Analysis of Single and Dual Under-Expanded, Rarefied Jets

A Dissertation Presented

by

Wenhai Li

to

The Graduate School
in Partial Fulfillment of the
Requirements
for the Degree of

Doctor of Philosophy

in

Mechanical Engineering

Stony Brook University
December 2010

Stony Brook University

The Graduate School

Wenhai Li

We, the dissertation committee for the above candidate for the
Doctor of Philosophy degree, hereby recommend
acceptance of this dissertation.

Dr. Foluso Ladeinde - Dissertation Advisor
Associate Professor, Department of Mechanical Engineering, Stony Brook University

Dr. John Kincaid - Chairperson of Defense
Professor, Department of Mechanical Engineering, Stony Brook University

Dr. Robert Kukta
Associate Professor, Department of Mechanical Engineering, Stony Brook University

Dr. Xiaolin Li - Outside Member
Professor, Department of Applied Mathematics and Statistics, Stony Brook University

This dissertation is accepted by the Graduate School

Lawrence Martin
Dean of the Graduate School

Abstract of the Dissertation

Analysis of Interacting, Under-Expanded, Rarefied Jets

by

Wenhai Li

Doctor of Philosophy

in

Mechanical Engineering

Stony Brook University

2010

A numerical study, using the Direct Simulation Monte Carlo (DSMC) approach, of the interaction effects between two identical sonic under-expanded nitrogen jets under rarefied conditions is reported. In this study, the effects of the jet stagnation Knudsen number (Kn_s), the ratio of the stagnation-to-background pressure (P_s/P_b), and the distance between the jet orifices (L/D) were investigated for a range of these parameters. The "primary-secondary" shock-cells structure has been successfully reproduced when flow is in the near continuum flow regime. The response of the system to various combinations of Kn_s, P_s/P_b, and L/D, is reported with a focus on the shock structures as well as the rarefaction effects. It shows that the background pressure has a very significant effect on the physics of flow, and the interactions between the two jets affect the location of the Mach disks for both the primary and secondary jets. When flow is rarefied, a study of the rotational-translational non-equilibrium showed large deviations between the translational and rotational temperatures in the vicinity of the orifice plate. It is also found that the background gas helps to reduce the translational-rotational non-equilibrium effects in the secondary jet.

Contents

List of Symbols

A	area (m^2); a constant
b	miss-distance impact parameter (m)
$\vec{\boldsymbol{c}}$	velocity vector (m/s)
c'	thermal velocity (m/s)
c_m	velocity of center of the mass of the pair of molecules (m/s)
c_r	relative velocity (m/s)
D	diameter of orifice (m); diffusion coefficient ($m^2 \cdot s^{-1}$)
$\frac{D}{Dt}$	total derivative ($1/s$)
D_M	diameter of Mach disk (m)
d	diameter of gas molecule (m)
e	specific energy ($J \cdot kg^{-1}$)
erf	error function
E	energy (J)
$\vec{F}$	force vector (N)
F	jet thrust (N)
f	normalized velocity distribution function in velocity space
$f\left(\theta\right)$	angular distribution function
Kn	Knudsen number
k	Boltzmann constant ($J \cdot K^{-1}$)
L	characteristic length (m); normal shock wave thickness (m)
l^*	reference length of normal shock wave (m)
M	Mach number
m	mass of gas molecule (kg)
m_r	reduced mass of the pair of molecules (kg)
N	number of particles
$\dot{N}$	a number flux (s^{-1})

n	number density (m^{-3})
P	probability or pressure (Pa), depending on context
Re	Reynolds number
R	gas constant ($J \cdot kg \cdot K^{-1}$); radial distance (m)
R_f	a random number which is uniformly distributed between $[0, 1]$
Sc	Schmidt number
$\vec{r}$	position vector (m)
r_p	penetration distance of the background gas (m)
T	temperature (K)
T_r	rotational temperature (K)
T_t	translational temperature (K)
t	time (s)
u	velocity (m/s)
$u_{\max}$	adiabatic speed limit (m/s)
V_{mp}	most probable velocity (m/s)
X	horizontal distance from orifice exit (m)
X_M	horizontal distance from orifice exit to Mach disk (m)
Z_r	rotational collision number
α	exponent in the VSS molecular model; a constant
Γ	gamma function
γ	specific heat ratio
ε	azimuthal impact parameter
Θ	characteristic temperature (K)
θ	angle
λ	mean free path (m)
μ	fluid dynamic viscosity ($N \cdot s \cdot m^{-2}$)
ν	collision rate (s^{-1})

ξ	rarefaction parameter ($dynes \cdot cm^{-1} \cdot K^{-1}$)
ρ	density ($kg \cdot m^{-3}$)
σ	collision cross-section (m^2)
σ_T	total collision cross-section (m^2)
ζ	number of internal degrees of freedom
τ	relaxation time (s); collision interval (s)
υ	relative speed exponent of VHS model
ϕ_r	fraction of the total molecular collisions that lead to the relaxation of the rotation mode
χ	deflection angle
Ω	solid angle
ω	temperature exponent of the coefficient of viscosity

Superscripts

*	post-collision values; conditions at the orifice exit (sonic values)

Subscripts

1	value right in front of shock wave
2	value right behind shock wave
b	value of background gas
c	value of colliding pair
i	value of internal energy; value of internal energy of mode i
j	value of jet gas
r	value of rotational mode
ref	reference value
s	value at stagnation conditions
t	value of translational mode
v	value of vibrational mode
∞	value at freestream

List of Figures

List of Tables

Acknowledgments

I would like to thank Professor Foluso Ladeinde, the project advisor, for supervising the work and providing effective guidance.

I would also like to thank my committee members, Professor John Kincaid, Professor Robert Kukta, and Professor Xiaolin Li, for their insightful comments.

I would like to acknowledge TTC Technologies, Inc., for providing the computer development environment for the DSMC code and making the AEROFLO software available to me free-of-charge.

Stony Brook University is also acknowledged for providing the Seawulf cluster as the parallel simulation environment.

I would like to thank my wife Yanan Di for standing beside me throughout my Ph.D. life.

Chapter 1
Introduction

In this chapter, we present the motivation, choice of simulation method, and the objectives of the thesis work.

1.1 Motivations of the Study

Although the thesis work includes both single and dual jets, it is the latter that is of practical application, with the former providing important foundation and baseline.

The interaction between rarefied free jets has received some attention in recent years because of the relevance to rockets and other space vehicles [1–3]. For rockets, two or more nozzles are used in order to provide a large impulse and stability [4]. Because of the high altitude, the pressure is low, which causes the plumes from each nozzle to have a large radial extent. Therefore, an interaction between the neighboring plumes may occur. Another example is the spacecraft's Orbiter Reaction Control System (RCS) [5–7], which always comprises of many primary and vernier engines. The RCS can provide the thrust for altitude maneuvers and for small velocity changes along the orbiter axis by firing selected engines. If adjacent engines are fired simultaneously, an interaction between the two jets can occur. The jet interaction phenomena can also be seen in the satellite's Altitude Control System (ACS), which is used to control the altitude of a satellite [8]. This system is generally formed by an array of small thrusters. Because the size of the satellite is small and the plume size is large in high altitude, interaction between the adjacent plumes can be significant.

Recently, the interaction between multiple plumes has become more and more important with the development of microspacecraft [9]. Many designs of micro-propulsion systems involve the use of thruster arrays for orbital maneuvers, such as attitude control and orbit rising. The thruster arrays can be batch-fabricated using Microelectromechanical Systems (MEMS) techniques. The thruster array can increase the flexibility for microspacecraft since thrusters can be fired in specific sequences, or simultaneously, to obtain desired impulse profile and thrust level for a particular maneuver. The distance between the thrusters in an array is always very small. Therefore, the interaction between the plumes may occur.

Another popular application of the interacting jets is in the plasma-aided materials processing technique [10]. A particular example is expanding thermal plasma (ETP) thin film decomposition, which can deposit thin films or coating on the materials. Schaepkens [11] has found that in the ETP process, a properly optimized dual-source system can deposit a uniform thick coating of abrasion-resistant material across a width of 30 cm of substrate in one pass. Autric [12] also reported experimental data on the dual-source crossed beams pulsed laser deposition technique for the production of cryolite thin films.

The interaction between jets can have several effects on spacecraft operation, such as changes in the thrust impulse profile, the dynamic of jet impingement, the heat flux and pressure force on the spacecraft surfaces, the contamination, stability performance, and noise generation [13, 14]. These phenomena can cause a lot of difficulties in the design of a spacecraft. For example, when the interaction effects are strong, there is a backflow region generated in the interaction region [15]. The backscattering molecules can enhance contamination and can also lead to relatively high heat flux and surface forces that exceed the fatigue failure limit for metallic aircraft structures. Another example is for acoustic generation. It has been observed that twin jets in jet engines reduce noise [16–18].

Rapidly expanding plumes at high altitudes involve the entire range of flow regimes, from continuum flows near the nozzle exit to transitional and then free molecular flow at large distances from the nozzle. Furthermore, for flight at different altitudes, the plumes from the spacecraft exhaust may be expanded into a background with finite pressure for the flight in the earth's atmosphere, or into vacuum for flight in outer space. Therefore, rarefaction effects could become an important issue for multiple jets. If the jets expand into vacuum, only the interactions between the molecules of the two jets need be considered. If the interaction is strong, oblique shocks wave are formed, as shown in Figure 1.1(a). The interaction region, which is surrounded by the oblique shocks, looks like another jet plume and will be referred to as the "secondary jet." If the jets expand into a background with finite pressure, the interactions between the molecules of the jets with those of the background gas become important. If the interaction is strong, barrel shocks and jet boundaries, which take on concave curvature, are formed. Together with the normal shock waves (Mach disks, for both primary and secondary jets) and the oblique shocks, a well-known "primary-secondary" shock-cell structure is formed (Figure 1.1(b)).

1.2 Choice of Simulation Method

Experimental investigation of high speed jet flows is expensive and involves practical difficulties, such as the need for non-intrusive flow measurements at high speed. The number of experimental studies is limited but includes those in [19] and [20]. Numerical analysis is an attractive option that is pursued in this thesis. For the flow in the rarefied regime, the direct simulation Monte-Carlo (DSMC) method has proven to be a very powerful technique [33]. Since the method statistically solves the Boltzmann equation, the DSMC method is theoretically applicable to the simulation of gas flows in all regimes: continuum, rarefied, and transition. Also, the DSMC method can accurately simulate the relaxation process between the translational and internal energies, and between the different modes of internal energy. Therefore, the thermal and chemical non-equilibrium effects can be calculated by DSMC [21, 22].

Many researchers have used the DSMC method for the dual interacting jets expanding into vacuum, such as Zhu and Dagum [5–7], Ketsdever [9], and Wu [23]. The numerical investigation of jets expanding into a background with finite pressure is extremely challenging for numerical methods, including the DSMC approach. For interacting jets expanding into a background with finite pressure, the density in the flow field is much higher than that for jets expanding into vacuum. Therefore, more simulated particles are needed. Since the problem is fully three-dimensional, the computation is very expensive. Also, the implementations of the downstream boundary conditions, where, depending on the problem, background pressure and temperature are specified, pose additional difficulties for the DSMC method. The traditional pressure boundary condition handling method, which usually includes a huge pressure reservoir in the computation, is very expensive. Recently, the "particle conservation" method was developed to address this problem [24–26]. With the flow velocity calculated at the downstream boundary and background pressure and temperature specified, correct stream boundary conditions can directly be applied in DSMC without using a pressure reservoir. The method has been used successfully by Wu [27] and the author [28] in single under-expanded jet calculations. However, the procedure has not been used for calculating interacting rarefied jets. The exception is Usami [29], who numerically simulated dual interacting jets expanding into a region with finite pressure by using DSMC and successfully captured the "primary-secondary" shock-cell structures. However, he assumed zero velocity at the downstream boundary which is problematic [27]. A more detailed investigation of the interaction between nitrogen jets under rarefied conditions is undertaken for both cases when the background region is either vacuum or has finite pressure.

1.3 Objective of the Research

In this projects, we want to achieve the following objectives:

(1) Develop, implement, and validate a robust three-dimensional parallel DSMC code for simulating flow at all Knudsen number regimes.

(2) Simulate, as the benchmark problem for interacting jets, the single under-expanded jets. Test the "particle conservation" method for implementing the pressure background boundary conditions. Reproduce the "shock-cell" structures. Investigate translational-rotational non-equilibrium effects in nitrogen under-expanded jets.

(3) For dual interacting jets, study the two situations where the jets expand into vacuum and into a region of finite pressure. Reproduce the ’primary-secondary’ shock-cell structures when the dual interacting jets exhaust into a finite background pressure. Analyze the interactions between the molecules of the two jets and those of the jets’ molecules with the molecules of the background gas.

(4) Investigate the response of the system to various combinations of the jet stagnation Knudsen number Kn_s, the under-expanded jet pressure ratio P_s/P_b, and the separation between the two orifices L/D, with a focus on the shock structures as well as the rarefaction effects. The location of the Mach disk in the secondary jet will be analyzed. The thermal non-equilibrium effects in the secondary jet will also be studied.

This dissertation is organized as follows: In Chapter Two, we present an overview of rarefied gas dynamics and the implementation of the DSMC method. In Chapter Three, the DSMC code is first validated with a one-dimensional normal shock wave problem. The problem of a two-dimensional hypersonic flow past a cylinder is also simulated for the validation purpose in Chapter Four. In Chapter Five, the single rarefied under-expanded jet problem is investigated. The dual, interacting jets are studied in Chapter Six. Chapter Seven contains the concluding remarks.

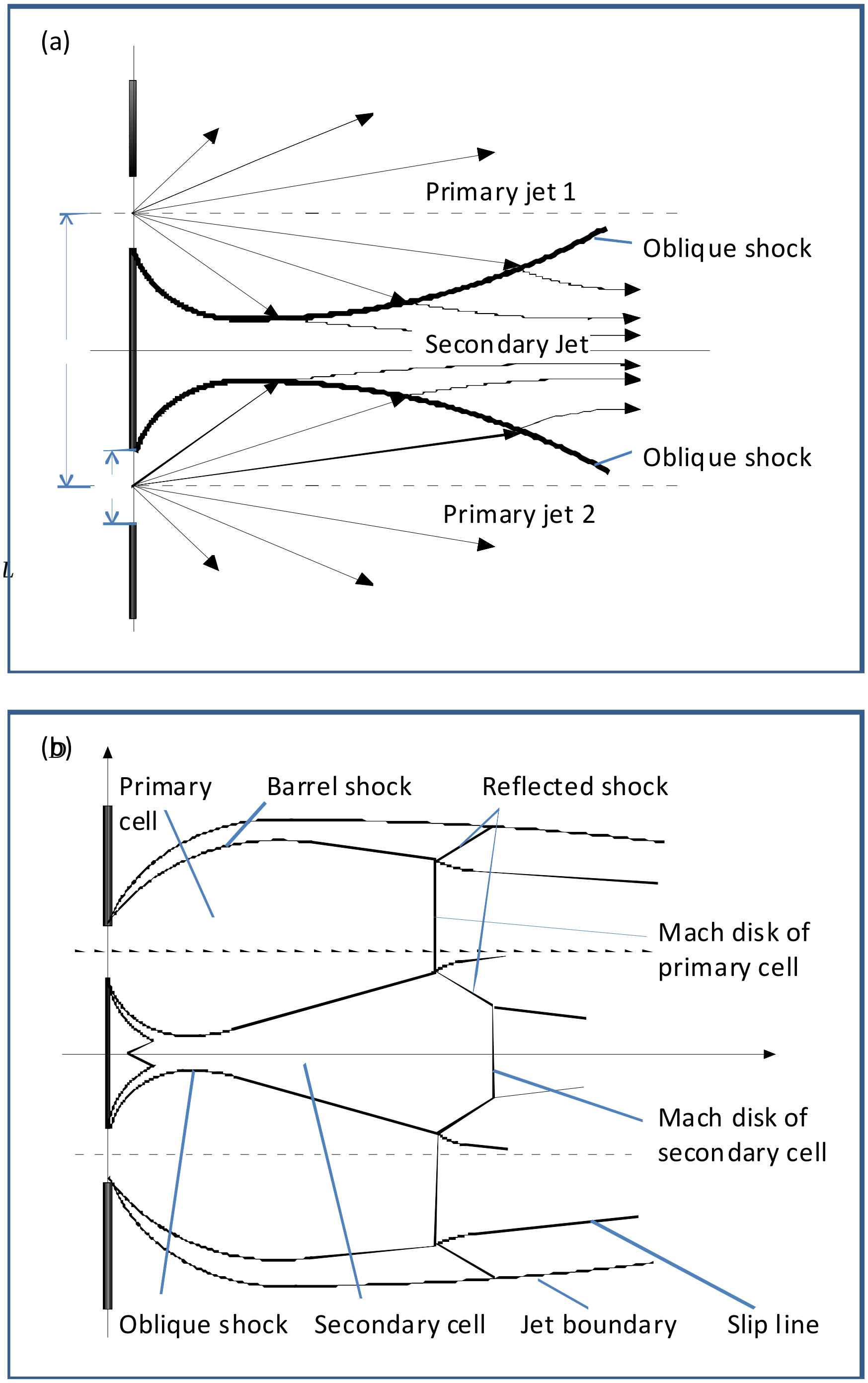

Figure 1.1. Shock structure of dual interacting jets in continuum flow regime: (a) flow expanding into vacuum; (b) flow expanding into a background with finite pressure

Chapter 2
Numerical Approach

In this chapter, we introduce the basic concepts of rarefied gas dynamics and a summary of a Direct Simulation Mote Carlo (DSMC) procedure.

2.1 Overview of Rarefied Gas Dynamics

When the averaged distance traveled by the gas molecules between collisions (the mean free path) is comparable to the characteristic length of the flow field, the continuum fluid approximation breaks down and the particle nature of the gas must be taken into consideration. This behavior can be characterized by the Knudsen Number:

$$Kn = \frac{\lambda}{L} \, , \tag{2.1}$$

where λ is the mean free path and L is the characteristic length. Often, L is taken as the length scale of a macroscopic scale, given by [30]

$$L = \frac{\varphi}{\left|\frac{d\varphi}{dx}\right|} \, , \tag{2.2}$$

where φ is a suitable macroscopic quantity, such as density, temperature, or velocity. Therefore, the flow can be said to be "rarefied" either when λ is large (low density) or when L is small (large flow gradient). It can also be shown that the Knudsen number Kn is related to

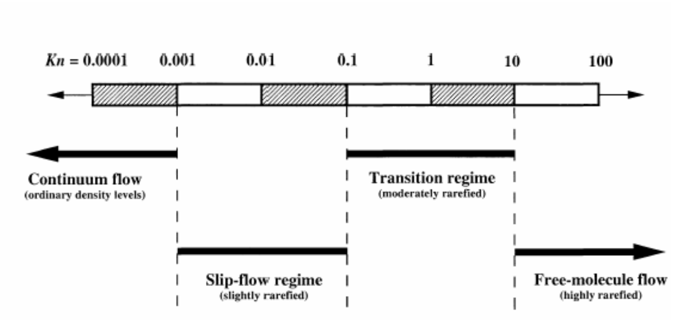

Figure 2.1. The flow regimes in gas dynamics

the Mach number M and Reynolds number Re by

$$Kn \approx \sqrt{\frac{\pi\gamma}{2}}\frac{M}{\mathrm{Re}}\,, \tag{2.3}$$

where γ is the gas specific heat ratio.

For different Knudsen numbers, the flow field can be divided into four regimes [31] as shown in Figure 2.1:

- When $Kn < 0.001$, the flow is said to be in the continuum regime. The flow field is governed by the Navier-Stokes equations. This regime is used in the classic kinetic gas dynamics.

- When $0.001 < Kn < 0.1$, the flow is said to be in the slip-flow regime (also called near-continuum regime). At the surface boundary, particle effects, such as velocity slip and temperature jump, are significant.

- When $0.1 < Kn < 10$, the flow is in the transition regime. The molecular mean free path λ and the characteristic length L are approximately of the same order. In this regime, rarefaction effects play an important role in the whole flow field.

- When $Kn > 10$, the flow is said to be in free-molecular regime. The molecular mean free path is much larger than the characteristic length scale of the flow field and there is no intermolecular collision. In this regime, the flow can be accurately solved by molecular gas dynamics.

Rarefied gas flows are governed by the Boltzmann equation, which can be expressed as [33]

$$\frac{\partial f}{\partial t} + \mathbf{c}\cdot\frac{\partial f}{\partial \mathbf{r}} + \mathbf{F}\cdot\frac{\partial f}{\partial \mathbf{c}} = \int_{-\infty}^{+\infty}\int_{0}^{4\pi}\left(f^{*}f_{1}^{*} - ff_{1}\right)c_{r}\sigma d\Omega d\mathbf{c}_{1} \ , \tag{2.4}$$

where f is velocity distribution function, t is time, $\mathbf{r}$ is position vector, $\boldsymbol{c}$ is velocity vector, $\mathbf{F}$ is field force vector, c_r is relative speed, σ the collision cross-section, and Ω the solid angle. The superscript '*' implies post-collision values and subscript '^{1}' implies a reference to the particle collided with. The left-hand side of the equation represents the change of the velocity distribution due to the motion of the molecules. The right-hand side is the change of the velocity distribution due to the collisions between the molecules.

There are several ways to solve the Boltzmann Equation. In general, there are two approaches: analytical methods and numerical methods. Analytical solutions are difficult

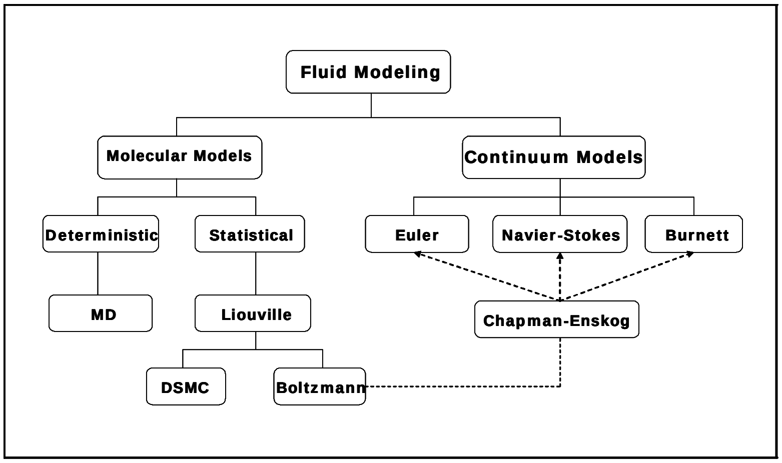

Figure 2.2. The different kinds of fluid models

to obtain. It is only in a few cases that an analytical solution of the velocity distribution exists. One example is the Chapman-Enskog theory. The method assumes the deviation of the velocity distribution function f from the Maxwellian distribution is small and it can be treated as a perturbation. Using the Chapman-Enskog approximation to expand the Boltzmann equation, we obtain the Euler equations, the Navier-Stokes equations, and the Burnett equations, which are, respectively, the zeroth order, first order, and second order solutions of the Boltzmann equation [34]. It is important to note that the Boltzmann equation applies equally to the transition and continuum regimes.

Molecular simulation is the most popular way to numerically solve the Boltzmann equation. Two typical methods, molecular dynamics (MD) and direct simulation Monte Carlo (DSMC) are frequently used. Both methods solve the Boltzmann equation by using simulated particles to statistically model the molecular motions and intermolecular collisions in real gas flows. The MD method is deterministic and whether or not two molecules will collide depends on the distance between them. On the other hand, the DSMC method is statistical and it uses a collision probability to judge if two particles will collide. Also, in DSMC, simulated particles, which can be regarded a group of real molecules, are used. Therefore, the DSMC calculation is less expensive than the MD method. However, the statistical scattering error is introduced into DSMC. Figure 2.2 gives a summary of the different fluid models.

2.2 The Procedure for the Sequential DSMC Code

A parallel, three-dimensional direct simulation Monte Carlo (DSMC) program has been developed for the present study, using procedures similar to those in Bird [32,33]. A review of the advances in the DSMC method in fluid mechanics has been presented by Oran et al [30]. The typical sequential DSMC procedure can be summarized by the following steps:

(1) Initialization of cells and particles: In DSMC, the calculation of inter-molecular collisions and the sampling of macroscopic properties is based on the computational cells. Therefore, the computational cells are first generated. The position, velocities, and internal energies of the simulating particles are also initialized.

(2) Movement of the particles: For each time step, when the inter-molecular force is negligible, the trajectories of the particles is simply computed by Newton's law: $\triangle\vec{r} = \vec{c}\triangle t$.

(3) Interaction with the boundaries: Particles which cross the boundary of the simulation domain are either removed from the simulation or reflected back to the domain. Removal occurs when a particle reaches the inflow or outflow boundaries. Refection occurs when a particle hits the wall surfaces or crosses the lines of symmetry.

(4) Sorting and indexing: When a particle arrives at its new position, it needs to be sorted and grouped into the corresponding computational cell. This is required for

the collision calculation and result sampling. This step is typically computationally expensive.

(6) Calculation of inter-molecular collisions: The inter-molecular collisions are calculated cell-by-cell, by the following steps:

  a. A potential collision pair is randomly selected in a cell.

  b. A collision probability is calculated to check if the selected pair will collide. Bird [33] proved that the collision probability is only decided by the molecular total collision cross-section σ_T and the relative velocity between the pairs, c. The collision probability is decided by $P \propto \sigma_T c_r$. An acceptance-rejection algorithm is used to decide if the pairs collide with the computed P. First, P is normalized by its maximum value, $P_{\max}$. Then, the normalized value $P/P_{\max}$ is compared with a random number R_f, which is uniformly distributed between $[0, 1]$. If $P/P_{\max} > R_f$, the collision occurs. If $P/P_{\max} < R_f$, the collision does not occur and the collision pair needs to be re-selected.

  c. When collision occurs, for elastic collision, the magnitude of the post-collision velocity of the collision pair is calculated based on momentum and energy conservation. The post-collision velocity of each particle is dependent on the selection of the molecular model in DSMC. If the molecules have internal degrees of freedom, inelastic collisions need to be considered and the total collision energy will be re-distributed between the degree of freedom. This calculation depends on the selection of the inelastic collision model in DSMC.

d. The collision calculation in time will continue until the total number of inter-molecular collisions in the current time step has a value that complies with the real physics. There are several methods to decide when the computed number of collision is sufficient for a time step and will be discussed in the next section.

(7) Repeat steps (2) through (6) for the next time step until flow reaches steady state and obtain enough number of samplings.

(8) Sampling of microscopic properties and output of macroscopic results: The macroscopic properties are calculated by averaging the properties of all the molecules in a computational cell based on the kinetic theory. The results include an error due to the statistical scatter. Better results require a larger sample size. It has been shown that the magnitude of statistical fluctuations varies according to the inverse square root of the sample size [33]. Therefore, it is necessary to perform time averaging for the steady flows and ensemble averaging for the unsteady flows, in order to obtain smooth results.

Figure 2.3 is a flow chart for the current sequential DSMC code.

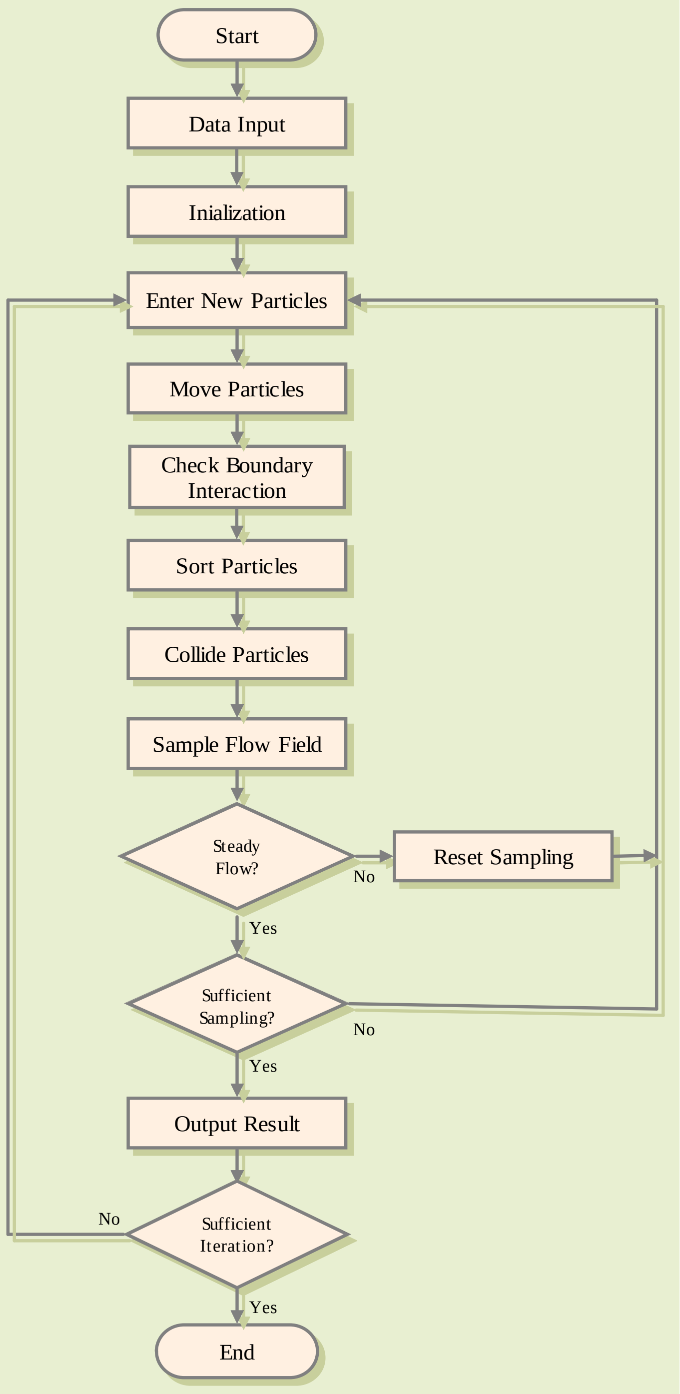

Figure 2.3. Flow chart for a sequential DSMC code

2.3 Models for DSMC

To calculate the inter-molecular collision, several kinds of molecular models have been implemented in the present work:

(a) the Variable Soft Sphere (VSS) molecular model [33] is used for the binary molecular collision;

(b) Bird's "no-time counter" (NTC) algorithm [33] is used to control the collision mechanics;

(c) the Borgnakke-Larsen phenomenological model [36] is used to calculate the internal energy relaxation process.

The details of each model are provided in the following subsections.

2.3.1 Models for Elastic Collisions

In the calculation of binary elastic collisions, the relationship between the deflection angle χ and the miss-distance impact parameter b, and that between the effective cross-section σ_T and the relative velocity c_r need to be modeled (Figure 2.4). Several phenomenological models are available for this purpose.

The hard sphere (HS) molecular model [33] is the simplest model. The collision cross-section is a constant and is computed by $\sigma_T = \pi d^2$, where d is the diameter of the molecule. The model has a very simple scattering relation $\chi = 2\cos^{-1}(b/d)$.

The shortcoming of the HS model is that it does not account for the cross-section change with different values of c_r. This led to the creation of the variable hard sphere (VHS) molecular model [33], which combines the scattering simplicity of the HS model with a variable cross-section based on the effective cross-section in the inverse power law molecular model. The molecular diameter is proportional to the relative collision velocity raised to the power ν. This leads to a viscosity coefficient μ proportional to temperature to power $\omega = \nu + 1/2$. The coefficient ω is chosen to fit the viscosity coefficient in real gas. Therefore, the "d" in the expression for the collision cross-section is computed as $d/d_{ref} = (c_r/c_{r,ref})^{\omega-1/2}$. The calculation of the deflection angle is the same as in the HS model.

Although the VHS model can reproduce the viscosity coefficient, it does not lead to the correct diffusion coefficient D. This led to the development of the variable soft sphere (VSS) model [33]. The model introduces an additional power-law parameter α into the hard sphere expression for the deflection angle. The parameter α can be computed by the Schmidt number, with the relation $S_c = \frac{2+\alpha}{(3/5)(7-2\omega)\alpha}$. Therefore, the deflection angle is computed as $\chi = 2\cos^{-1}\left\{(b/d)^{1/\alpha}\right\}$. The calculation of the cross-section is the same as in the VHS model.

In this project, the VSS model is used. The value of the post-collision velocity is computed by

$$\begin{cases} \mathbf{c}_1^* = \mathbf{c}_m^* + \frac{m_r}{m_1}\mathbf{c}_r^* \\ \mathbf{c}_2^* = \mathbf{c}_m^* + \frac{m_r}{m_2}\mathbf{c}_r^* \end{cases} . \tag{2.5}$$

From the momentum and energy conservation, we obtain

$$\begin{cases} \mathbf{c}_m = \mathbf{c}_m^* \\ |\mathbf{c}_r| = |\mathbf{c}_r^*| \end{cases} , \tag{2.6}$$

where $\mathbf{c}_m \equiv \frac{m_1\mathbf{c}_1+m_2\mathbf{c}_2}{m_1+m_2}$ is the velocity of the center of mass of the pair of molecules and $m_r \equiv \frac{m_1 m_2}{m_1+m_2}$ is called the reduced mass. The superscript "*" implies post-collision condition. The subscripts '1' and '2' indicates particle 1 and particle 2, respectively, in the colliding pair. The relative velocity of post-collision is $\vec{c}_r^* = c_r^*\vec{n}$ and the unknown direction $\vec{n} = (n_1, n_2, n_3)^T$ is calculated as

$$\begin{cases} n_1 = \cos\chi_1 \\ n_2 = \sin\chi_1 \cos\chi_2 \\ n_3 = \sin\chi_1 \sin\chi_2 \end{cases} , \tag{2.7}$$

where deflection angles χ_1,χ_2 are determined by

$$\cos\chi_1 = 2 * R_f^{1/\alpha} - 1 \quad \text{and} \quad \chi_2 = 2\pi R_f \quad . \tag{2.8}$$

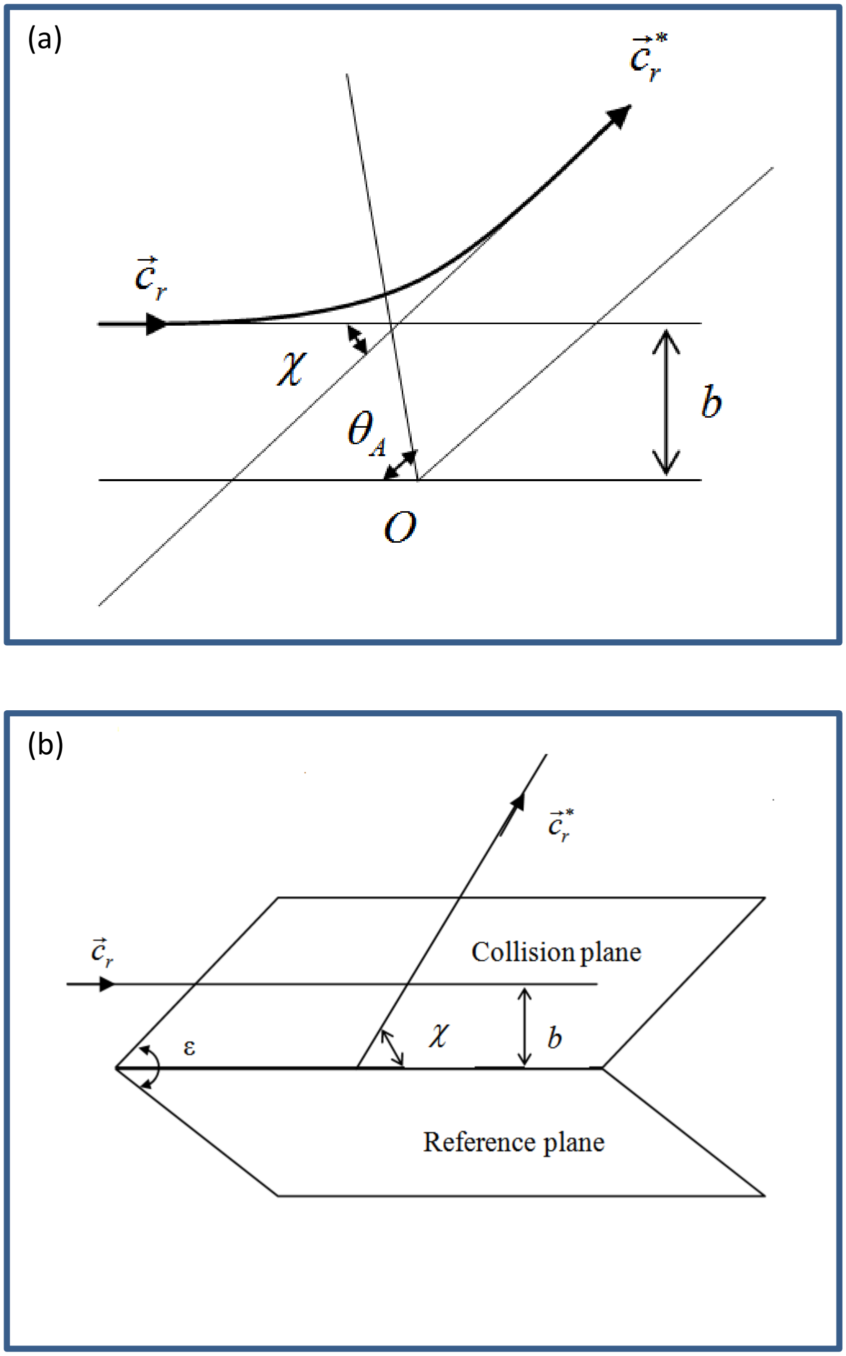

Figure 2.4. Illustration of the impact parameters in binary collisions: (a) 2D frame; (b) 3D frame.

2.3.2 Collision Counting Model

Three models were developed to determine the number of collisions that need to be calculated in a given time step $\triangle t$: the time counter (TC) method [33], the null collision (NC) method [35], and the no-time counter (NTC) method [33].

The TC method, which was developed by Bird, consists of following three operations: (a) retain the randomly chosen pair if $(\sigma_T c_r)/(\sigma_T c_r)_{\max} > R_f$; (b) for each pair retained, compute $\tau = 2/(Nn\sigma_T c_r)$; and (c) collide pairs while $\tau_1 + \tau_2 + \tau_3 + \cdots \leq \triangle t$. In step (b), n represents number density and N represents the number of particles in a cell.

Koura [35] found that the collision number computed by TC tends to be larger than the expected value. Therefore, he developed the NC method by introducing the null collision concept. The key idea is to replace the σ_T in the TC method with $\sigma_{\max} = \sigma + \sigma_{null}$, where the null collision cross-section σ_{null} corresponds to null collision which does not change the velocity of the collision pair.

Bird developed the NTC method which avoids the problems with the TC method without any loss of computational efficiency. The method also has the advantage of easy vectorization of the collision procedure. In the NTC method, in the time interval $\triangle t$, the total collision number N_t is given by

$$N_t = \frac{1}{2} N n \sigma_T \overline{c_r^{2-2\omega}} \triangle t\ , \tag{2.9}$$

where the sign '—' implies averaging. In NTC method, the collision computation is repeated until the number of collisions in a time step is equal to N_t. The NTC method is used in this thesis work.

2.3.3 Inelastic Collision Model

For the inelastic collisions, models need to be used to judge when the inelastic collision occurs and how the energy is distributed between the degrees of freedom. The Borgnakke-Larsen (BL) model [36] is the most commonly used model for inelastic collision calculation. In BL model, the inelastic collision happens only for a fraction ϕ_i of the total particle collision. This is computed by $\phi_i = 1/Z_i$, where Z_i is called the relaxation number for the internal mode i. The post-collision values of each kind of internal energy (rotational energy, vibrational energy, etc.) are simply sampled from the known equilibrium distribution functions and are equally partitioned between the degrees of freedom of the mode i. The relaxation process is governed by Jean's equation [33]:

$$\frac{DT_r}{Dt} = \frac{T_e - T_i}{\tau_i} = \frac{T_e - T_r}{\tau \cdot Z_i} \ , \tag{2.10}$$

where T_e is the equilibrium temperature, τ is the collision time, and $\tau_i = \tau \cdot Z_i$ is the relaxation time for the internal energy mode i. A correct value of Z_i must be used in the phenomenological model and it has been shown that Z_i may be a function of temperature.

We need to note that the collision number Z_i^{DSMC} defined in the DSMC is different with the collision number Z_i^{CONT} defined in the continuum simulations [37]. In continuum simulations, the collision number is defined as $Z_i^{\text{CONT}} = \tau_i/\tau_c$, where τ_c is mean collision time and τ_i is the characteristic relaxation time for the i-th internal energy. Lumpkin [42] developed the relation between Z_i^{DSMC} and Z_i^{CONT} as

$$Z_i^{\text{CONT}} = \left(1 = \frac{\zeta_i}{\zeta_T}\right) Z_i^{\text{DSMC}} \ , \tag{2.11}$$

where ζ_i is the number of degrees of freedom for the internal energy i.

The Translational-Rotational Relaxation

The Borgnakke-Larsen phenomenological model is used for the rotational-translational (RT) relaxation process in this investigation, whereby, the rotational relaxation is quantified in terms of a characteristic rotational collision number Z_r, which is approximately the reciprocal of the number of collisions required to reach equilibrium between the translational energy and rotational energy. The procedures for the Borgnakke-Larsen method applied to translational-rotational (TR) energy exchange can be described as follows [33]:

(a) After the colliding pairs are randomly selected by DSMC, the acceptance-rejection method is employed to judge whether or not an inelastic collision has taken place. The TR energy exchange takes place if $1/Z_r > R_f$.

(b) If a TR energy exchange has taken place, the rotational and translational energies of the colliding pairs are distributed according to the equilibrium energy distribution function for a specified number of degree of freedom, which is given by

$$f\left(\frac{E_r}{E_c}\right) = \frac{\Gamma\left(5/2 - \omega + \zeta_r\right)}{\Gamma\left(5/2 - \omega\right)\Gamma\left(\zeta_r\right)} \left(\frac{E_t}{kT}\right)^{3/2-\omega} \left(\frac{E_r}{kT}\right)^{\zeta_R - 1} \ , \tag{2.12}$$

where $f\left(\frac{E_r}{E_c}\right)$ is the probability of the occurrence of the energy distribution, $E_c = E_r + E_t$ is the total collision energy of the colliding pair, which is known and conserved during the collision. E_r and E_t are the rotational and relative translational energies of the colliding pair, ω is the temperature exponent of the coefficient of viscosity in VHS model and $5/2-\omega$ is the number of translational degrees of freedom contributing to the inelastic collision, ζ_R is the number of rotational degrees of freedom, k is the Boltzmann constant, and T is the temperature. The distribution function can be normalized by its maximum value:

$$\frac{f}{f_{\max}} = \left\{\frac{\zeta_R + 1/2 - \omega}{3/2-\omega}\left(\frac{E_t}{E_c}\right)\right\}^{3/2-\omega}\left\{\frac{\zeta_r + 1/2 - \omega}{\zeta_r - 1}\left(1-\frac{E_t}{E_c}\right)\right\}^{\zeta_r - 1} \quad . \tag{2.13}$$

To sample from this distribution, the following acceptance-rejection procedure is used. First, a uniformly distributed random number $R_{f,1}$ is employed to sample $E_r = R_{f,1}E_c$ and $E_t = E_c - E_r$. Then E_r and E_t are used to compute $f/f_{\max}$. The resulting $f/f_{\max}$ is used to compare with another uniform distributed random number $R_{f,2}$. If $f/f_{\max} < R_{f,2}$, E_r and E_t need to be re-calculated. If $f/f_{\max} > R_{f,2}$, the energy distribution is successful.

(c) Note that the post-collision rotational energy includes the rotational energy of each particle in the collision pair, $E_r = e_r^1 + e_r^2$. The quantities e_r^1 and e_r^2 are the respective rotational energy of particle 1 and particle 2 in the collision pair, which need to be sampled from the equilibrium distribution function:

$$f\left(\frac{e_r^1}{E_r}\right)=\frac{\Gamma\left(\zeta_r^1+\zeta_r^2\right)}{\Gamma\left(\zeta_r^1\right)\Gamma\left(\zeta_r^2\right)}\left(\frac{e_r^1}{E_r}\right)^{\zeta_r^1-1}\left(1-\frac{e_r^1}{E_r}\right)^{\zeta_r^2-1}\quad , \tag{2.14}$$

where ζ_r^1 and ζ_r^2 are the rotational degrees of freedom of particle 1 and particle 2, respectively. Note the relation $\zeta_r=\left(\zeta_r^1+\zeta_r^2\right)/2$. The distribution function can also be normalized by its maximum value:

$$\frac{f}{f_{\max}}=\left\{\frac{\zeta_r^1+\zeta_r^2-2}{\zeta_r^1-1}\left(\frac{e_r^1}{E_r}\right)\right\}^{\zeta_r^1-1}\left\{\frac{\zeta_r^1+\zeta_r^2-2}{\zeta_r^2-1}\left(1-\frac{e_r^1}{E_r}\right)\right\}^{\zeta_r^2-1}\quad . \tag{2.15}$$

The same acceptance-rejection method in step (b) can be used to sample the value of e_r^1 and e_r^2 from the given distribution function.

(d) The post-collision translational energy of the collision pair is distributed between the two particles by using the elastic collision calculation described in subsection 2.3.1.

In most cases, the rotational collision number Z_r is considered to be a constant. However, this is not correct when temperature profile varies significantly in the flow field. Parker [38] gave an approximate expression for the relation between Z_R and T:

$$Z_r=\frac{\left(Z_r\right)_\infty}{1+\left(\pi^{3/2}/2\right)\left(T^*/T\right)^{1/2}+\left(\pi^2/4+\pi\right)T^*/T}\quad , \tag{2.16}$$

where T^* is the characteristic temperature of the intermolecular potential and $\left(Z_r\right)_\infty$ is the limiting value. For the DSMC method, Parker's expression may be used to evaluate a single value for all collisions within a computational cell of local translational temperature . But Hass [39] argued that it can be computationally expensive to calculate, which may itself be ill-defined in nonequilibrium flows. Boyd [40, 41] developed an expression for Z_r that is dependent on the relative energy of individual collisions and that reproduces Parker's expression when integrated over all collisions at equilibrium. The expression is

$$\phi_r \frac{(Z_r)_\infty}{Z_t} = 1 + \frac{\Gamma(2-\omega)}{\Gamma(3/2-\omega)} \left(\frac{2kT^*}{m_r c_r^2}\right)^{1/2} \frac{\pi^{3/2}}{2} + \frac{\Gamma(2-\omega)}{\Gamma(1-\omega)} \left(\frac{2kT^*}{m_r c_r^2}\right) \left(\frac{\pi^2}{4} + \pi\right) \quad , \tag{2.17}$$

where Z_t is the translational collision number which is usually taken as unity in DSMC calculations. It was shown that the model can provide better results for the calculation of a standing shock wave [41] and the shock wave thickness for a range of Mach numbers [42]. However, it is found that it fails to achieve the equipartition of the thermal modes, or fail to achieve detailed balance. That is, the equilibrium state can not be kept at equilibrium when this scheme is applied. Abe [43] developed a new model which employs the instantaneous probability and obeys the principle of detailed balance. He modified the BL model to

$$f\left(\frac{E_r}{E_c}\right) = \frac{\phi_r(E_t)}{\phi_{\max}} \frac{\Gamma(5/2-\omega+\zeta_r)}{\Gamma(5/2-\omega)\Gamma(\zeta_r)} \left(\frac{E_t}{kT}\right)^{3/2-\omega} \left(\frac{E_r}{kT}\right)^{\zeta_r-1} \quad , \tag{2.18}$$

where $\phi_{\max}$ is a value larger than any possible $\phi_r(E_t)$.

The Translational-Vibrational Relaxation

In the classical BL model, the vibrational energy is considered to be continuous [33]. If the vibration follows the simple harmonic oscillator (SHO) model, the specific vibration energy associated with a mode having a characteristic vibrational temperature Θ_v is

$$E_v = \frac{R\Theta_v}{\exp(\Theta_v/T) - 1} \quad . \tag{2.19}$$

Therefore, the effective number of degrees of freedom at temperature T is

$$\zeta_v = \frac{2\Theta_v/T}{\exp\left(\Theta_v/T\right) - 1} \ . \tag{2.20}$$

In the inelastic collision calculation, the total collision energy E_c is first distributed between the translational energy E_t and the internal energy $E_i = E_r + E_v$ by following the procedures similar to TR translation. The only difference is to use $\zeta_i = \zeta_r + \zeta_v$ to substitute for ζ_r. Then the equipartition of the rotation energy E_r and vibration energy E_v is decided by using acceptance-rejection method for the following expression:

$$\frac{f}{f_{\max}} = \left\{ \frac{\zeta_r + \zeta_v - 2}{\zeta_r - 1} \left(\frac{E_r}{E_i} \right) \right\}^{\zeta_r - 1} \left\{ \frac{\zeta_r + \zeta_v - 2}{\zeta_v - 1} \left(\frac{E_v}{E_i} \right) \right\}^{\zeta_v - 1} \ . \tag{2.21}$$

Because the vibrational spectrum of real gas molecules is characterized by large gaps between the neighboring energy levels, the continuity of the vibrational energy mode assumed in the classical BL model is obviously too approximate. The quantum effects need to be considered. This is true especially for low-temperature flows. A discrete version of the BL model was developed [44, 45]. For level i of a particular mode, the harmonic oscillator model gives the vibrational energy of that mode as

$$E_v = ik\Theta_v \ . \tag{2.22}$$

The Boltzmann distribution of the energy level can be written as

$$f_{E_v} \propto \exp\left(-\frac{E_v}{kT} \right) \delta\left(E_v - ik\Theta_v \right) \ . \tag{2.23}$$

The distribution function for a particular combination of E_v and E_t is given by

$$f\left(\frac{E_v}{E_c} \right) \propto \left(E_c - E_v \right)^{3/2-\omega} \delta\left(E_v - ik\Theta_v \right) \exp\left(-\frac{E_c}{kT} \right) \ . \tag{2.24}$$

The maximum probability is for the ground state $E_v = 0$. Therefore, $f/f_{\max}$ can be calculated as

$$\frac{f}{f_{\max}} = \left(1 - \frac{ik\Theta_v}{E_c}\right)^{3/2-\omega} \quad . \tag{2.25}$$

The detailed procedures used in DSMC are described as follows:

(a) Calculate the maximum possible level by

$$i_{\max} = \text{INT}\left(\frac{E_c}{k\Theta_{v,1}}\right) \quad , \tag{2.26}$$

where $\Theta_{v,1}$ is the characteristic temperature of level 1.

(b) Randomly select the post-collision vibration level as

$$i = R_f i_{\max} \quad . \tag{2.27}$$

(c) Calculate $f/f_{\max}$ and use the acceptance-rejection method to decide whether or not this energy exchange can occur.

The vibrational relaxation probability is also dependent on the collision temperature or energy. Boyd [46] developed the expression that is dependent on energy and agrees with the vibrational relaxation time given by Millikan and White [47]. He assumed that the probability has the form

$$\phi_v = \frac{1}{Z_0} c_r^{3+2\omega} \exp\left(\frac{-c_r^*}{c_r}\right) \quad , \tag{2.28}$$

where Z_0 is constant and c_r^* is a characteristic velocity. c_r is the relative velocity of the colliding pair. Hash and Hassan [48] developed the expression that is dependent on the temperature based on Millikan and White's vibrational relaxation time.

Chemical Reaction

Although the chemical reaction is not included in this study, the author would still like to introduce the chemical reaction models in DSMC for possible implementation in future research.

In DSMC method, most reaction models try to convert the continuum chemical reaction rate equations into chemical collision cross-sections. The chemical collisions occur as part of the collision process with the probability equal to the ratio of the chemical collision cross-section to the elastic cross-section. Several models, like Total Collision Energy (TCE) model [49], Vibrationally Favored Dissociation (VFD) model [50, 51], Generalized Collision Energy (GCE) Model [52], and Threshold Line (TL) Model [53] were developed and implemented in some chemical reactions in DSMC simulations. These models were evaluated by comparing the numerical results with the available experimental results [54–58].

2.4 Computational Parameters

Several important simulation parameters are introduced in this section.

Particle Weight

Each computational particle in DSMC represents a large number of real molecules. The number of real molecules represented by a computational particle is termed as particle weight W_p. Smaller values of W_p result in a larger number of computational particles in the simulation. Since the statistical fluctuation is determined by the sampling size. Larger number of computational particles can provide more accurate result. However, due to the restriction of the computational resource and computation time, the number of computational particles should be restricted to a proper number. For DSMC simulation, the number of the particles per cell should be more than 10.

Time Step

A finite time is used to decouple the movement of particles from collisions. To comply with the dynamic theory, this requires the time step must be a smaller value than the molecular mean collision time τ. For a single species gas using VSS model, τ is [33]

$$\tau = \frac{\sqrt{\pi}}{2} \frac{4\alpha\left(5-2\omega\right)\left(7-2\omega\right)}{5\pi^{1/2}\left(\alpha+1\right)\left(\alpha+2\right)} \left(\frac{m}{2kT}\right) \frac{\mu}{\rho}\,. \tag{2.29}$$

Generally, the time step can be chosen as a fraction of τ. In this study, $\Delta t = 0.8\tau$.

Grid Cell Size

The size of the computational cells is limited by the constraints of physical accuracy and computational efficiency. In DSMC, the particles are grouped cell-by-cell, and the collision calculation is computed cell-by-cell. In a real gas, the average distance travelled by a particle between collisions is termed as the mean free path λ. For a single species gas using VSS model, λ is [33]

$$\lambda = \frac{4\alpha\left(5-2\omega\right)\left(7-2\omega\right)}{5\pi^{1/2}\left(\alpha+1\right)\left(\alpha+2\right)}\sqrt{\frac{m}{2kT}}\frac{\mu}{\rho} \quad . \tag{2.30}$$

Because the collision pairs are randomly selected in a cell during the collision calculation, to comply with real physics, the size of the grid cell should be smaller than λ. On the other hand, the number of particles in a cell should maintain in a number level to retain the accuracy. Smaller grid cells require more particles in the simulation, which lower the computational efficiency. Therefore, the size of the cell should be selected to a proper value to optimize both the physical accuracy and computation efficiency. In this study, $\Delta x = \lambda$.

Number of Iterations

One way to judge if the calculation has reach the steady state is to monitor the overall number of particles in the computational domain. If the total number of particles is almost unchanged, the flow can be considered to be steady. To obtain the steady state results and further reduce the scattering error, another several thousands time steps of calculation are required after the flow reaches the steady state to obtain enough number of samplings. The steady state results are obtained by performing time-averaging on these samplings.

2.5 Boundary Conditions for DSMC

In this section, we will discuss how to implement different kinds of boundary conditions in DSMC.

Stream Boundary

For a specified stream enters across the inlet boundary with a velocity V, the number of particles $\dot{N}$ entered per unit time per unit boundary area is computed by [33]

$$\frac{\dot{N}_i}{A} = \frac{nV_{mp}\left\{\exp\left(-s^2\right) + \sqrt{\pi}s\left[1 + \mathrm{erf}\left(s\right)\right]\right\}}{2\sqrt{\pi}} \quad , \tag{2.31}$$

where $V_{mp} = \sqrt{2RT}$ is the most possible velocity, and s is the molecular speed ratio which is given by

$$s = \frac{V}{V_{mp}} \cos\theta \quad . \tag{2.32}$$

A is the area of the boundary surface element, R is the gas constant, erf is the error function, and θ is the angle between the stream direction and the normal direction of the normal direction of the surface (Figure 2.5). The velocities of the entering particles are sampled from the Boltzmann distribution with the mean stream velocity and temperature.

Wall Surface

Phenomenological approaches are used to compute the collision between gas molecules with a solid surface.

(1) **Specular model** [45]: A specular reflection occurs when molecules collide with the surface without exchanging energy with the surface. The reflected velocity only depends on the pre-collision molecular velocity.

(2) **Diffusion model** [33]**:** In diffuse reflection, the molecules accommodate with the surface totally in the transient collision. The reflected velocity is independent of the initial velocity and can be sampled by the Maxwellian distribution using the surface temperature.

(3) **Cercignani-Lampis-Lord (CLL) model** [59]**:** The CLL model is a combination of specular model and diffusion model. The model implementation allows the normal energy, rotational energy and tangential momentum accommodation coefficients to be specified independently.

Plane of Symmetry

When particles strike a plane of symmetry All molecules striking the boundary are specularly reflected.

Vacuum Interface

No molecule enters the flow and all molecules striking the boundary are removed from the computational domain.

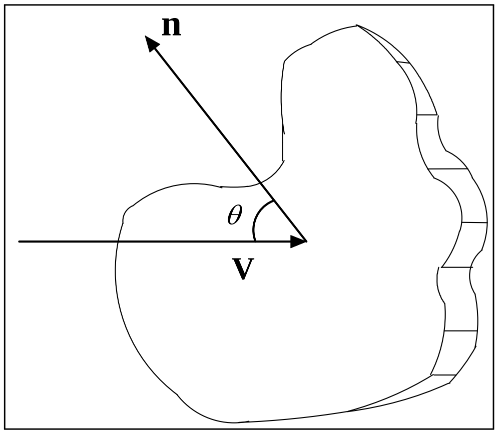

Figure 2.5. Stream flux across an element of surface

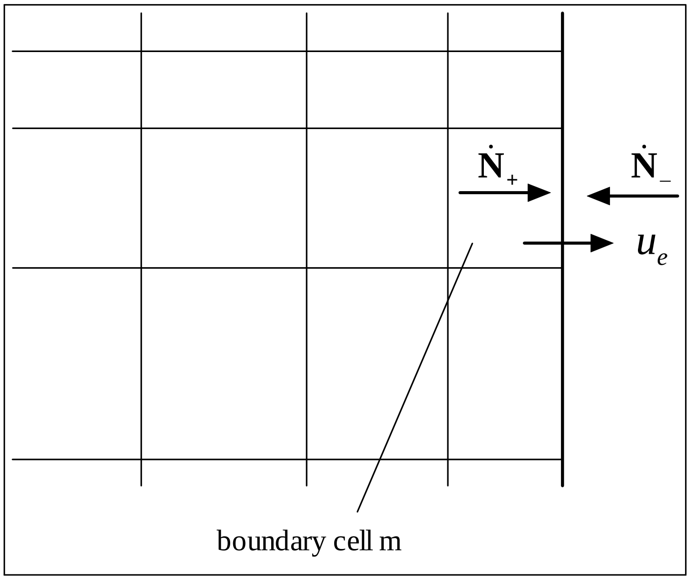

Figure 2.6. Illustration of Wu's Method

2.6 Implementation of the Background Boundary Conditions

The specified pressure boundary condition can not be directly applied to DSMC due to the particle nature of the method. The pressure at the boundary needs to be converted into the velocity, density, and energy for the particles at the boundary cells. This always requires the definition of a secondary stream, which is the stream that flows into the computational domain from the background. Several works have been done for the pressure boundary condition implementation in DSMC method by using an "particle conservation" iterative flux method [24–26]. The present approach follows the "particle conservation" procedure in Wu [26]. In this method, an implicit iterative scheme is used to introduce the background particles entering into the flow region at the boundaries between the background and the region of the flow. In this procedure, the mean velocity, u_e, and the average number of particles leaving the computational domain, $\dot{N}_+$, are first obtained from the calculations in the previous time step for each boundary cell "m" (Figure 2.6). Then, the number of particles $\dot{N}_-$ entering each boundary cell in the current time step is calculated by applying the conservation of particle fluxes under the specified pressure and temperature boundary conditions:

$$(u_e)_m^t = \frac{\left(\dot{N}_+^t - \dot{N}_-^{t-\triangle t}\right)}{n_b A} \ , \tag{2.33}$$

where A is the area on a downstream boundary cell, and the downstream number density n_b is calculated as

$$n_b = \frac{P_b}{kT_b} \ , \tag{2.34}$$

where P_b and T_b are the pressure and temperature at the downstream boundaries. Thus, for each boundary cell, the particles entering the flow region from the background are introduced by sampling from a Maxwellian distribution with the calculated mean flow velocity u_e and the background temperature.T_b.

Although Cai and Boyd [60] argued that this method could cause statistical error in the flow field, the method has been successfully used for the several simulations. In this study, to further reduce the statistical error, the calculated mean flow velocities in the boundary cells are averaged over time.

2.7 Parallel Implementation

The DSMC method is always computationally expensive, especially for 3D problem. Improved performance can usually obtained through parallel execution. Because of the particle nature, the DSMC algorithm is readily parallelized through domain decomposition. Computational grid is built for each domain and the particle movement and collisions are calculated in each domain. Parallel communication occurs only when particles cross domain boundaries. Figure 2.7 is a typical flow chart for a parallel DSMC code.

2.7.1 Parallel Efficiency

High parallel efficiency can be achieved if communication is minimized and the computation load is evenly distributed between processors. To minimize communication, the domain boundaries should lie along the streamlines of the flow field. This is always hard to achieve. Proper load-balancing can, to first order, be achieved by using an equal number of particles on each processor. The number of collisions occurring per processor has a second order effect on computational load. The number of cells assigned to each processor does not have a significant effect on efficiency.

2.7.2 Dynamic Domain Decomposition

When the flow does not reach the steady state, the particle resolution is changed during the computation. To equally distributed the computational load to each process, the decomposition of the domain should be changed during the calculation. A simple dynamic domain decomposition technique is going to be used. In the simulation of interacting jets, if the jets are exhausting in x-direction, the domain is only be decomposed in y- and z- directions to reduce the communication as shown in Figure 2.8. Firstly, the computational domain is decomposed in y-direction. The block boundaries are selected so that the particles are equally distributed to each block. Then for each block decomposed in the first step, the block is again decomposed in z-direction to ensure the particles are equally distributed. After the domain is decomposed, the computational cell in each sub-domain is re-created and the particles are re-sorted. The particles which are not in the current block will be transferred to the corresponding sub-domains.

2.7.3 Adaptive Mesh

In DSMC, the grid cell size should be smaller than the local mean free path. For the case of jet simulation, the local mean free path is significantly varied in the flow field. Therefore, adaptive mesh should be used to increase accuracy and efficiency. A simply 2-level structure adaptive mesh will be applied in the code (Figure 2.9). The simulation starts from a coarse 1st-level cells until the simulation reaches the steady state. The local mean free path length in each cell can be calculated. Then, a number of 2nd-level grid cells is created in each 1st-level grid. The size of the 2nd-level grid cell should be a fraction of the local mean free path calculated in the 1st-level cell. By using this method, the grid will be automatic refined for the region where the density is high. This grid refinement process can be executed several times in the simulation.

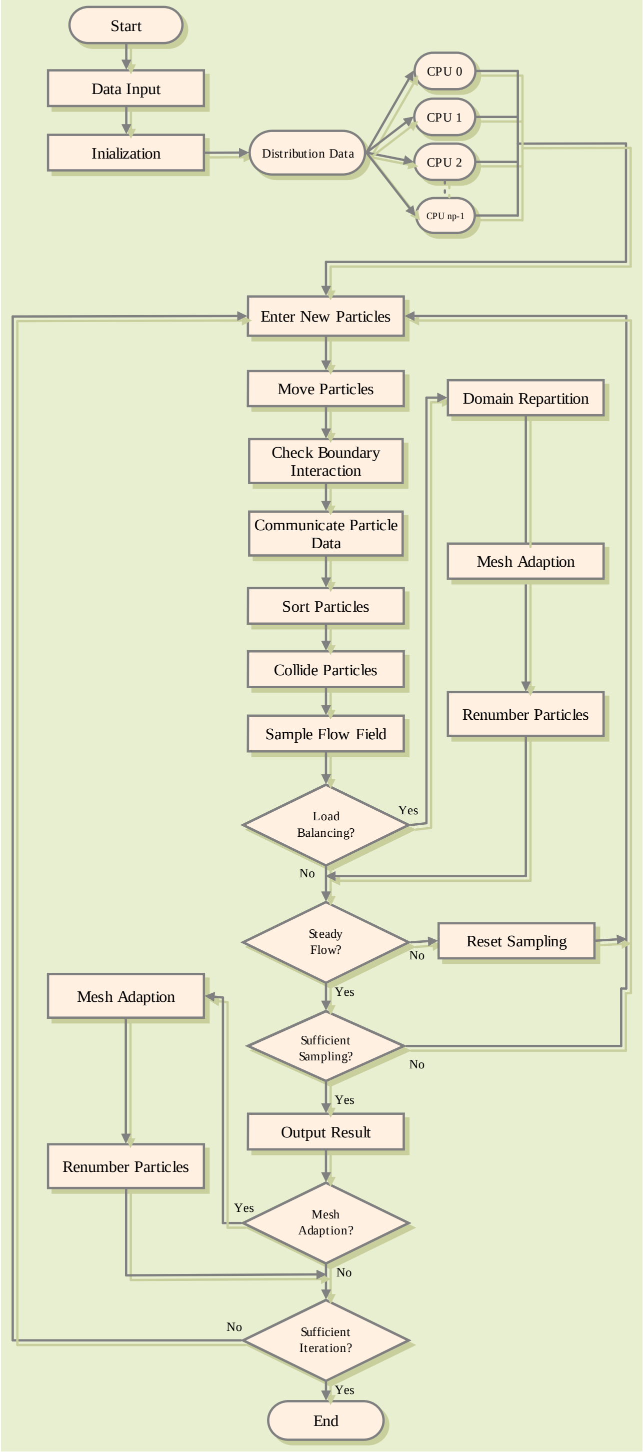

Figure 2.7. Flow chart for parallel DSMC code

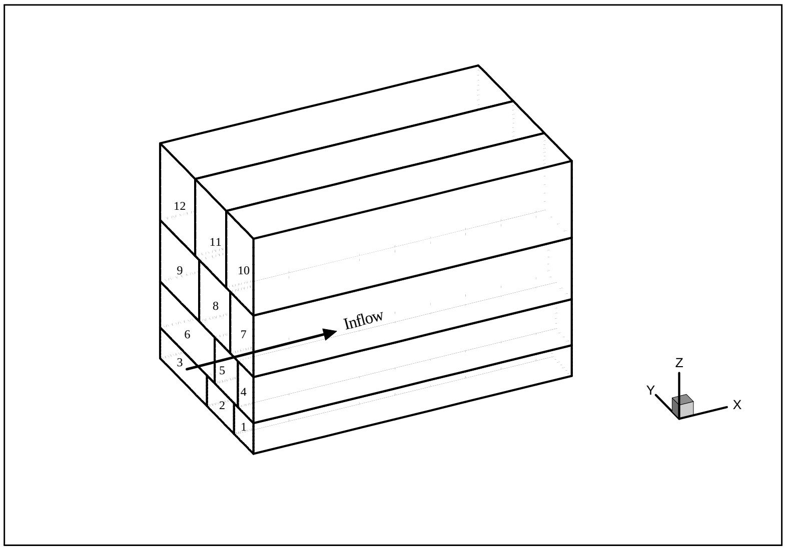

Figure 2.8. Illustration of dynamic domain decomposition

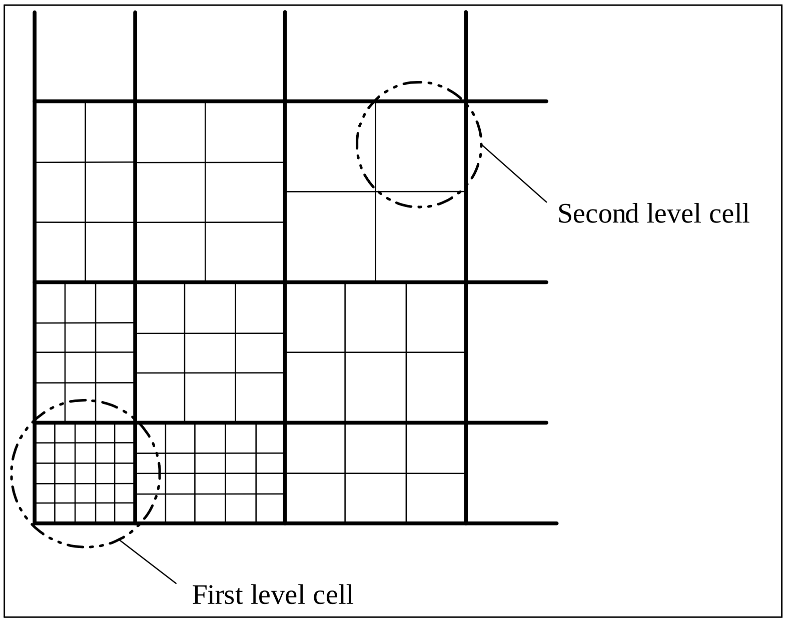

Figure 2.9. Illustration of mesh adaption

Chapter 3
One-Dimensional Shock Wave

For the one-dimensional normal shock wave, because of the sharp gradient of the flow properties in a very small region (small values of L in Equation (2.1)), high local Knudsen numbers can occur in strong shock waves at all gas densities. It has been proved that the traditional Navier-Stokes method can not resolve the detail shock wave structure if the shock wave Mach number $M_1 > 1.6$ [33]. There are many experimental data available for the structure of normal shock wave [61–64], and therefore, this flow become a very important test case for the theoretical [65–67] and numerical studies [68–71] of rarefied gas dynamics. For monotonic gas ($\gamma = 5/3$), as M_1 becomes larger, the shock wave thickness becomes smaller and the parallel temperature $T_{||}$ (calculated by the thermal velocity in the direction of shock propagation) deviates from the normal temperature $T_{\perp}$ (calculated from the thermal velocity in the normal direction of the shock propagation) [33, 72]. For diatomic gas ($\gamma = 7/5$), additional rotational degree of freedom needs to be considered. The breakdown of the thermal equilibrium between the translational and rotational degrees of freedom is also observed [73–76]. There is a significant lag of the rotational temperature T_r profile to the translational temperature T_t profile. If the M_1 is high, the distribution of the rotational energy also becomes non-maxwellian [77].

The one-dimensional normal shock wave was used as a benchmark because of its relevance to the Mach disk formed in the under-expanded jet problem. Upstream Mach number

M_1 values in range of 1.5 to 10.0 are simulated for argon and nitrogen. The upstream temperature T_1 is 273 K and pressure P_1 is 50 mtorr. The downstream boundary condition is set as a specularly reflecting wall moving with the Rankine-Hugoniot speed. The domain runs from -20 to 20, after being normalized by the upstream mean free path λ_1, which is calculated as [33]

$$\lambda_1 = \frac{16}{5}\left(\frac{1}{2\pi R T_1}\right)^{1/2} . \tag{3.1}$$

Table 3.1 summarizes the conditions used for the DSMC calculation for argon ($M_1 = 9$) and nitrogen ($M_1 = 10$).

Table 3.1. Parameters for the DSMC calculation of normal shock wave

Parameter	**Argon**	**Nitrogen**
Mach number of shock wave (M_1)	9.0	10.0
Number of particles after steady	$34,050$	$36,653$
Number of cells	400	400
Upstream number density (n_1)	1.61×10^{20}	1.61×10^{21}
Upstream Temperature (T_1)	300K	300K
Upstream mean free path length (λ_1)	1.09319mm	1.01453mm
Reference Temperature (T_{ref})	273K	273K
Reference Viscosity (μ_{ref})	2.117×10^{-5}N·s/m^2	1.656×10^{-5}N·s/m^2
Temperature exponent ω for $\mu = \mu_{ref}\,(T/T_{ref})^{\omega}$	0.81	0.74
Exponent in VSS model (α)	1.40	1.36
Rotational collision number (Z_r)	N/A	5
Time step size ($\triangle t$)	0.75×10^{-6}s	0.75×10^{-6}s
Time steps to reach steady	$40,000$	$40,000$
Time steps for sampling after steady state	$60,000$	$60,000$

3.1 Argon Normal Shock Waves

Because there is no internal degrees of freedom, the normal shock wave structure for a monotonic gas was carefully studied. Several analysis were developed based on the approximate solution of Boltzmann equation. Mott-Smith [65] used the moment method by assuming a bimodal velocity distribution function and found the density profile as

$$\frac{\rho - \rho_2}{\rho_1 - \rho_2} = \frac{1}{1 + \exp\left\{\alpha\left(x/\lambda_1\right)\right\}}\ , \tag{3.2}$$

where α is a function of shock Mach number M_1 and the subscripts "1" and "2" represent values in upstream of downstream of the shock wave. Figure 3.1 compares the DSMC-generated density distribution for $M_1 = 9$ argon shock wave with that from the experimental results by Alsmeyer [68] and data calculated by Mott-Smith's approximation (Equation (3.2)). Agreement is evident although the DSMC result shows a slight dissipation. Because the velocity difference between the x-direction and normal direction components of the thermal velocity, the parallel temperature T_x (based on x-direction thermal velocity) deviates from the normal temperature T_n (based on the thermal velocity on y- and z-directions). Figure 3.1 also plots the distributions of T_x, T_n, and the overall temperature T. The strong nonequilibrium between T_x and T_n is observed due to the high shock wave Mach number. While T_x reaches a maximum value that is almost one-fifth higher than downstream temperature T_2, T_n approaches T_2 monotonically.

Figure 3.2 shows the reciprocal shock wave thickness (λ_1/L) for the argon shock waves, where L is defined as

$$L = \frac{(\rho_2 - \rho_1)}{(d\rho/dx)_{\max}} \; . \tag{3.3}$$

The DSMC results are compared with several experimental data. Excellent agreement is evident for Mach numbers less than 3, with visible dissipation at the higher Mach numbers. Even then, the computed results for these high Mach number cases compare well with the data from Camac [63].

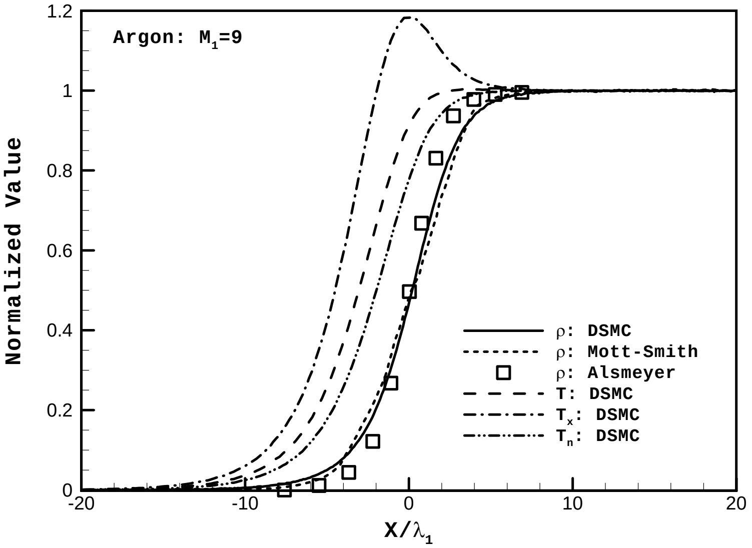

Figure 3.1. Normalized density and temperature distributions in an argon normal shock wave ($M_1 = 9$)

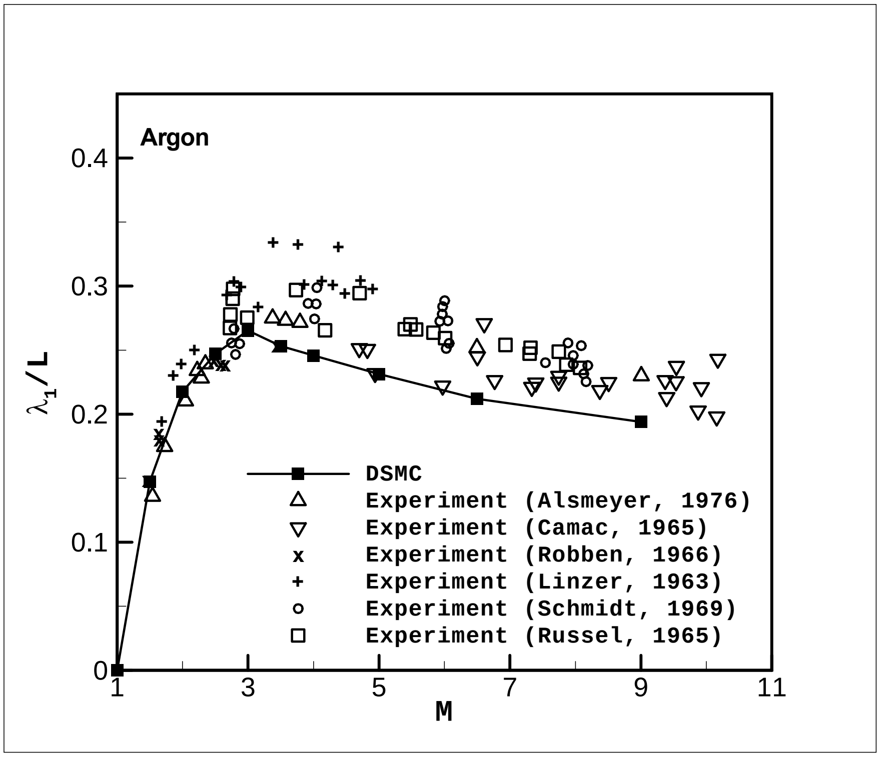

Figure 3.2. Calculated argon shock wave reciprocal thickness compared with data from several experiments.

3.2 Nitrogen Normal Shock Waves

For nitrogen shock wave, which is diatomic, the additional rotational degrees of freedom must be considered. Since the rotational collision number $Z_r > 1$, the rotational temperature T_r must lag behind the translational temperature T_t. In Figure 3.3, the density and rotational temperature obtained from the present DSMC calculations of nitrogen normal shock (using $Z_r = 5$) are compared with the experimental data from Robben and Talbot's [73] for $M_1 = 1.71$, 7, and 12.9. Compared with λ_1, $L^* = \mu\left(T^*\right)/\rho u$ is used as the reference length, where the superscript "*" represents values at sonic speed ($M = 1$). The conversions between L^* and λ_1 in the current calculations are given by $L^*/\lambda_1 = 0.40463$, 0.48075, and 0.61325 for $M_1 = 1.71$, 7.0, and 12.9, respectively. Also The agreement between the numerical results and the experimental data is quite good. The translational temperature T_t obtained from the calculation is also shown to illustrate the nonequilibrium between T_t and T_r. It shows that even for a smaller shock Mach number ($M_1 = 1.71$), T_r profile lags to T_t profile and even lags slightly to the ρ profile. When the shock Mach number is large ($M_1 = 7$ and 12.9.), the ρ profile lags to the T_r profile and the gap between the two temperature curves becomes larger as M_1 increases.

Figure 3.4 shows the reciprocal shock wave thickness (λ_1/L) for the nitrogen shock waves. Good agreement with experimental data is evident.

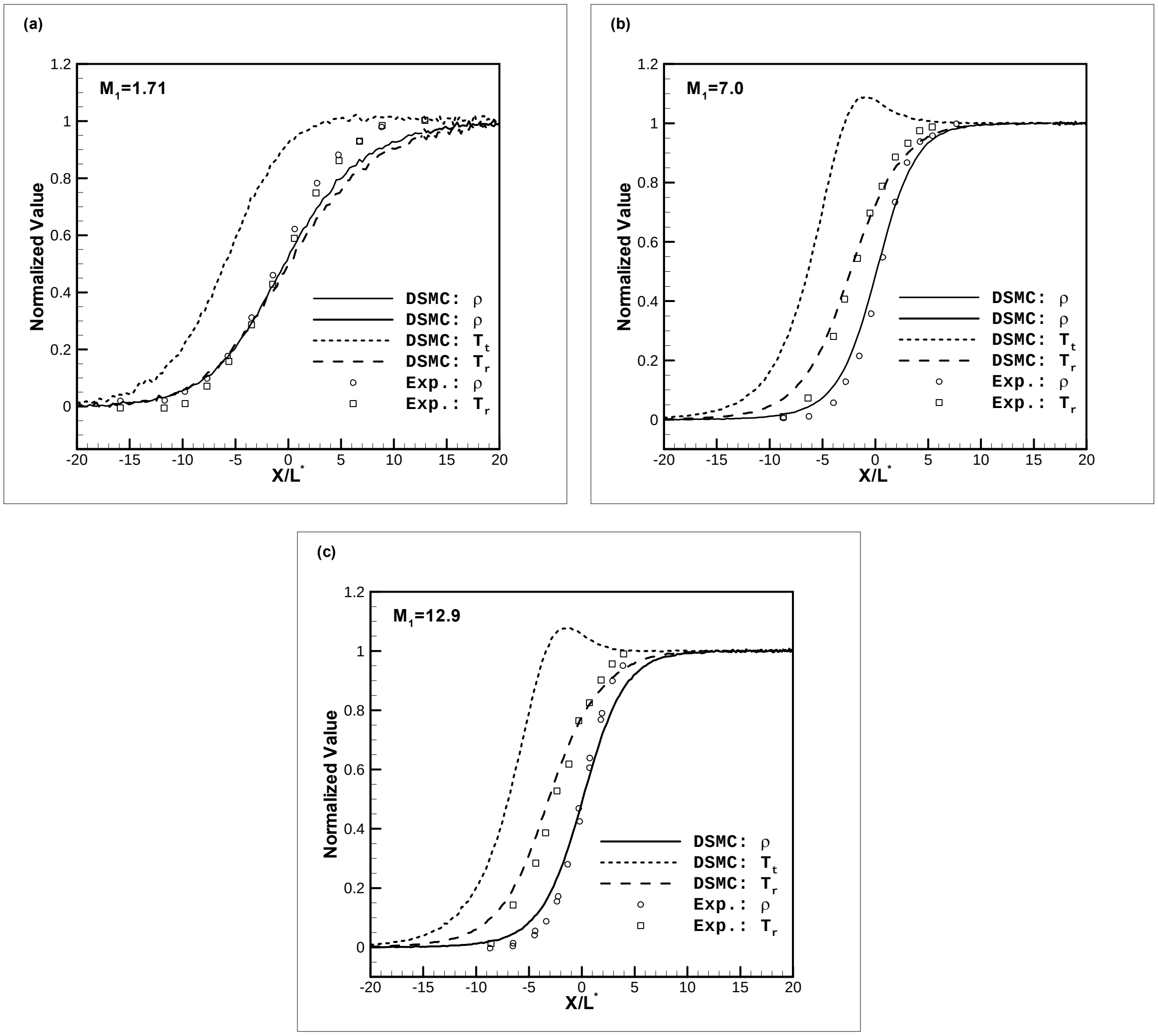

Figure 3.3. Normalized density and temperature distribution in nitrogen normal shock waves: (a) $M_1 = 1.71$; (b) $M_1 = 7.0$; (c) $M_1 = 12.9$.

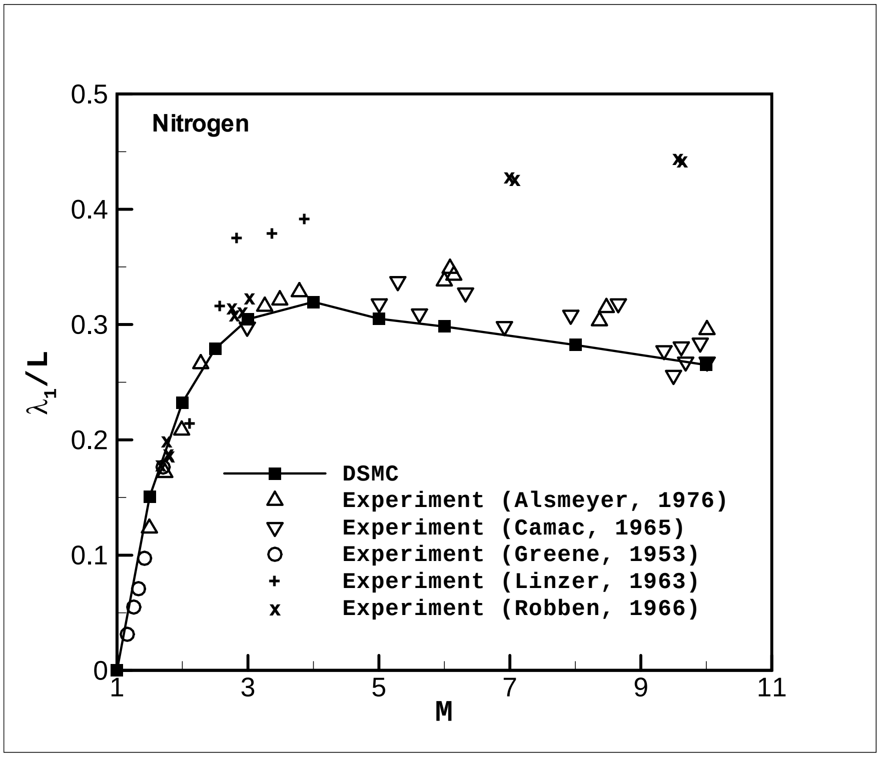

Figure 3.4. Calculated nitrogen shock wave reciprocal thickness compared with data from several experiments.

Chapter 4
Two-Dimensional Hypersonic Flow Past a Cylinder

A two-dimensional hypersonic nitrogen flow past a cylinder is also simulated for the purpose of validating the DSMC program. Figure 4.1 shows the computational domain. The calculations are made for a freestream Knudsen number $Kn_\infty = \lambda_\infty / D = 0.1$ and Mach number $M_\infty = 20$, where D is the cylinder diameter and $\lambda_\infty = \left(\sqrt{2}\pi d^2 n_\infty\right)^{-1}$. Both the upstream and cylinder temperature are fixed at 300 K. The cylinder is assumed to be a diffuse surface and the downstream boundary condition is assumed to be vacuum. The cell size is 800×250. Note that vibrational relaxation is important in this problem because of the high Mach number. Table 4.1 summarizes the parameters used to calculate the vibrational relaxation in DSMC.

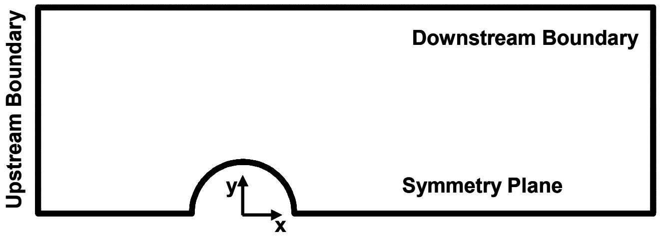

Figure 4.1. Computational domain for hypersonic flow past a cylinder

Figure 4.2 shows the normalized density, translational temperature, rotational temperature, and vibrational temperature contours for the flow. Very high temperature can be observed in the region just upwind of the cylinder. Therefore, the relaxation of the vibrational mode become very important. In Figure 4.3, our results are compared with Koura's [78] DSMC simulation results for the transverse distribution of density, translational, rotational, and vibrational temperatures at an axial distance of $X/D = 1$. The two calculations are in close agreement, with the exception of the vibrational temperature distribution. It shows that the vibrational temperature of the current calculation is somehow lower than Koura's results in the region close to the cylinder. This might be due to the fact that a simplified vibrational relaxation model, which only considers one active vibration mode is used in our code, compared with the more comprehensive EITFITS (extended improvement to forced oscillator, impulsive transfer semiclassical) model used by Koura for the vibrational relaxation in the region where temperature is very high. However, the under-expanded jet simulations in the present study is at room temperature and vibrational relaxation will be negligible. Figure 8 shows the contour maps of normalized number density, translational, rotational, and vibrational temperatures.

Table 4.1. Parameters used for the calculation of vibrational relaxation in nitrogen flows

Parameter	**Value**
The number of active vibration mode	1
Characteristic vibrational temperature (Θ_v)	$3371K$
Vibrational collision number $Z_v = (C_1/T^{\omega})\exp(C_2 T^{-1/3})$	$C_1 = 9.1$, $C_2 = 220.0$

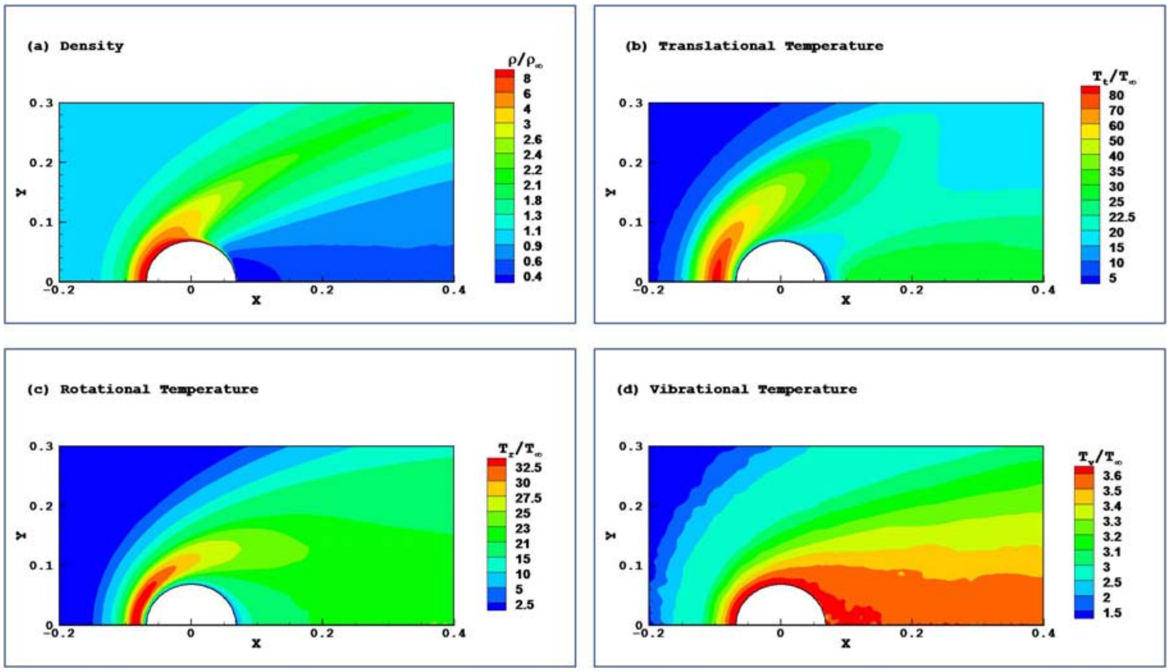

Figure 4.2. Normalized (a) density; (b) translational temperature; (c) rotational temperature; (d) vibrational temperature for a hypersonic nitrogen flow past a cylinder ($M_\infty = 20$, $Kn_\infty = 0.1$).

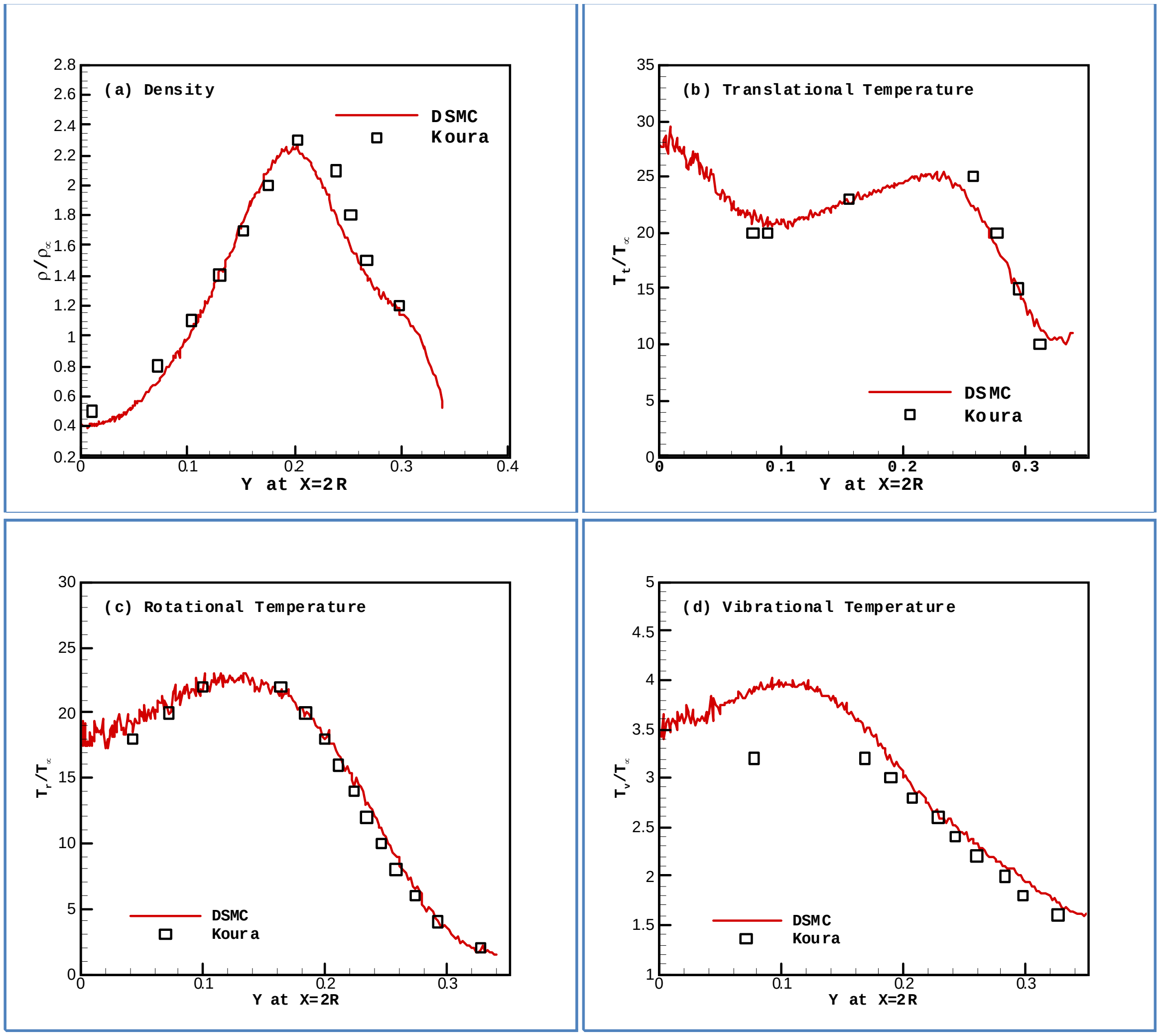

Figure 4.3. Results from the present calculation compared with Koura's [78] DSMC results for hypersonic flow past cylinder ($M_\infty = 20$, $Kn_\infty = 0.1$): (a) density; (b) translational temperature; (c) rotational temperature; (d) vibrational temperature. Note that results are shown as functions of the transverse coordinates (y) where longitudinal coordinate (x) is equal to D.

Chapter 5
Single Under-Expanded Jet

In this chapter, single under-expanded jets are studied by using DSMC approach. Both of jets issuing into vacuum and into a background with finite pressure are simulated. The stagnation pressure (P_s) and temperature (T_s) of the jet are 30 torr and 293 K. The background temperature (T_b) is set to the source stagnation temperature. A constant value of $Z_r = 4$ is used for nitrogen jets. Several values of stagnation-to-background pressure ratios (P_s/P_b): 20, 50, 100, 200, and values that approach infinity are investigated. Each case runs for three different values of the stagnation Knudsen number (Kn_s) of 0.05, 0.005, and 0.002, respectively. Therefore, the under-expanded jets in both the rarefied and near-continuum flow regimes are studied.

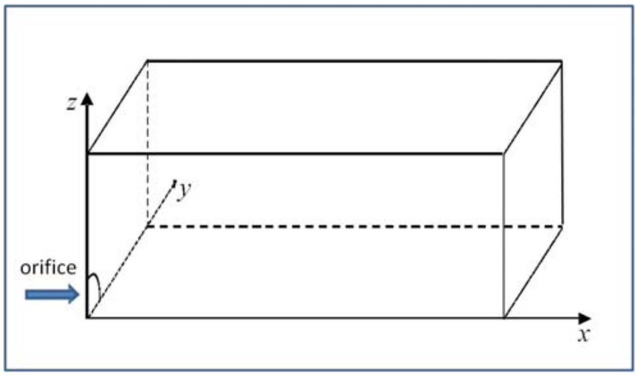

Figure 5.1. The computational domain for the DSMC calculation of under-expanded jets in this paper, showing a quarter of the full domain, assuming symmetry.

The geometry of the simulated region is shown in Figure 5.1. Only a quarter of the full physical domain is simulated based on the assumption of symmetry. The jet flow exhausts through a circular orifice located at the x=0 plane. The boundary conditions are set as follows:

(a) For the x=0 plane, sonic conditions are used for the particles entering through the orifice and the orifice plate is set to be a fully diffusive wall with a temperature value equal to the background temperature;

(b) Symmetry boundary conditions are imposed on both the $y = 0$ and $z = 0$ planes;

(c) The "particle conservation" method, which is introduced in Section 2.6 is used to specify the background pressure P_b and temperature T_b for all outflow boundaries.

Note that, to correctly specify the downstream boundary conditions, the size of the computational domain needs to be sufficiently large so that the influence of the jet plume is negligible at the downstream boundaries. Figure 5.2 shows the typical grid configurations for the DSMC calculations. Note that the sub-domains in Figure 5.2 are not equally-sized, as an automatic, adaptive domain decomposition is used to obtain parallel load balancing. The number of particles, not the physical size of the domain, determines the computational loads and hence the load balancing. For example, block 1 in Figure 5.2 contains the orifice where the density is large and hence, the number of simulated particles is large, whereas block 16 is in a more rarefied region where the number of particles is relatively small. The number of the simulated particles and grid cells used for each simulation are also shown in Table 5.1.

Table 5.1. Case studies for the DSMC simulation of single under-expanded jets

Case	Kn_s	P_s/P_b	**CPUs**	**Orifice Diameter** (m)	$\xi\ (\frac{dynes}{cm \cdot K})$	**Size of Domain**	**Particle Weight**	**No. of Particles**	**No. of Cells**
1	0.05	∞	16	2.73957×10^{-5}	0.0000	$25D \times 6D \times 6D$	1.302×10^{4}	4,149,620	484,652
2	0.05	200	16	2.73957×10^{-5}	0.0253	$25D \times 6D \times 6D$	2.170×10^{4}	6,465,380	542,346
3	0.05	100	16	2.73957×10^{-5}	0.0357	$25D \times 6D \times 6D$	4.894×10^{4}	8,787,720	605,248
4	0.05	50	16	2.73957×10^{-5}	0.0505	$20D \times 6D \times 6D$	8.684×10^{4}	10,450,762	663,736
5	0.05	20	16	2.73957×10^{-5}	0.0799	$18D \times 5D \times 5D$	2.605×10^{5}	14,256,128	727,352
6	0.005	∞	36	2.73957×10^{-4}	0.0000	$25D \times 6D \times 6D$	8.680×10^{5}	17,443,800	758,426
7	0.005	200	36	2.73957×10^{-4}	0.2527	$25D \times 6D \times 6D$	1.736×10^{6}	20,201,509	841,730
8	0.005	100	36	2.73957×10^{-4}	0.3574	$25D \times 6D \times 6D$	8.681×10^{6}	17,818,486	809,932
9	0.005	50	36	2.73957×10^{-4}	0.5055	$20D \times 6D \times 6D$	8.681×10^{6}	35,391,399	1,608,670
10	0.005	20	36	2.73957×10^{-4}	0.7922	$18D \times 5D \times 5D$	2.171×10^{7}	34,868,988	2,328,034
11	0.002	∞	36	6.83991×10^{-4}	0.0000	$25D \times 6D \times 6D$	1.953×10^{7}	12,124,814	1,348,216
12	0.002	200	36	6.83991×10^{-4}	0.6318	$25D \times 6D \times 6D$	6.510×10^{7}	25,142,704	2,285,702
13	0.002	100	36	6.83991×10^{-4}	0.8935	$25D \times 6D \times 6D$	9.766×10^{7}	32,296,781	2,691,398
14	0.002	50	36	6.83991×10^{-4}	1.2637	$20D \times 6D \times 6D$	5.208×10^{7}	93,928,219	6,261,882
15	0.002	20	36	6.83991×10^{-4}	1.9980	$18D \times 5D \times 5D$	1.563×10^{8}	78,154,987	5,086,774

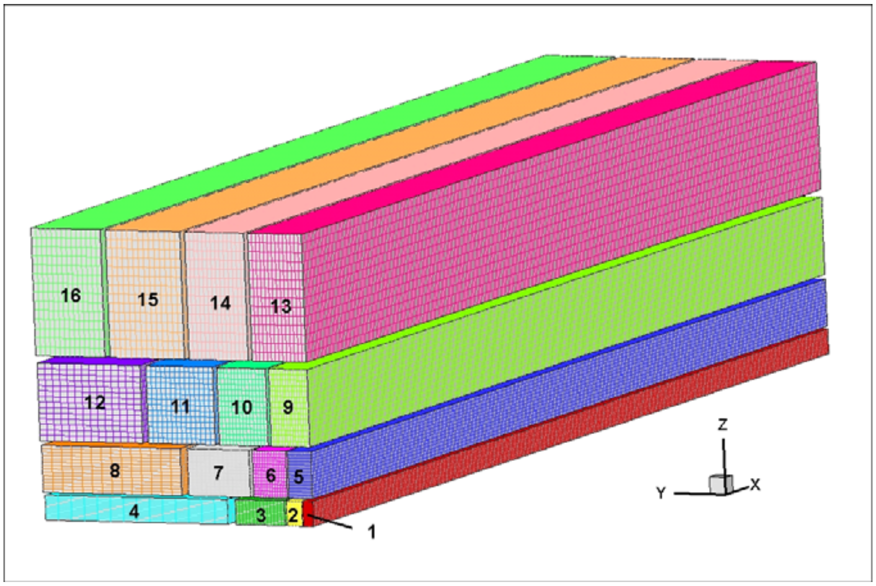

Figure 5.2. A typical grid for the DSMC simulation running on 16 CPUs

5.1 Single Jet Expanding into Vacuum

A supersonic jet expanding into vacuum is a fundamental test case for rarefied gas dynamics. The free rapid expansion results in a fast decay of density (large values of λ) and the local Knudsen number becomes larger as the jet flow propagating. There are many experimental and analytical studies available [79–83]. In the region close to the orifice, the flow density is still high and both density and temperature profiles follow the isentropic relations. When the distance from the orifice R becomes large, both curves deviate from the isentropic ones and the density profile continuously decays as $1/R^2$ due to the conservation of mass. While the circumferential direction temperature $T_{\perp}$ continuously decreases due to the decrease of density, the radial direction temperature $T_{||}$ decreases to a terminal value $T_{||,\infty}$ and remain unchanged [84–90]. This is the so-called "super cooling" effects. If the gas is not monotonic, the rotational temperature T_r also deviates from translational temperature T_t when R is large [91–101]. It was also noticed that the distribution function of the internal rotational modes may become non-maxwellian [102–105].

5.1.1 Rarefaction Parameter

For free jets expanding into vacuum ($P_s/P_b \longrightarrow \infty$) from a sonic orifice, the only flow parameter is the jet stagnation Knudsen number Kn_s, which is also related to the Reynolds number at the orifice exit, Re_D^*:

$$Kn_s = \frac{\lambda_s}{D} = \frac{k}{\sqrt{2}\pi d^2} \cdot \frac{T_s}{P_s D} = \frac{1}{\mathrm{Re}_D^*}\sqrt{\frac{\pi\gamma}{2}} \cdot \left(\frac{2}{\gamma+1}\right)^{\frac{1}{\gamma-1}} \ . \tag{5.1}$$

Therefore, for a free jet expanding into vacuum at a fixed temperature T_s, Kn_s (Re_D^*) is determined only by the product of P_s and D. This quantity (P_sD), with units of torr×mm, is frequently used in experiments to characterize sonic jet expansion.

Several researchers developed approximate asymptotic solutions for the jet density distribution, which is of the form [106–108]

$$\frac{n}{n_s} = A\left(\frac{D/2}{R}\right)^2 \cdot f\left(\theta\right) \ , \tag{5.2}$$

where R is the radial distance from the orifice and $f\left(\theta\right)$ is the angular distribution function, which has the form

$$f\left(\theta\right) = \cos^2\left(\frac{\pi}{2} \cdot \frac{\theta}{\theta_{\max}}\right) \ . \tag{5.3}$$

and A and θ_{max} are γ-dependent constants. For $\gamma = 1.4$, $A = 0.345$ and $\theta_{max} = 95.2^\circ$ [15].

5.1.2 Results and Validation

Marrone [92] and Mori [105] experimentally measured the centerline properties of free jets for the case where P_sD=torr×mm. The detail experimental conditions are shown in Table 5.2. This provides validation data for the present effort. In Figure 5.3, the density contours from the developed DSMC code and from AEROFLO [109] on the $Z = 0$ symmetry plane are compared. Excellent agreement is evident. AEROFLO is a compressible Navier-Stokes based multi-disciplinary CFD code that is based on high-order discretization in space and time. Since the vacuum boundary condition is not valid in AEROFLO, a very large computational domain (compared with the computational domain used in DSMC) is used for the AEROFLO model and Neumann boundary conditions are applied at the downstream boundary.

Table 5.2. Summary of the experiments of single jet expanding into vacuum

No.	Author	Year	Gas	P_s (torr)	D (mm)	T_s (K)	Re_D^*	Kn_s	M^*	Method
1	Mori	2005	N_2	30	0. 50	293	280	2.736×10^{-3}	1. 0	Resonantly Enhanced Multiphoton Ionization
2	Marrone	1967	N_2	3	5. 0	293	280	2.736×10^{-3}	1. 0	Electron Beam Fluorescence

In Figure 5.4, the density distribution along the jet centerline that is calculated with the DSMC code is compared with Marrone's experimental data, an asymptotic relation (Equation (5.2)), the isentropic relation, and the result from AEROFLO. The isentropic relation can be expressed as

$$\frac{\rho_s}{\rho} = \frac{n_s}{n} = \left(1 + \frac{\gamma - 1}{2} M^2\right)^{\frac{1}{\gamma-1}} \quad . \tag{5.4}$$

where M is the Mach number distribution within the expansion core, which can be approximated by [110]

$$M = (2.2)^{\frac{\gamma-1}{2}} \left[\gamma\left(\gamma - 1\right)\right]^{-\frac{\gamma-1}{4}} \left(\frac{\gamma + 1}{\gamma - 1}\right)^{\frac{\gamma+1}{4}} (X/D)^{\gamma-1} \quad . \tag{5.5}$$

Two DSMC calculations are shown: (a) $P_s = 3$ torr, $D = 5$ mm; and (b) $P_s = 30$ torr, $D = 0.5$ mm. According to Equation (5.1), these two calculations should give essentially the same results because the product $P_s D$ is the same. We can see in Figure 5.4 that this is indeed the case. Moreover, the Navier-Stokes simulations as well as the asymptotic distribution and the isentropic relation give the same density profile. The experimental data also agrees with these results for $X/D \lesssim 12$, with deviations further downstream. We believe the deviations are due to the inability to obtain perfect vacuum conditions in the experiment, whereas the various calculations had no difficulties enforcing an infinite value for P_s/P_b. Note, however, that the magnitude of the error in the measurement is exaggerated in Figure 5.4 because of the use of a log scale.

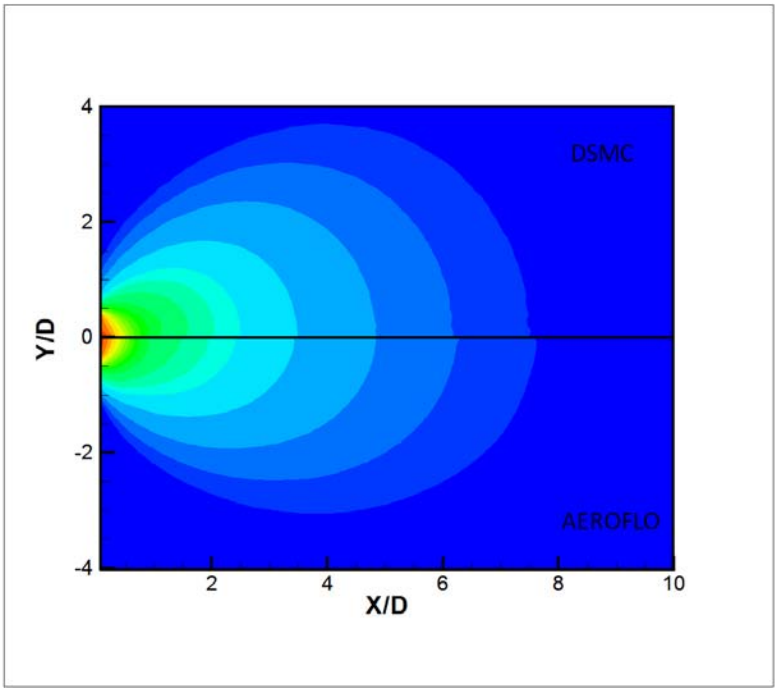

Figure 5.3. Density contour map on the Z=0 symmetry plane ($Ps/Pb \to \infty$, $P_sD = 15$ torr×mm) from the present DSMC calculations and from AEROFLO

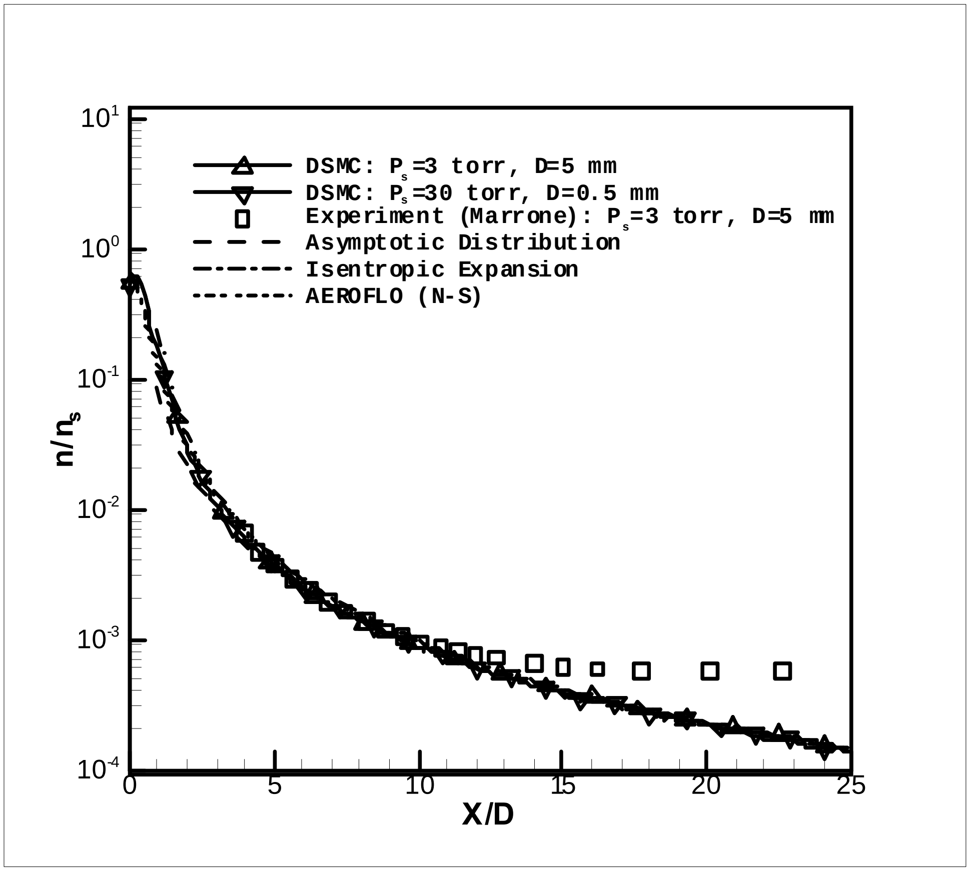

Figure 5.4. Comparison of calculated and measured density distribution along the centerline. The data comes from Marrone's experiments and continuum calculations from AEROFLO. Also shown are the DSMC results, the asymptotic distribution (Eqn. (5.2)), and the isentropic relation (Eqn.(5.4)). Two DSMC results with different flow conditions are shown.

5.1.3 Thermal Non-Equilibrium Effects

Figure 5.5 compares the DSMC results for translational temperature with the Navier-Stokes (AEROFLO) calculations and the isentropic relations, both of which are based on the continuum hypothesis. The isentropic relation can be expressed as

$$\frac{T_s}{T} = 1 + \frac{\gamma - 1}{2} M^2 \, . \tag{5.6}$$

We see that the two DSMC calculations with different P_s and D values but with the same values of $P_s D$ give identical results. We also observe that the continuum calculations (AEROFLO and isentropic relation) give progressively poorer results as X/D increases, due to increasing non-equilibrium effects downstream.

To evaluate the translational-rotational non-equilibrium effects, a simple model for predicting the axial decay of the rotational temperature, T_r, is developed below, starting from Equation (2.10). The equilibrium temperature T and number density n can be evaluated assuming isentropic conditions. Since $M \gg 1$ for most free jets when $X/D > 1$, we can write the equations for T and n as follows:

$$\frac{1}{\Phi}\begin{bmatrix} T \\ n \end{bmatrix} = \begin{bmatrix} T_s & 0 \\ 0 & n_s \end{bmatrix} \begin{bmatrix} \left(\frac{X}{D}\right)^{-2(\gamma-1)} \\ \left(\frac{X}{D}\right)^{-2} \end{bmatrix} = \frac{1}{\Phi}\begin{bmatrix} 0.378318 \times T_s \left(\frac{X}{D}\right)^{-0.8} \\ 0.0880324 \times n_s \left(\frac{X}{D}\right)^{-2} \end{bmatrix} \quad , \tag{5.7}$$

where

$$\Phi = \left(\frac{\gamma - 1}{2}\right) (2.2)^{\gamma-1} \left[\gamma\left(\gamma - 1\right)\right]^{-\frac{\gamma-1}{2}} \left(\frac{\gamma + 1}{\gamma - 1}\right)^{\frac{\gamma+1}{2}} \quad . \tag{5.8}$$

If we assume an adiabatic speed limit, $u_{\max}$, of [33]

$$u_{\max} = \left(\frac{2\gamma R T_s}{\gamma - 1} \right)^{1/2} \tag{5.9}$$

and the departure from equilibrium is small [95], we can estimate

$$\frac{DT_r}{Dt} \simeq \frac{DT}{Dt} = u_{\max} \frac{dT}{dx} = -1.38747 \times 10^7 \left(X/D \right)^{-1.8} \ , \tag{5.10}$$

using the conditions in Marrone's experiment and the temperature distribution in Equation (5.6). We further assume that τ can be given as

$$\tau = \frac{\pi \mu \left(T \right)}{4P} = \frac{\pi \mu \left(T \right)}{4nkT} \ . \tag{5.11}$$

Equating Equations. (2.10) and (5.10), we can express T_r as

$$T_r = 0.378318 \times T_s \times \left(X/D \right)^{-0.8} + 7.096326 \times \left(X/D \right)^{0.408} \times Z_r. \tag{5.12}$$

Note that we have used the power law relation between the dynamic viscosity and temperature, $\mu = \mu_{ref} \left(T/T_{ref} \right)^{0.74}$, where $\mu_{ref} = 1.656 \times 10^{-5}$ N·s/m^2 at $T_{ref} = 273$ K [33].

A model for the rotational collision number Z_r as a function of the translational temperature T_t is needed in order to evaluate T_r in Equation (5.12). Advantage is taken of previous relevant work in order to close the T_r model. Parker [38] developed the equation

$$Z_r = \frac{Z_r^{\infty}}{1 + \left(\pi^{3/2}/2 \right) \left(T^*/T_t \right)^{1/2} + \left(\pi + \pi^2/4 \right) \left(T^*/T_t \right)} \ , \tag{5.13}$$

with $Z_r^{\infty} = 15.7$ and $T^* = 80.0$ K for nitrogen. When the experimental results of Lordi and Mates [111] are used to fit this equation, the coefficient values are $Z_r^{\infty} = 23.0$ and

$T^* = 91.5$ K. This expression was subsequently corrected by Brau and Jonkman [112]:

$$Z_r = \frac{Z_r^\infty}{1 + (\pi^{3/2}/2)\left(T^*/T_t\right)^{1/2} + (2 + \pi^2/4)\left(T^*/T_t\right) + \pi^{3/2}\left(T^*/T_t\right)^{3/2}} \quad , \tag{5.14}$$

with $Z_r^\infty = 25.2$ and $T^* = 118.5$ K. These expressions are plotted in Figure 5.6 for temperatures up to 500 K.

In Figure 5.7, the DSMC results for the rotational temperature distribution along the jet centerline are compared with the experimental data and the prediction from Equation (5.12). Both the DSMC calculations and Equation (5.12) are carried out for $Z_r = 2$ and 5. Good agreement with the experimental results is evident for $Z_r = 2$. This is due to the fact that the value of Z_r depends on temperature (the higher the temperature, the larger value of Z_r). Since the flow temperature drops rapidly and $T \leq 100$ K when $X/D > 1$, $Z_r = 2$ is a more reasonable value for the experiments and, therefore, the numerical calculations, is evident from the translational temperature values, vis-a-vis, the Z_r distributions in Figure 5.6.

It is also interesting to study the so called "super cooling" effects, which refers to the non-equilibrium between the components of the translational temperature in different directions. It has been observed that, for a free jet expanding into vacuum, while the circumferential direction temperature $T_\perp$ continuously decreases due to the decrease of density, the radial direction temperature $T_{||}$ decreases to a terminal value $T_{||,\infty}$ and remain unchanged. Figure 5.8 plots the centerline temperature distributions of the argon jet flow and it does show this non-equilibrium behavior. There are several analysis of this non-equilibrium effects by using a sudden freeze model. It can be shown that the $T_{||,\infty}$ and decay rate of is $T_{\perp}$ a function of Kn_s (or P_sD).

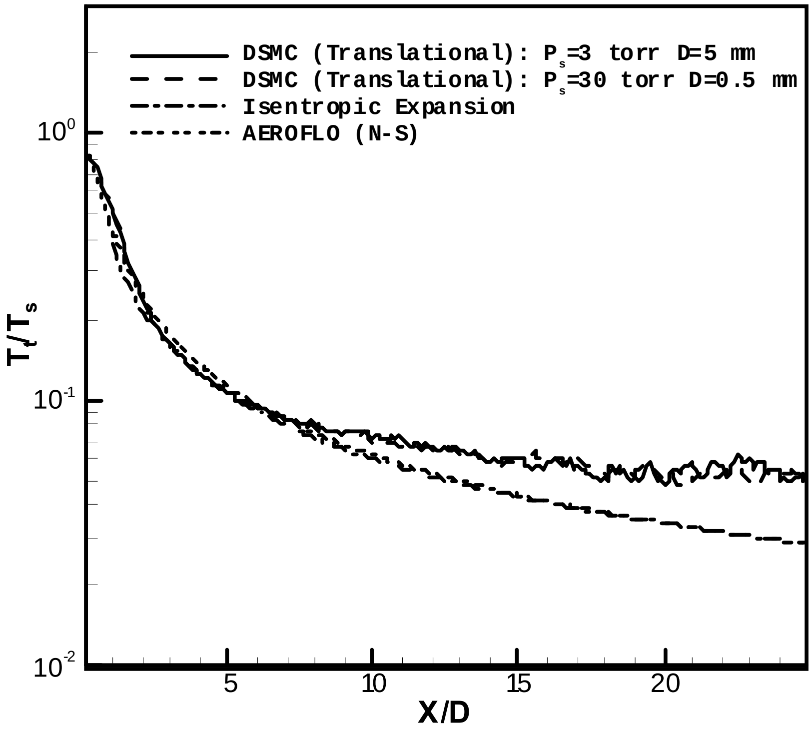

Figure 5.5. Comparison of translational temperature distribution along the centerline from DSMC simulation and continuum calculation using AEROFLO. The isentropic expansion relation is also shown, as are DSMC results with different flow conditions.

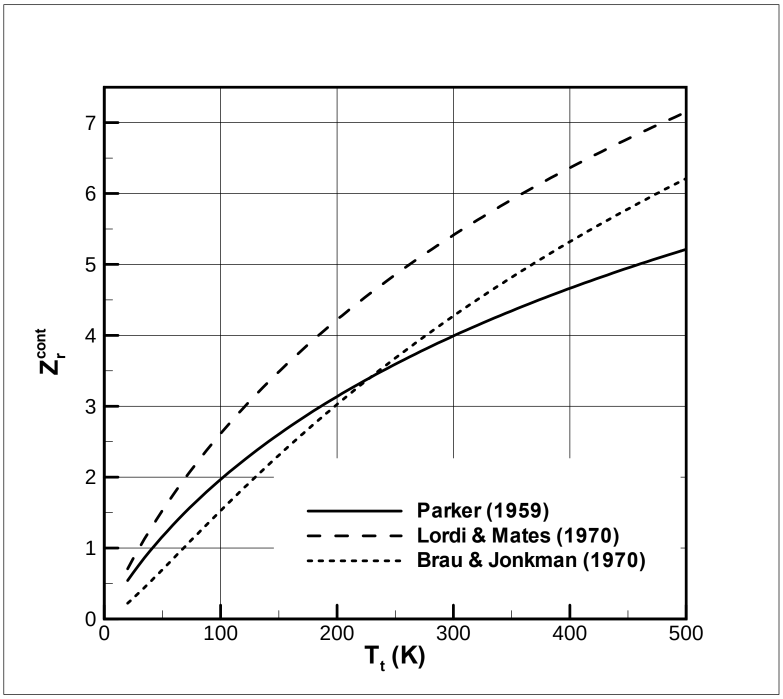

Figure 5.6. Plot of nitrogen rotational collision number Z_r as a function of temperature.

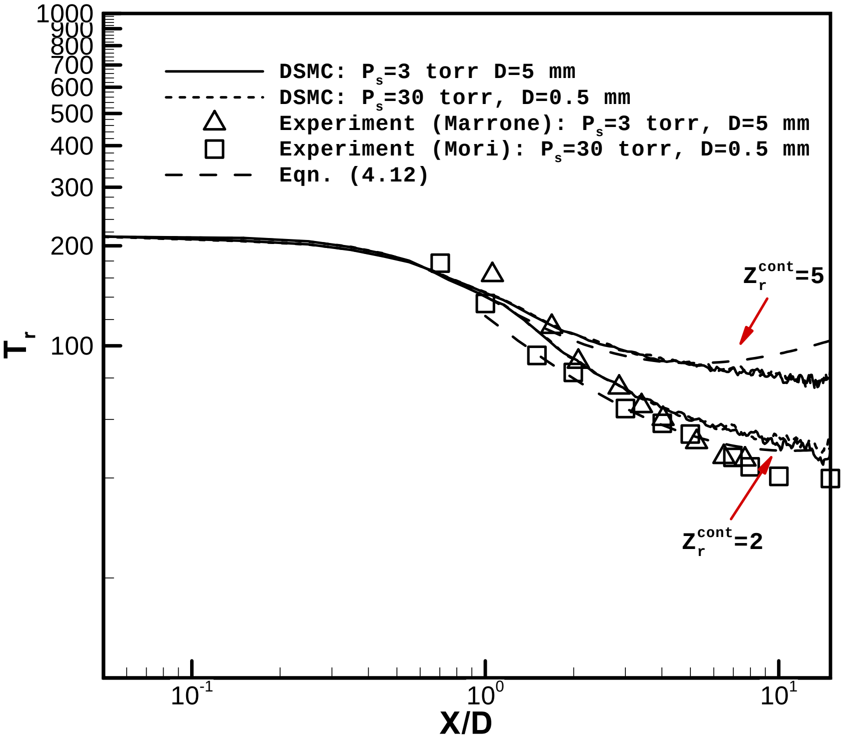

Figure 5.7. Comparison of calculated DSMC rotational temperature distribution along the centerline with Marrone and Mori's experimental data, and with the simple rotational temperature decay model (Eqn. (5.12)). Note that both DSMC and Eqn. (5.12) are calculated for $Z_r = 2$ and $Z_r = 5$

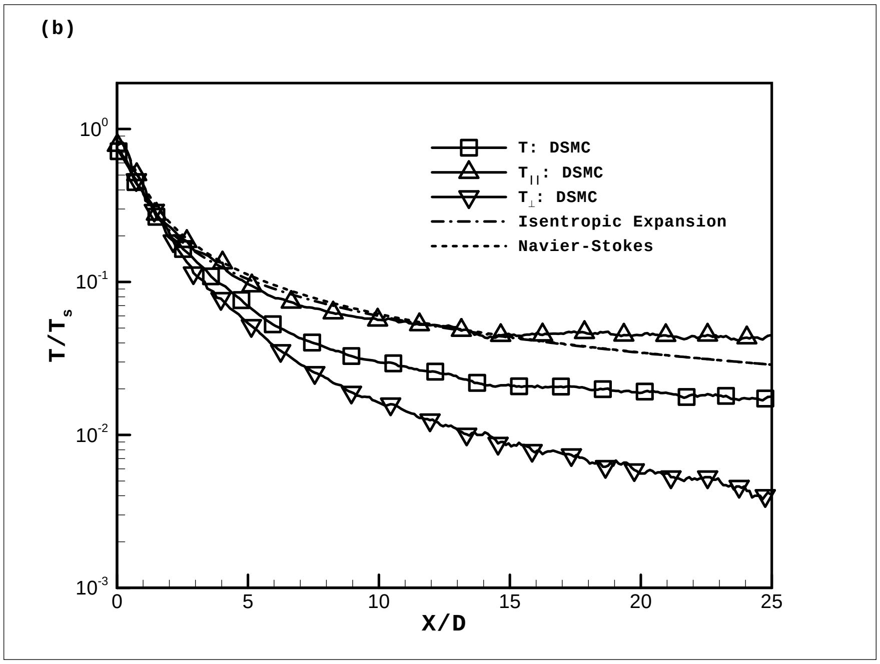

Figure 5.8. Centerline temperature distribution for an argon free jet expanded into vacuum ($P_s D = 15$ torr×mm)

5.2 Single Jet Expanding into a Region with Finite Pressure

Rather than expanding into vacuum, when the jet expands into a region of finite ambient pressure, a more complicated flow structure results due to the interaction between jet flow and the background gas. Because the jet exhausting conditions could vary for different pressure levels (such as rocket exhaust at different altitudes) [113], and applications could vary from very large scales (such as a power plant) [114] to very small scales (such as a micro-jet in MEMS device) [115], under-expanded jets may be observed in the entire flow regimes, i.e., from the free molecular regime to the continuum regime.

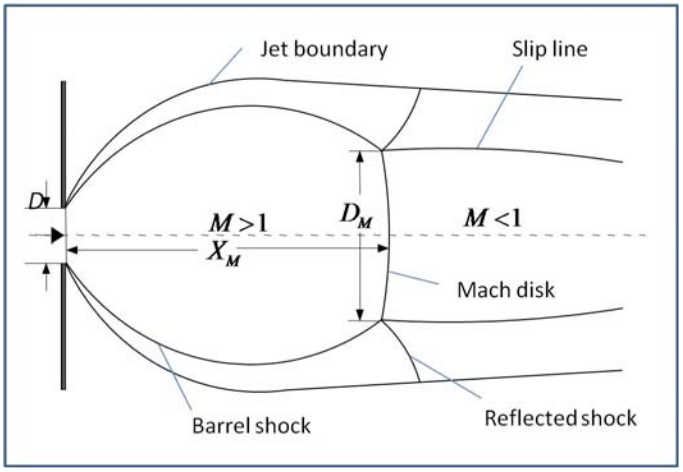

Figure 5.9. The shock structure from an under-expanded sonic jet issuing from an orifice

At high levels of the background pressure (P_b) and small values of the jet stagnation Knudsen number (Kn_s), the plume is in the continuum flow regime. In this case, the plume expands around the orifice exit to form an inertia-dominated region of isentropic high Mach number flow, which is sometimes called expansion core. Due to the strong interaction between the jet and the background gas, a normal shock wave (Mach disk) and barrel shocks, which take on a concave curvature, are formed. This “shock-cell” structure is shown in Figure 5.9.

There have been many analytical and experimental studies on under-expanded jets, and most of them focus on the shock structures in the continuum flow regime. The method of characteristics [79–81, 106–108] was used to predict the inviscid jet boundary. The location and size of the Mach disk were also extensively measured in experiments [110, 116–124]. Empirical correlations for the location and diameter of the Mach disk were given by Ashkenas [118] and Crist [120]:

$$X_M/D = 0.67\,(P_s/P_b)^{1/2} \tag{5.15}$$

and

$$D_M/D = 0.24\,(P_s/P_b)^{1/2}\ . \tag{5.16}$$

Electron beam fluorescence method [125] was firstly used to measure the density and temperature distributions along the centerline of the jets. The Raman [126] or Rayleigh scattering [127] technique have been widely used in later studies. Recently, Venkatakrishnan [128] and Kolhe [129] made a complete density mapping of the jets by using background-oriented Schlieren and miniature rainbow schlieren deflectometry technique, respectively. Naik [130] also measure the pressure, density, and velocity along the jet centerline by using Planar laser-induced fluorescence imaging. There are also many numerical simulations of the under-expanded jets in continuum regime by solving the Navier-Stokes equations [131–141].

When background pressure P_b is smaller and jet stagnation Knudsen number Kn_s is large, the plume becomes rarefied. The thickness of the shock waves increases and the mixing zone is enlarged. Since the plume contains both supersonic expansion region (expansion core) and shock waves (Mach disk, barrel shock), the thermal non-equilibrium effects become more complicated. Although there are many studies of under-expanded jets in continuum flow, only a few of studies analyzed the under-expanded jets in rarefied flow regimes. Muntz [142] used the electron beam fluorescence method to show the differences of the flow structures in different flow regimes. The penetration of the background gas into the jet flow were also studied theoretically by Brook [83, 143, 144]. Several researchers also used the DSMC method to study the rarefied under-expanded jets [27, 29, 145–148]. There are also other numerical methods to calculate the under-expanded jets in all flow regimes. Ivanov [149] proposed a hybrid approach that combines the DSMC method with Navier-Stokes equations for different parts of the flow field. Wang and Boyd [150] and Ladeinde et al. [21, 22] have also reported on hybrid methods for rarefied flows. However, all of these studies focused on how the flow shock structures are changed due to rarefaction effects rather than the thermal nonequilibrium effects in rarefied under-expanded jets. To the author's knowledge, the quantitative studies of the thermal nonequilibrium effects for a rarefied under-expanded jet is still scarce. Therefore, this study focuses the analysis of the nonequilibrium effects for rarefied under-expanded jets.

5.2.1 Rarefaction Parameter

The interaction between the jet molecules and the molecules of background gas were studied for single under-expanded jets by Muntz [125]. A rarefaction parameter ξ was proposed as

$$\xi = D\left(P_s P_b\right)^{1/2}/T_s\ , \tag{5.17}$$

to characterize this interaction. It can be shown that this parameter is inversely proportional to the square root of the pressure ratio P_s/P_b and stagnation Knudsen number Kn_s:

$$\xi = \frac{k}{\sqrt{2}\pi d^2} \cdot \frac{1}{\left(P_s/P_b\right)^{1/2} Kn_s} = \frac{k}{\sqrt{2}\pi d^2} \cdot \sqrt{\frac{2}{\pi\gamma}} \cdot \left(\frac{\gamma+1}{2}\right)^{\frac{1}{\gamma-1}} \cdot \frac{\mathrm{Re}_D^*}{\left(P_s/P_b\right)^{1/2}}\ . \tag{5.18}$$

Therefore, the rarefaction effects for the jets expanding into vacuum depend on two parameters: Kn_s and P_s/P_b.

In addition to the rarefaction parameter ξ defined in Equation (5.17), we can introduce a new parameter, Kn_p, the background molecular penetration Knudsen number, to evaluate the penetration of the background gas into the jet flow. It is defined as (shown in Figure 5.10):

$$Kn_p \equiv \frac{r_p}{l^*}\ , \tag{5.19}$$

where r_p is the background molecular penetration length (measured from the source), which is given by

$$r_p = \frac{\pi d^2 u_{\max} n^* D^2}{4 c_b'} \qquad , \tag{5.20}$$

and l^* is a characteristic plume dimension, which is given by

$$l^* = \left[\left(F/P_b \right) \left(u_{\max}/u^* \right) /2\pi \right]^{1/2} \ . \tag{5.21}$$

Note that r_p is actually the minimum axial distance from the orifice to where a background molecule can be found. F is the jet thrust calculated as

$$F = \frac{\rho^* \left(u^* \right)^2 \pi D^2}{4} \qquad , \tag{5.22}$$

where ρ^* is the velocity at the orifice exit and D is the orifice diameter. c_b' is the thermal velocity of the background molecules:

$$c_b' = \frac{2}{\sqrt{\pi}} \sqrt{2RT_s} \ . \tag{5.23}$$

This allows us to write Kn_p as

$$Kn_p = \frac{\pi^{3/2} d^2}{4 \left(mkR \right)^{1/2}} \left(\frac{\gamma+1}{\gamma-1} \right)^{1/4} \left(\frac{2}{\gamma+1} \right)^{\frac{1}{2(\gamma-1)}} \cdot \xi \ . \tag{5.24}$$

It shows that Kn_p reproduces the rarefaction parameter ξ, which indicates that ξ is indeed a measure of how far the background gas can penetrate into the jet flow.

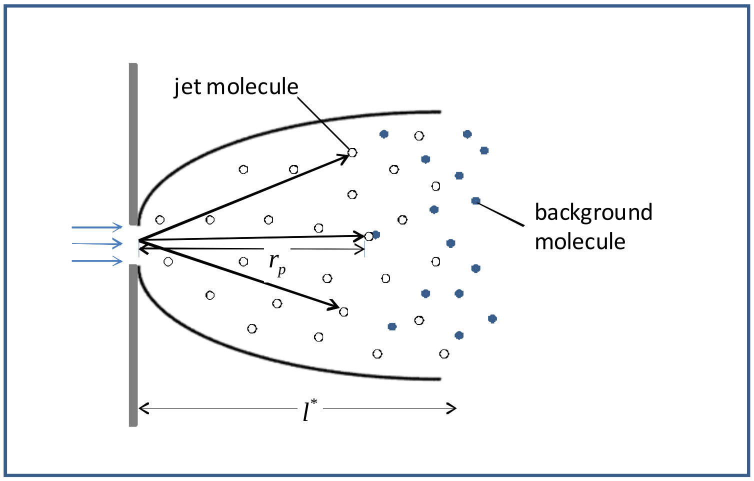

Figure 5.10. Scales used in the definition of $Kn_p = r_p/l^*$, where r_p is the background molecular penetration distance (measured from the orifice) and l^* is a characteristic plume dimension.

Figure 5.11 shows the contour maps of the normalized density, translational temperature, rotational temperature, and the Mach number when the jet has the parameters $Kn_s = 0.002$, $P_s/P_b = 50$. Compared with the Figure 5.3, the existence of the background gas significantly changes the flow structure. In this case, although the flow is still rarefied and the shock structure is much dissipated, the "shock-cell" structure (Figure 5.9) can still be observed from these figures, especially in the Mach number and temperature contours. Slight difference can also be observed in the translational and rotational temperature contours. This translational-rotational non-equilibrium is expected since the inter-molecular collision frequency is too low to balance the translational and rotational temperature.

Figure 5.12 presents the same contour maps for $Kn_s = 0.002$, $P_s/P_b = 100$. The effects of P_s/P_b can be seen by comparing with Figure 5.11. The most obvious observation is the significant difference in the transverse (y) scale of the shock structure, with the larger pressure ratio case ($P_s/P_b = 100$) showing the larger size. This is consistent with the experimental observation that the diameter of the Mach disk scales with the square root of the pressure ratio. According to Equation (5.16), this length scale in the large pressure ratio should be $\sqrt{2}$ times greater than the smaller, which is consistent with the observations in these figures. Also, with higher value of P_s/P_b, the Mach disk is located further downstream of the plume.

Figure 5.13 also presents the same contour maps but for $Kn_s = 0.05$, $P_s/P_b = 50$. Compared with Figure 5.11, a larger value of Kn_s indicates that the plume is much more rarefied and the interaction between the molecules of the jet and the background gas molecules could be neglected. Therefore, no shock waves are formed. Also, significant non-equilibrium between the translational temperature and rotational temperature fields can be observed.

Figure 5.14 shows the contour maps of normalized density in the $Y - Z$ plane for $Kn_s = 0.005$, $P_s/P_b = 20$ and $X/D = 1.0$, 2.0, 6.0, and 12.0. The location $X/D = 1.0$ is very close to the jet exit, with a solution field that is similar to the uniform distribution specified at the orifice. The location $X/D = 2.0$ is in the isentropic core, where the density is relatively low because the flow there is supersonic. The location $X/D = 6.0$ is downstream of the Mach disk ($X_M/D \simeq 3$). The density becomes higher because the flow becomes subsonic. This trend continues at $X/D = 12.0$.

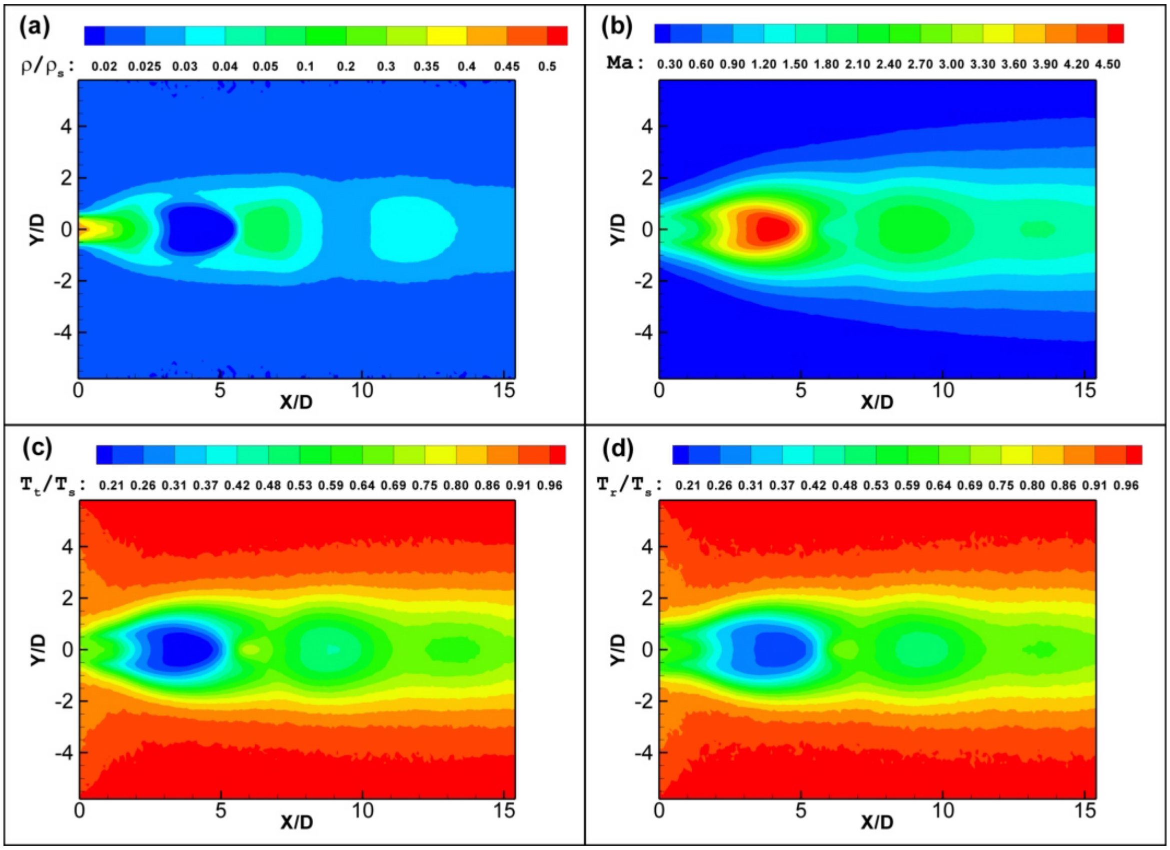

Figure 5.11. The contour maps of single under-expanded jet at the $Z = 0$ symmetry plane for $Kn_s = 0.002$, $P_s/P_b = 50$: (a) normalized density; (b) Mach number; (c) normalized translational temperature; (d) normalized rotational temperature.

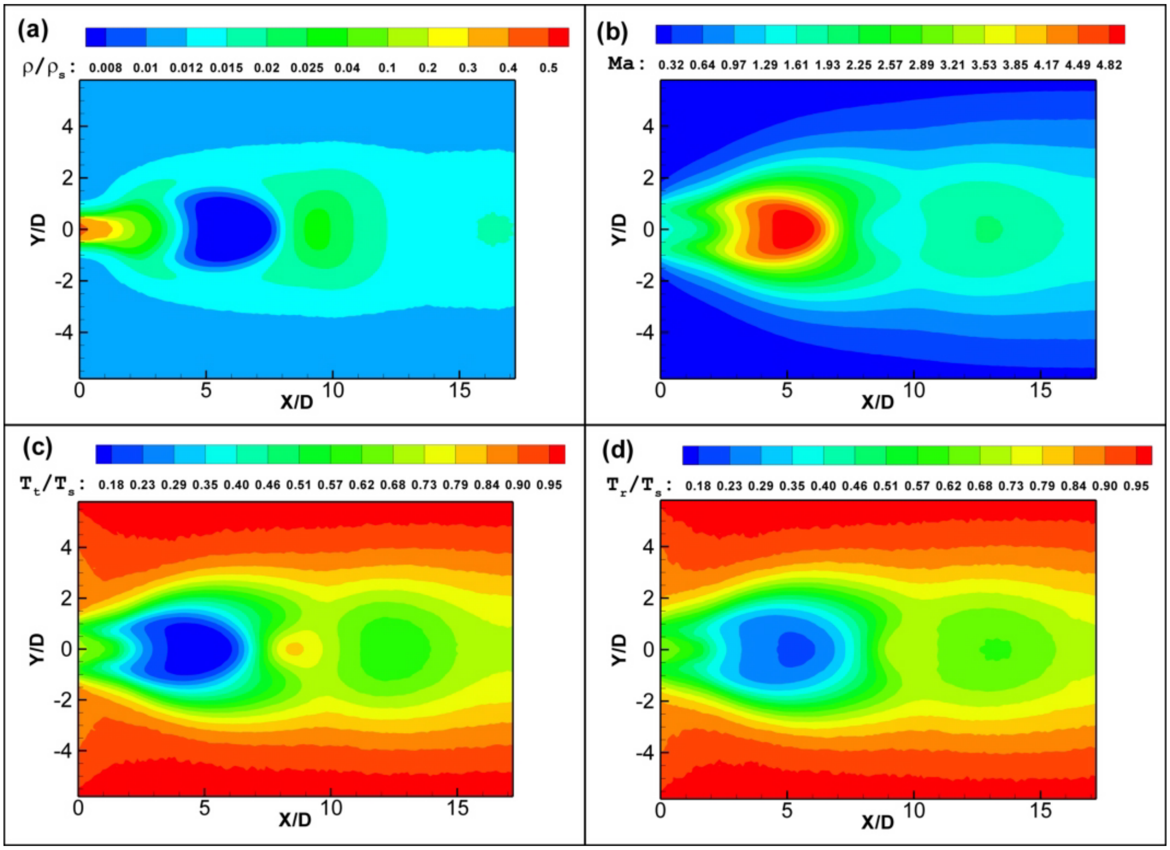

Figure 5.12. The contour maps of single under-expanded jet at the $Z = 0$ symmetry plane for $Kn_s = 0.002$, $P_s/P_b = 100$: (a) normalized density; (b) Mach number; (c) normalized translational temperature; (d) normalized rotational temperature.

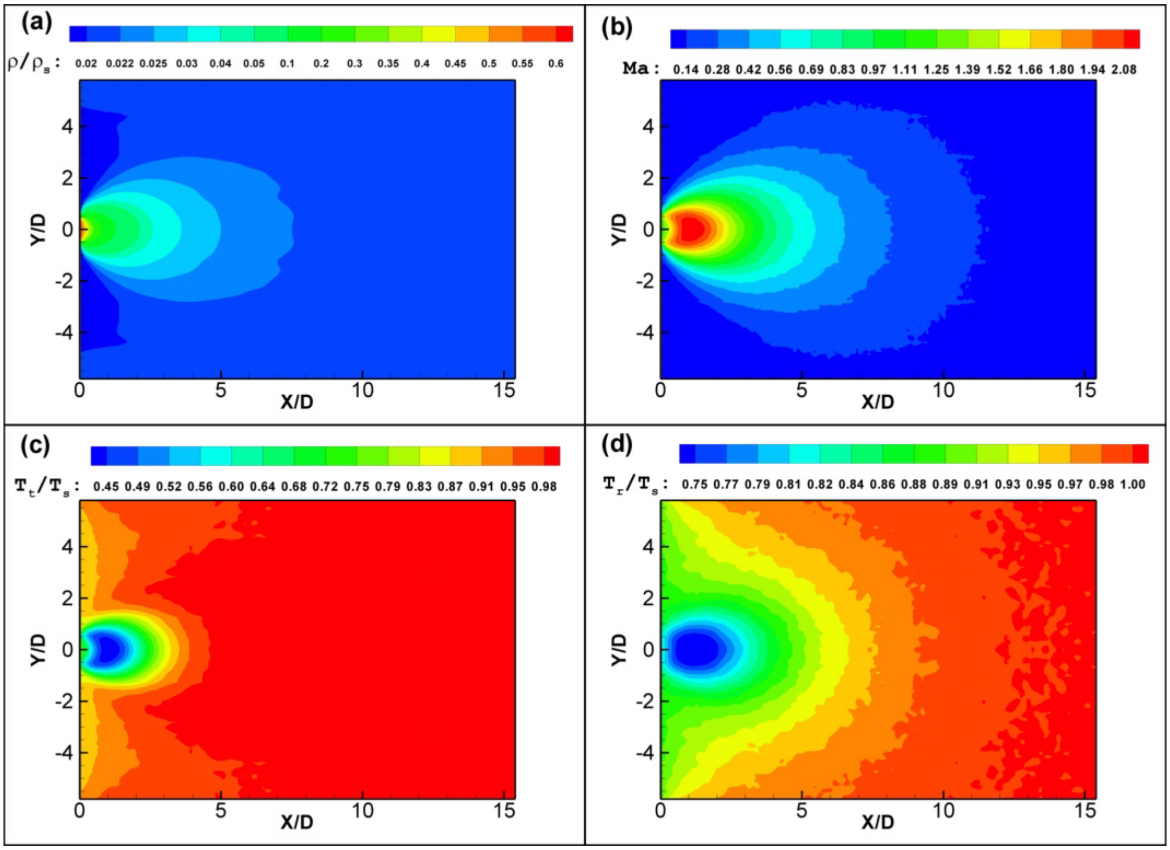

Figure 5.13. The contour maps of single under-expanded jet at the $Z = 0$ symmetry plane for $Kn_s = 0.05$, $P_s/P_b = 50$: (a) normalized density; (b) Mach number; (c) normalized translational temperature; (d) normalized rotational temperature.

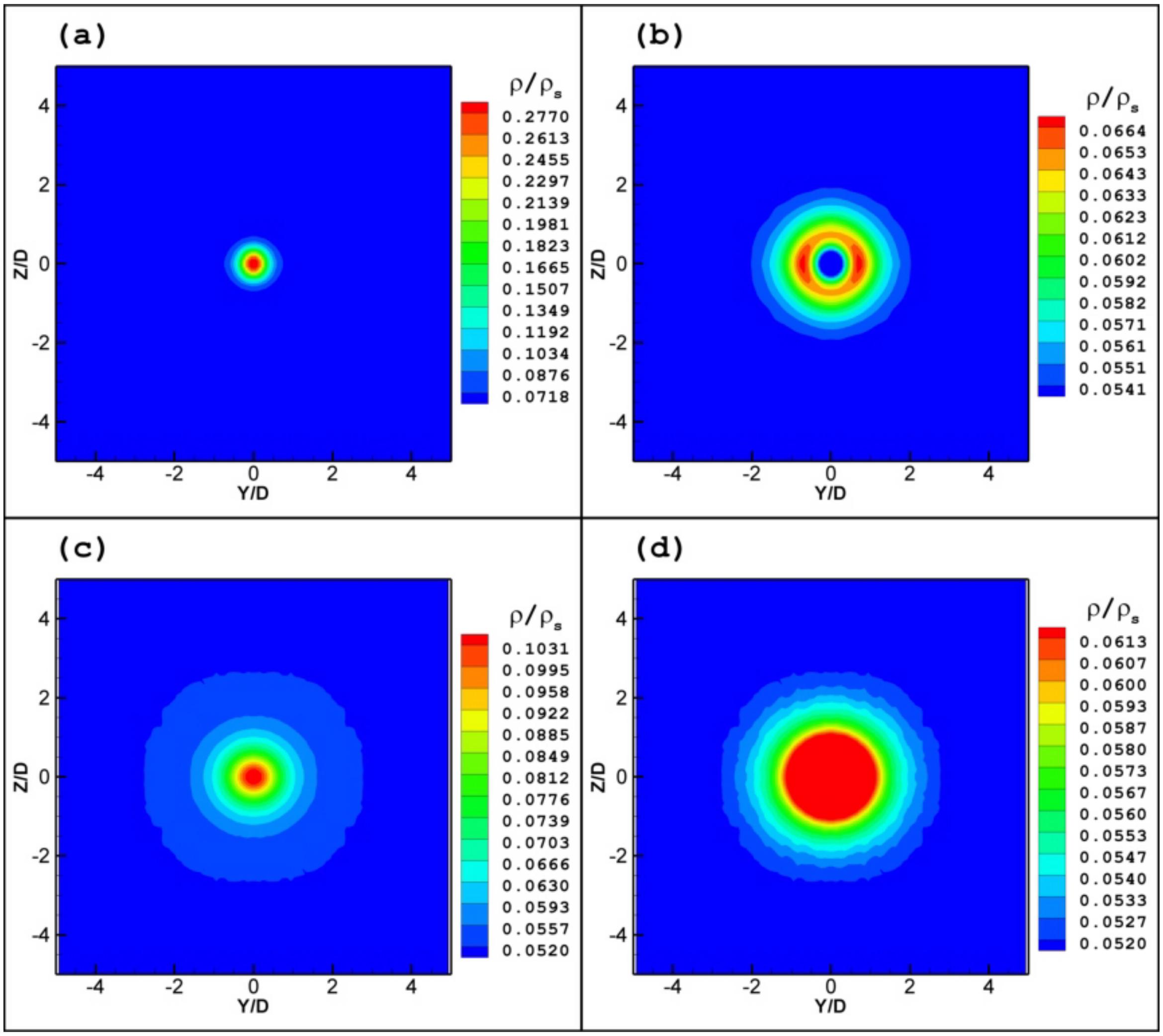

Figure 5.14. The contour maps of normalized density in the $Y - Z$ plane at various X/D locations for flow at $Kn_s = 0.005$, $P_s/P_b = 20$: (a) $X/D = 1.0$; (b) $X/D = 2.0$; (c) $X/D = 6.0$; (d) $X/D = 12.0$

5.2.2 Effects of Kn_s and P_s/P_b

Figures 5.15 through 5.17 are the normalized density, pressure, translational temperature, and rotational temperature distributions along the jet centerline for different pressure ratios when $Kn_s = 0.05$ (Figure 5.15), 0.005 (Figure 5.16), and 0.002 (Figure 5.17). When $Kn_s = 0.05$, the flow is very rarefied and no shock wave is formed. As shown in Figure 5.15(a) and 5.15(b), when P_s/P_b is finite, both the density and pressure distributions are monotonically attenuated to the background values, which are higher for lower P_s/P_b values. The DSMC simulation clearly predicts the correct trend of uniform presence in the plume as P_s/P_b approaches unity. Figure 5.15(c) shows that the translational temperature quickly decays downstream but then gradually increases to the background temperature. Compared with the translational temperature, the rotational temperature distribution (Figure 5.15(d)) asymptotes to background temperature at a significantly slower rate (in X/D). This is consistent with the fact that the relaxation of the rotational mode is slower than the relaxation of the translational mode ($Z_r = \tau_r/\tau > 1$) when the rarefaction effect is strong.

As shown in Figure 5.16, because of the smaller Kn_s value ($Kn_s = 0.005$), the flow could still be in the transitional flow regime when P_s/P_b is small. In Figure 5.16, we can clearly observe the spatial oscillations in the density, pressure, and temperature fields for small values of P_s/P_b. Although it is much dissipative, this is an indication of the waves associated with the "shock-cell" structures.

The interaction between the jet and background gas becomes even stronger when Kn_s is further reduced to 0.002. Increased waviness in the centerline distributions can be observed in Figure 5.17, which means that not only has the "shock-cell" structure been formed, but also that the structure is replicated downstream, which is indeed the expected physics when the jet is expanded in the near continuum regime.

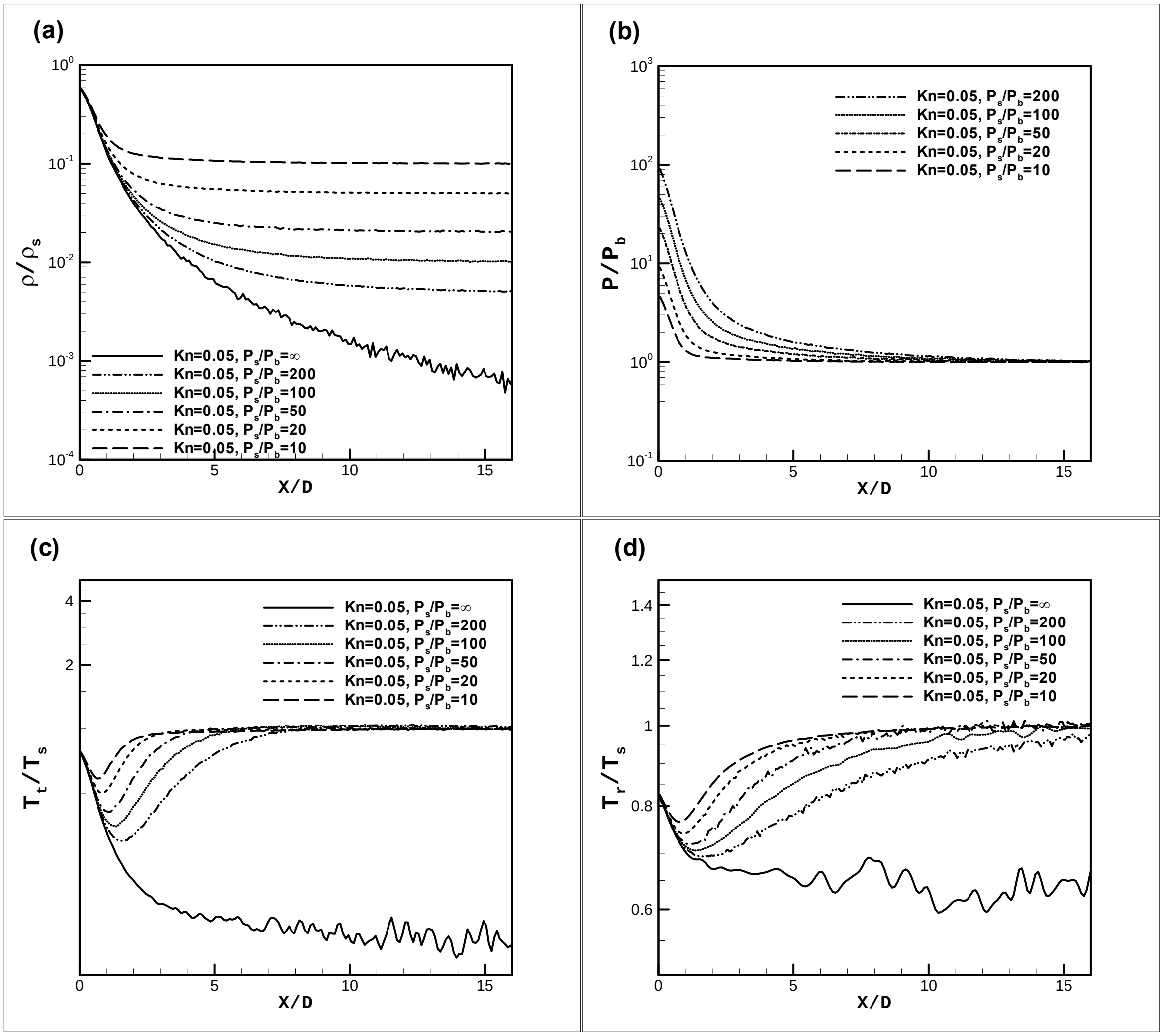

Figure 5.15. Additional centerline results for $Kn_s = 0.05$: (a) ρ/ρ_s; (b) P/P_b; (c) T_t/T_s; (d) T_r/T_s.

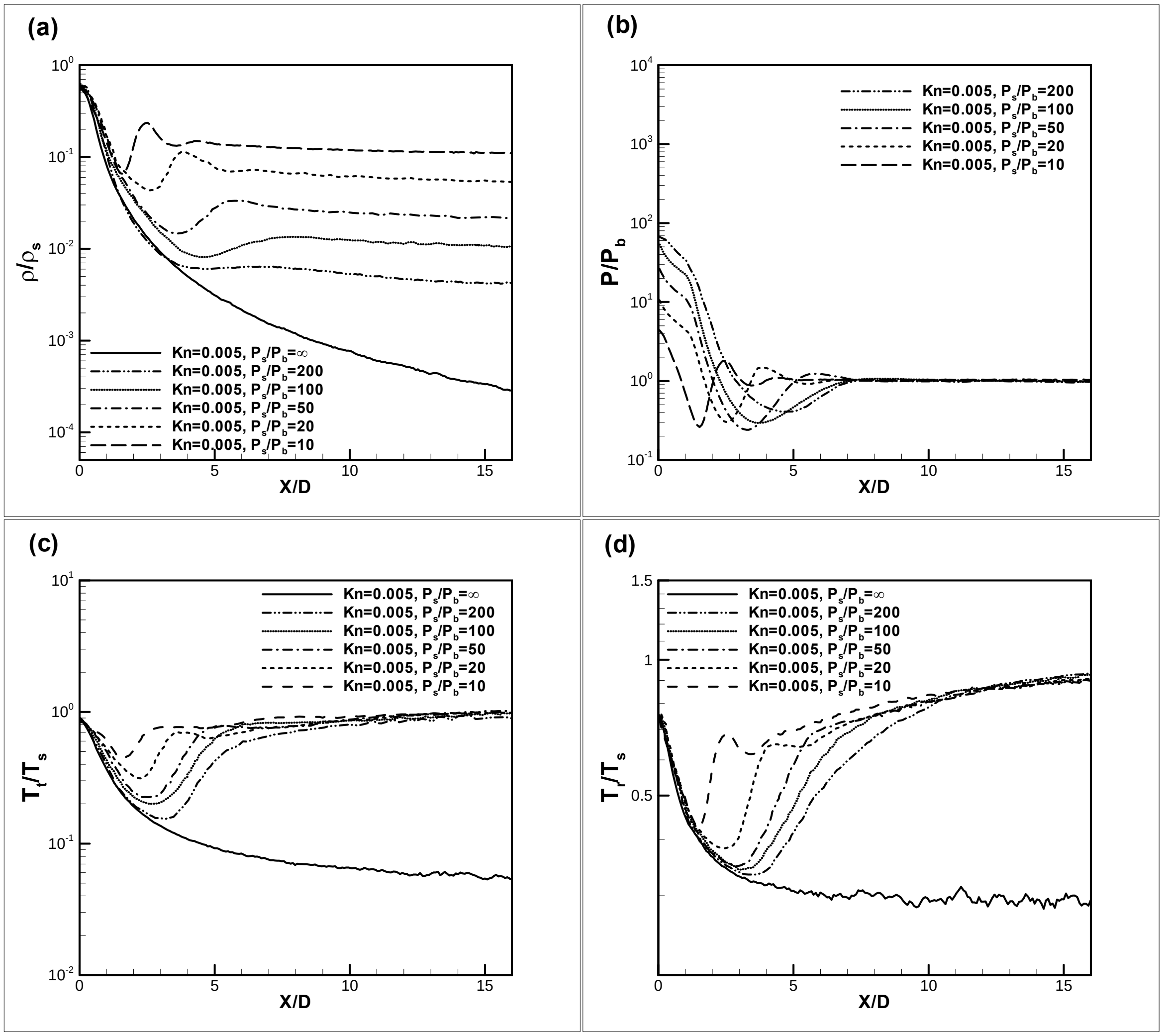

Figure 5.16. Additional centerline results for $Kn_s = 0.005$: (a) ρ/ρ_s; (b) P/P_b; (c) T_t/T_s; (d) T_r/T_s.

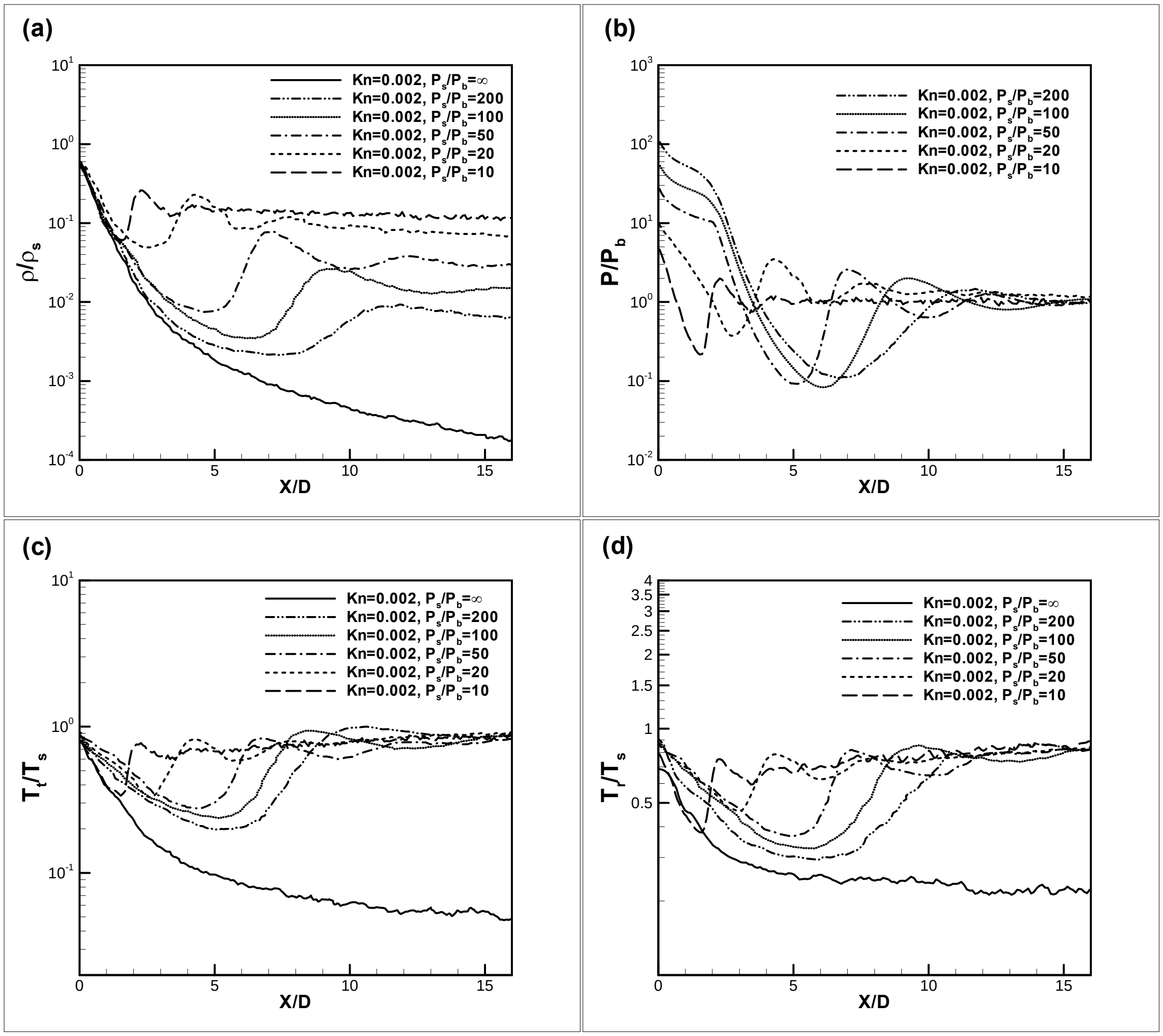

Figure 5.17. Additional centerline results for $Kn_s = 0.002$: (a) ρ/ρ_s; (b) P/P_b; (c) T_t/T_s; (d) T_r/T_s.

5.2.3 Thermal Non-Equilibrium Effects

The nonequilibrium between the translational and rotational temperatures for nitrogen underexpanded jets are shown in Figures 5.18 through 5.22. Figures 5.18 plots the differential behavior of the centerline translational and rotational temperatures at different Kn_s values when $P_s/P_b = 50$. The dependence of translational-rotational non-equilibrium on the Kn_s is shown. At the highest Kn_s value ($Kn_s = 0.05$), the flow is in the rarefied flow regimes, and the deviation between the translational temperature and rotational temperature is large in all of the expansion core, Mach disk (is weak and thickened), and flow downstream of Mach disk (until $X/D = 10$). When Kn_s becomes smaller, while P_s/P_b is unchanged, the gap between the profiles of the two temperatures becomes smaller while the deviation can still be observed until $X/D = 10$. Figure 5.19 plots the same temperature profiles but for different P_s/P_b values when $Kn_s = 0.002$. It can be found that although the location of the Mach disk is changed for different P_s/P_b values, the maximum gap between the two temperatures in expansion core is almost unchanged, while as P_s/P_b is smaller, the non-equilibrium effects can reach further locations of downstream of Mach disk. From these two figures, it can be seen that, in the expansion core, the deviation between the rotational and translational temperatures are more likely decided by the jet's Knudsen number, Kn_s and not affected by P_s/P_b. This is consistent with the fact that the background gases are excluded from the expansion core by the Mach disk and the flow in the expansion core is only affected by Kn_s. However, the rotational-translational nonequilibrium effects in the downstream of Mach disk (including the Mach disk region) are affected by both Kn_s

and P_s/P_b and how far the rotational-translational nonequilibrium effects can reach in the downstream of Mach disk are more sensitive to the pressure ratio P_s/P_b.

Figures 5.20 and 5.21 plot the profiles of translational and rotational temperatures at different X/D locations when $Kn_s = 0.005$, $P_s/P_b = 50$ and $Kn_s = 0.002$, $P_s/P_b = 50$. Four values of $X/D = 1.5$, 3.5, 4.8, and 7.0 are selected to show the translation-rotation nonequilibrium in the transverse direction for flow close to the orifice, flow in the expansion core, flow around the Mach disk, and the flow downstream of Mach disk, respectively. For smaller X/D ($X/D = 1.5$), the existence of barrel shock waves are observed, which results in a large gap between the translational and rotational temperature curves. When X/D becomes large, the effects of barrel shock vanishes due to the fast decay of flow density, and the translation-rotation non-equilibrium effects is significant in the jet boundary only when Kn_s is relatively large ($Kn_s = 0.005$). Figure 5.22 plots the profiles of translational and rotational temperatures at different X/D locations when $Kn_s = 0.005$, $P_s/P_b = 100$. Compare with Figure 5.20, it also can be found that the increase of P_s/P_b value results in a large gap between the translational and rotational temperatures in the jet boundary.

The non-equilibrium between the translational temperature in the jet propagating direction T_x and the translational temperature in the direction normal to the jet propagating direction T_n for an under-expanded jet are also tested. Figure 5.23 shows the T_x and T_n profiles along the jet centerline for an argon under-expanded jet for $Kn_s = 0.05$ and $P_s/P_b = 50$, $Kn_s = 0.005$ and $P_s/P_b = 50$, and $Kn_s = 0.005$ and $P_s/P_b = 100$. Significant deviation between the two temperatures can be found only when Kn_s is large ($Kn_s = 0.05$). When the jet flow is not very rarefied ($Kn_s = 0.005$), T_n only slightly lags to T_x in the expansion core and the flow downstream of Mach disk and these differences are almost negligible.

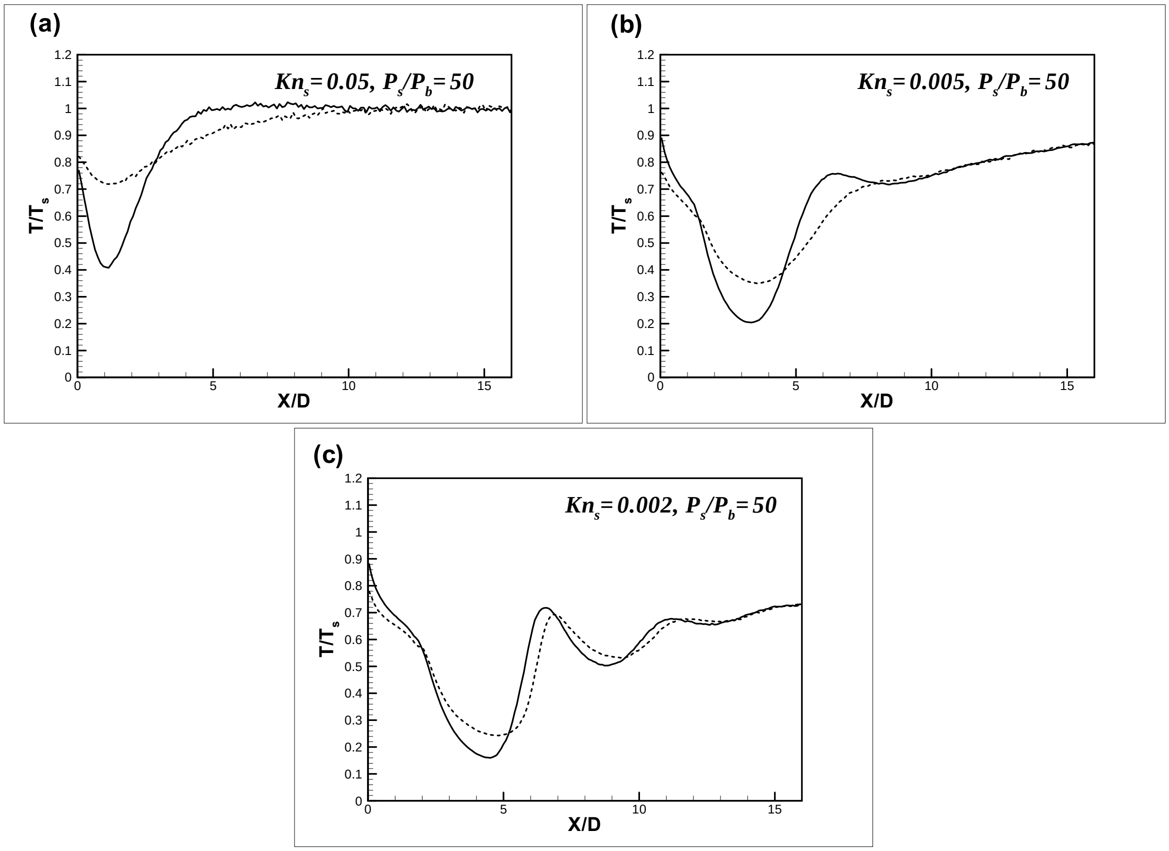

Figure 5.18. Differential behavior of translational (lines) and rotational (dots) temperatures as a function of Kn_s for $P_s/P_b = 50$: (a) $Kn_s = 0.05$; (b) $Kn_s = 0.005$; (c) $Kn_s = 0.002$.

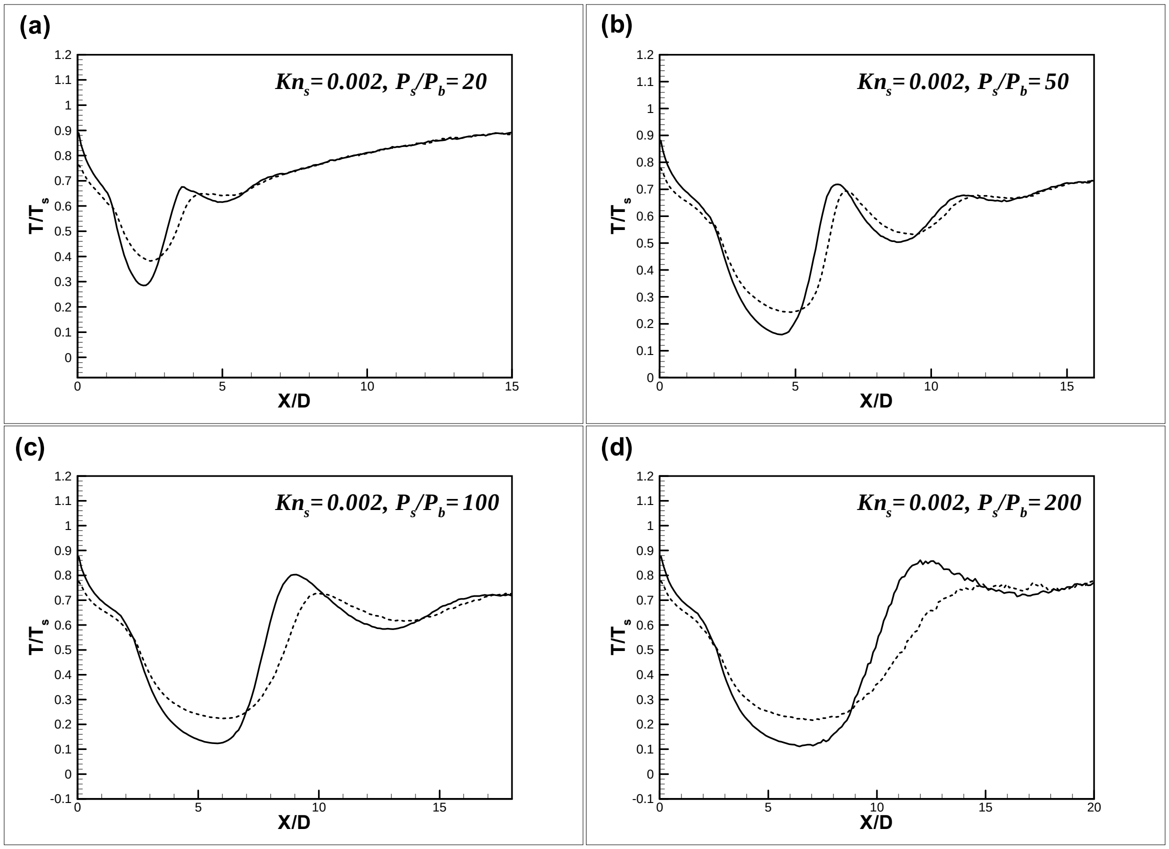

Figure 5.19. Differential behavior of translational (lines) and rotational (dots) temperatures as a function of P_s/P_b for $Kn_s = 0.002$: (a) $P_s/P_b = 20$; (b) $P_s/P_b = 50$; (c) $P_s/P_b = 100$; (d) $P_s/P_b = 200$.

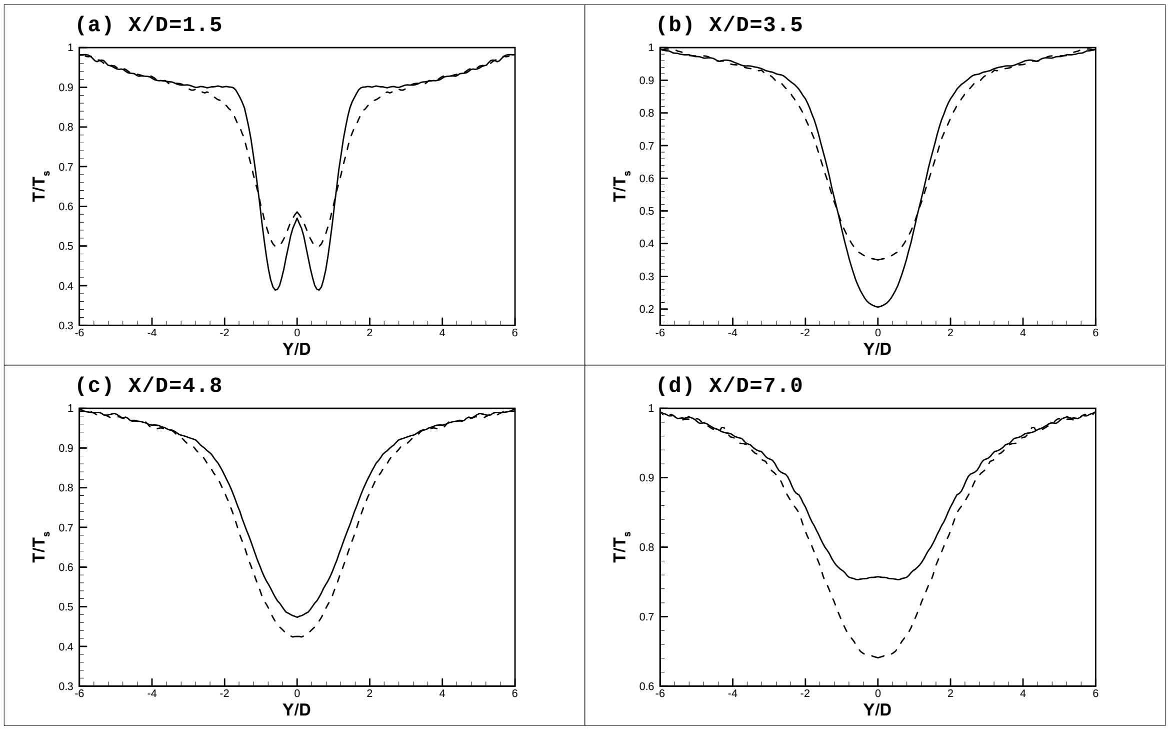

Figure 5.20. The profiles of translational (lines) and rotational (dots) temperatures at different X/D locations: (a) $X/D = 1.5$; (b) $X/D = 3.5$; (c) $X/D = 4.8$; (d) $X/D = 7.0$ when $Kn_s = 0.005$, $P_s/P_b = 50$.

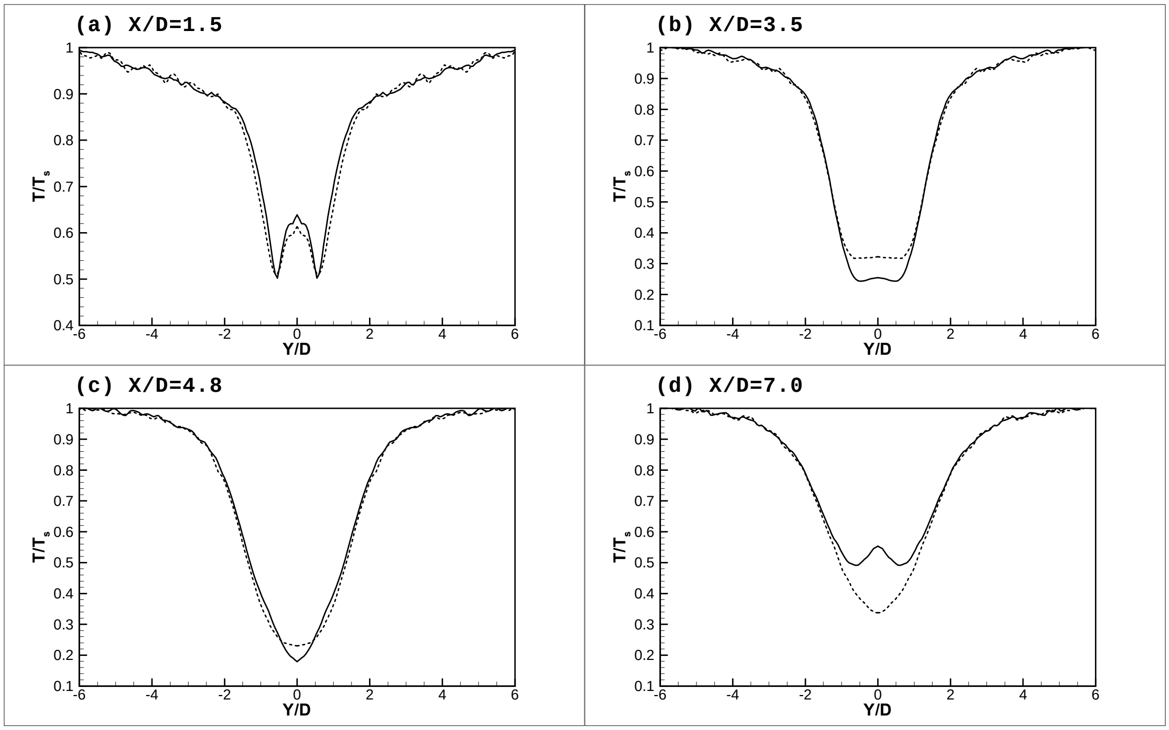

Figure 5.21. The transverse profiles of translational (lines) and rotational (dots) temperatures at different X/D locations: (a) $X/D = 1.5$; (b) $X/D = 3.5$; (c) $X/D = 4.8$; (d) $X/D = 7.0$ when $Kn_s = 0.002$, $P_s/P_b = 50$.

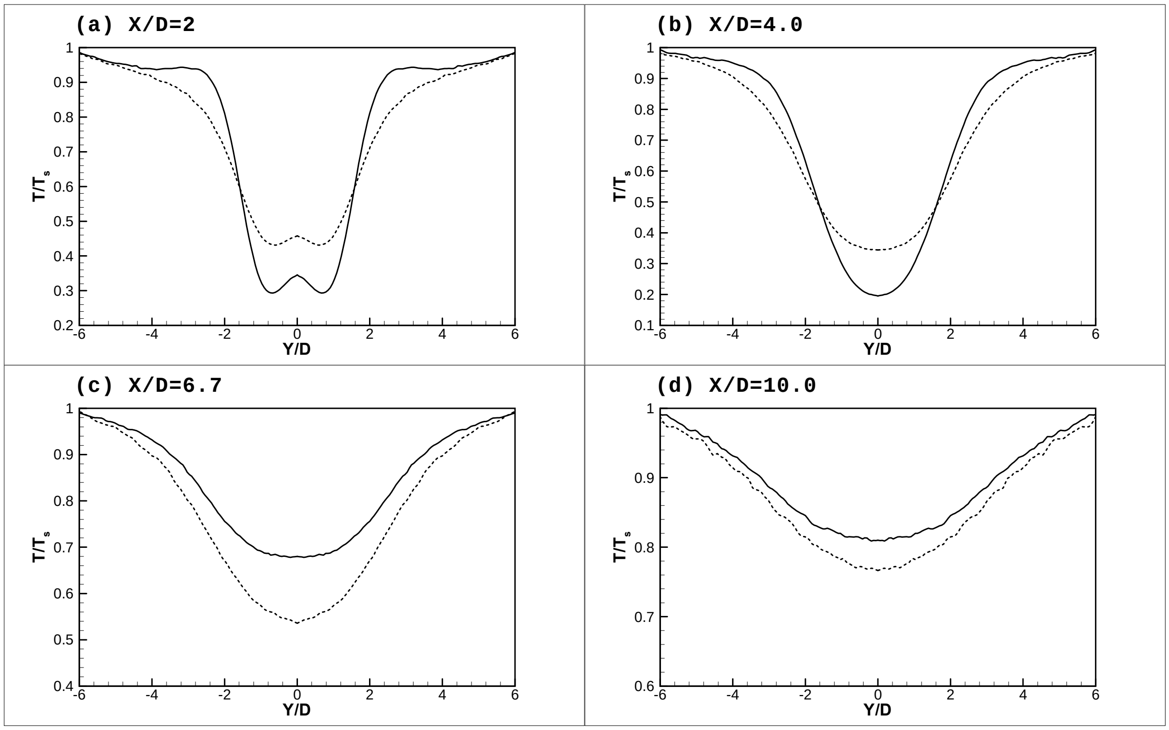

Figure 5.22. The transverse profiles of translational (lines) and rotational (dots) temperatures at different X/D locations: (a) $X/D = 1.5$; (b) $X/D = 3.5$; (c) $X/D = 4.8$; (d) $X/D = 7.0$ when $Kn_s = 0.005$, $P_s/P_b = 100$.

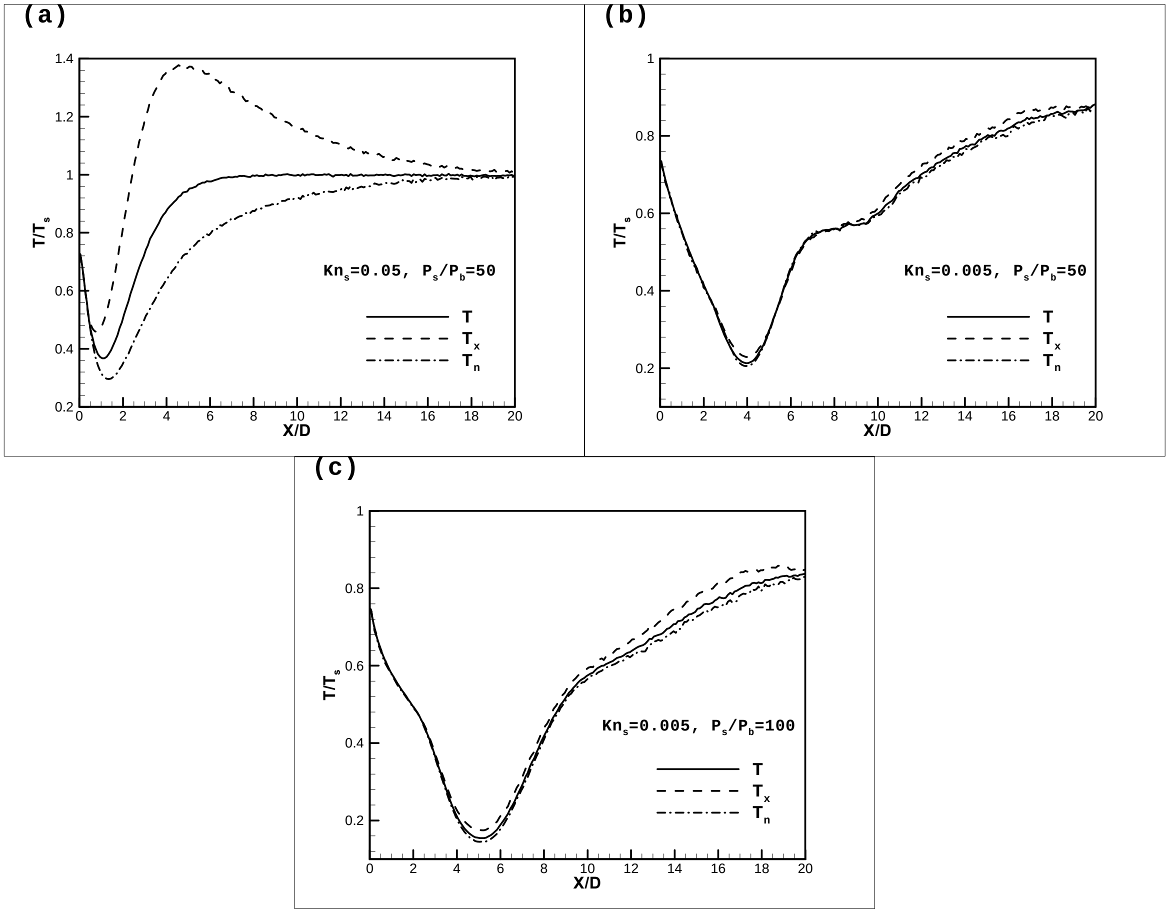

Figure 5.23. Temperature distribution along the jet centerline in an argon under-expanded jet: (a) $Kn_s = 0.05$ and $P_s/P_b = 50$; (b) $Kn_s = 0.005$ and $P_s/P_b = 50$; (c) $Kn_s = 0.005$ and $P_s/P_b = 100$.

5.2.4 Location of the Mach Disk

A simple theoretical model is also developed to support the experimental correlation in Equation (5.15) describing the location of the Mach disk. The flow in the vicinity of the nozzle exit and in the isentropic core is in continuum, with the consequent assumption of isentropic conditions. By using the Rankine-Hugoniot relations, the density just behind the Mach disk can be estimated as

$$n'_j \approx n_s \frac{\gamma+1}{\gamma-1} \Phi^{-\frac{1}{\gamma-1}} \left(\frac{X_M}{D} \right)^{-2} , \tag{5.25}$$

where Φ has been defined previously (Equation (5.8)). The mean free path length of the jet molecules in the background gas λ'_{jb} is [33]

$$\lambda'_{jb} = \frac{c'_b}{n'_j \sigma_{jb} u_{r,jb}} = \frac{\frac{2}{\sqrt{\pi}} \sqrt{2RT_s}}{C\left(\gamma\right) n_s \left(D/X\right)^2 \cdot \pi d^2 \cdot \left(\frac{2\gamma R T_s}{\gamma-1} \right)^{1/2}} = \frac{2k\sqrt{1-\frac{1}{\gamma}}}{C\left(\gamma\right) \pi^{3/2} d^2} \cdot \frac{T_s}{P_s} \cdot \left(\frac{X_M}{D} \right)^2 , \tag{5.26}$$

where $c'_b = \frac{2}{\sqrt{\pi}}\sqrt{2RT_s}$ is the mean thermal velocity of the background molecules, $\sigma_{jb} = \pi d^2$ is the collision cross-section area between the jet and background molecules, and $u_{r,jb}$ is the relative velocity between the jet molecules and background molecules. Here, we still assume the jet molecule has reached its adiabatic speed limit ($u_{r,jb} = u_{\max} = \left(\frac{2\gamma R T_s}{\gamma-1} \right)^{1/2}$). The constant $C\left(\gamma\right)$ is defined as

$$C\left(\gamma\right) = \left(\frac{\gamma+1}{\gamma-1} \right) \Phi^{-\frac{1}{\gamma-1}} = \begin{cases} 0.623 & \text{for} \quad \gamma = 1.667 \\ 0.528 & \text{for} \quad \gamma = 1.400 \\ 0.488 & \text{for} \quad \gamma = 1.286 \end{cases} . \tag{5.27}$$

The background gas cannot affect the isentropic core, and in the zone downstream of the Mach disk, the jet flow can mix with the background gas. Therefore, the mean free path length of the jet molecules moving into the background molecules just behind the Mach disk should be comparable with the mean free path length of the background molecules ($\lambda'_{jb} \sim \lambda_b$), where λ_b can be calculated as [33]

$$\lambda_b = \frac{k}{\sqrt{2}\pi d^2} \cdot \frac{T_s}{P_b} \,. \tag{5.28}$$

Therefore

$$\frac{k}{\sqrt{2}\pi d^2} \cdot \frac{T_s}{P_b} \sim \frac{2k\sqrt{1-1/\gamma}}{C\left(\gamma\right)\pi^{3/2} d^2} \cdot \frac{T_s}{P_s} \cdot \left(\frac{X_M}{D}\right)^2 \qquad , \tag{5.29}$$

or

$$\frac{X_M}{D} \propto f\left(\gamma\right)\left(\frac{P_s}{P_b}\right)^{1/2} \quad , \tag{5.30}$$

where

$$f\left(\gamma\right) = \left(\frac{C\left(\gamma\right)\sqrt{\pi}}{2^{3/2}\sqrt{1-1/\gamma}}\right)^{0.5} = \begin{cases} 0.786 & \text{for} \quad \gamma = 1.667 \\ 0.787 & \text{for} \quad \gamma = 1.400 \\ 0.805 & \text{for} \quad \gamma = 1.286 \end{cases} \,. \tag{5.31}$$

Equations. (5.30) and (5.31) show that the location of the Mach disk is proportional to the square root of P_s/P_b and $f\left(\gamma\right)$ is fairly independent of γ. This simple model provides an explanation for the experimental results pertaining to the location of the Mach disk.

Figure 5.24 shows the location and diameter of the Mach disk predicted by the DSMC program and shows good agreement with the empirical relations given by Equations (5.15) and (5.16). In the current study, the location and size of the Mach disk is defined by the position where the local Mach number has the maximum slope. The error bars are shown in the figure.

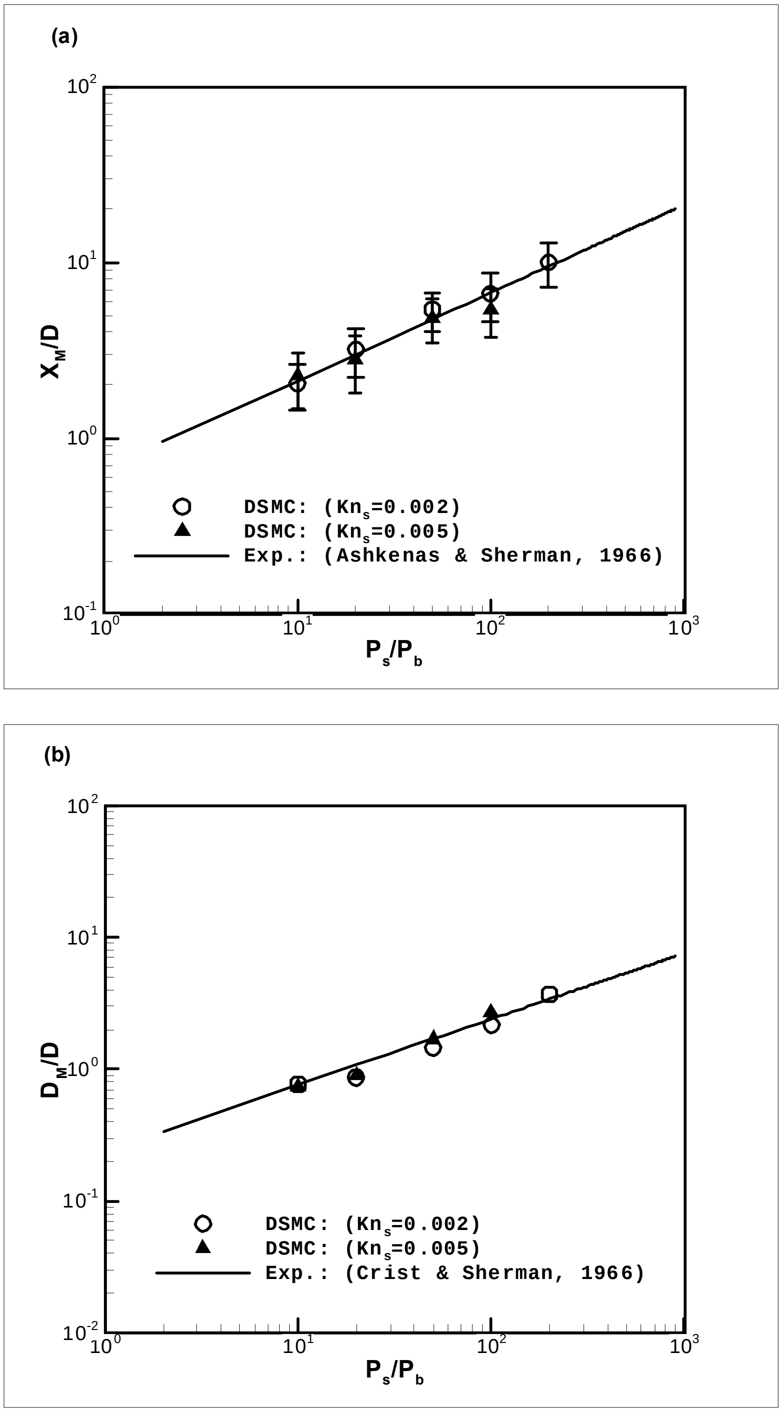

Figure 5.24. Location (a) and diameter (b) of the Mach disk as a function of pressure ratio.

In summary, a numerical study of a single under-expanded jet under sonic conditions using the DSMC calculations is reported for flow in both rarefied and near continuum regimes, within a stagnation Knudsen number, Kn_s, range of $0.002 \leq Kn_s \leq 0.05$ and the ratio of the stagnation-to-background pressure, P_s/P_b, between 10 and values that approach infinity. The downstream boundary conditions have been successfully implemented by using the "particle conservation" method.

The thermal nonequilibrium effects for rarefied under-expanded jets were studied. For the jet expanding into vacuum, an approximation expression was derived to predict the rotational temperature distribution along the jet centerline. For nitrogen under-expanded jets, the rotational-translational thermal nonequilibrium effects are found to be significant for all of the flows in the expansion core, around the Mach disk, and in downstream of Mach disk even when Kn_s and P_s/P_b is relatively small. In the expansion core, the deviation between the rotational and translational temperatures are more likely determined by Kn_s and not affected by P_s/P_b. The rotational-translational nonequilibrium effects in the downstream of Mach disk (including the Mach disk region) are affected by both Kn_s and P_s/P_b. However, how far the rotational-translational nonequilibrium effects can reach in the downstream of Mach disk is more sensitive the pressure ratio P_s/P_b.

The location of the Mach disk was also studied by the DSMC results and by a simple theoretical analysis. The predicted Mach disk locations and diameters compare well with the empirical correlations.

Chapter 6
Dual Interacting Jets

The physics of dual, interacting jets were investigated with the DSMC procedure after establishing the accuracy of the numerical approach for the current type of problems. The physical problem of interest is as in Figure 1.1, with the computational domain in Figure 6.1. With the assumption of symmetry, only a quarter of the three-dimensional model is simulated. The model is similar to that for the single under-expanded jet, except that the orifice is now located at $(0, 0, L/2)$, where L is the separation between the two orifices. The settings of the boundary conditions are also same with those used for single under-expanded jets. The values of the stagnation Knudsen number, Kn_s, chosen for the study are 0.02, 0.005, and 0.002, and the separation between the orifices are within $1.0 \leq L/D \leq 8.0$. The stagnation-to-background pressure ratios $P_s/P_b = 50$, 100, 200, and values that approach infinity are used. The domain is chosen to be sufficiently large so that the influence of the interacting jets does not reach the downstream boundary. The stagnation pressure and temperature of the jet flow are $P_s = 870$ Pa and $T_s = 285$ K, respectively. The simulation cases are given in Table 6.1.

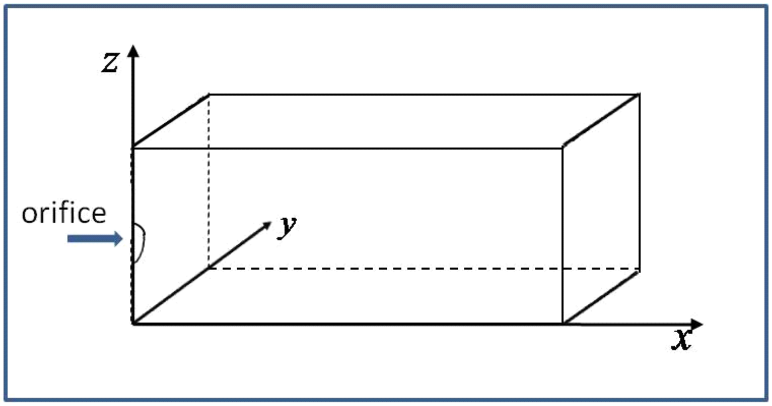

Figure 6.1. Computational model for the DSMC calculation of interacting jets

Table 6.1. Case studies for the DSMC simulation of interacting jets

Case	Kn_s	P_s/P_b	L/D	**Orifice Diameter** (m)	ξ $(\frac{dynes}{cm \cdot K})$	$Kn_{p,\min}$	**Size of Domain**	**No. of Particles**
1	0.002	220	1.0	3.0×10^{-3}	0.6024	0.0478	$35D \times 7D \times 8D$	27,962,359
2	0.002	220	2.0	3.0×10^{-3}	0.6024	0.0956	$35D \times 7D \times 8D$	28,315,263
3	0.002	220	3.0	3.0×10^{-3}	0.6024	0.1434	$35D \times 6D \times 8D$	25,651,298
4	0.002	220	6.0	3.0×10^{-3}	0.6024	0.2867	$30D \times 6D \times 9D$	20,395,871
5	0.002	220	8.0	3.0×10^{-3}	0.6024	0.3823	$30D \times 5D \times 10D$	21,745,141
6	0.002	∞	3.0	3.0×10^{-3}	0.6024	0.1434	$35D \times 6D \times 8D$	15,363,830
7	0.005	∞	3.0	3.0×10^{-3}	0.0000	0.3584	$35D \times 6D \times 8D$	12,104,632
8	0.005	200	3.0	1.18908×10^{-3}	0.2527	0.3584	$35D \times 6D \times 8D$	20,194,251
9	0.005	100	3.0	1.18908×10^{-3}	0.3574	0.3584	$30D \times 6D \times 8D$	22,325,751
10	0.005	50	3.0	1.18908×10^{-3}	0.5055	0.3584	$30D \times 6D \times 6D$	21,146,486
11	0.02	∞	3.0	1.18908×10^{-3}	0.0000	1.4336	$30D \times 6D \times 8D$	6,372,875
12	0.02	200	3.0	3.0×10^{-4}	0.0632	1.4336	$25D \times 6D \times 8D$	10,325,459
13	0.02	100	3.0	3.0×10^{-4}	0.0894	1.4336	$25D \times 6D \times 8D$	10,698,869
14	0.02	50	3.0	3.0×10^{-4}	0.1264	1.4336	$25D \times 6D \times 8D$	12,326,652

6.1 Interacting Jets Expanding Into Vacuum

For the two identical sonic interacting jets expanding into vacuum, only the interactions between the molecules of the two jets need to be considered. When the interaction is strong, oblique shock waves are formed and the interaction region looks like another jet, which is called "secondary jet". This flow structure is shown in Figure 1.1(a).

6.1.1 Rarefaction Parameter

The interaction between the molecules of the two jets was first studied by Dankert and Koppenwallner [8, 15]. They introduced a parameter Kn_p, which is called Penetration Knudsen number, to describe the interaction:

$$Kn_p \equiv \frac{\lambda_p}{l_{ref}} \quad , \tag{6.1}$$

where λ_p is the penetration mean free path of one plume molecules moving through another plume flow field and l_{ref} represents the characteristic length of the flow, which is chosen as the distance from the symmetry plane to the centerline of the plume, as shown in Figure 6.2. It can be shown that Kn_p is a function of the jet's stagnation Knudsen number Kn_s, the orifice separation distance L/D, and the interaction angle θ, which can be expressed as

$$Kn_p(\theta) = \frac{2\sqrt{2}}{\sqrt{\pi}}\sqrt{1+\frac{1}{\gamma}}\cdot\frac{Kn_s}{A}\cdot\frac{L}{D}\cdot\frac{1}{f(\theta)\sin^2\theta} = \frac{2\sqrt{2}}{\sqrt{\pi}}\sqrt{1+\frac{1}{\gamma}}\cdot\frac{Kn_s}{A}\cdot\frac{L}{D}\cdot g\left(\theta\right) \quad , \tag{6.2}$$

where

$$g(\theta) = \left[\cos^2\left(\frac{\pi}{2} \cdot \frac{\theta}{\theta_{\max}}\right)\sin^2\theta\right]^{-1}$$

and A and θ_{max} have been defined previously (Equation (5.2)). The interaction between the two jets can be characterized by $Kn_{p,min}$, which is the value of Kn_p when $g(\theta)$ attains its lowest value, which occurs when $\theta \approx 39°$.

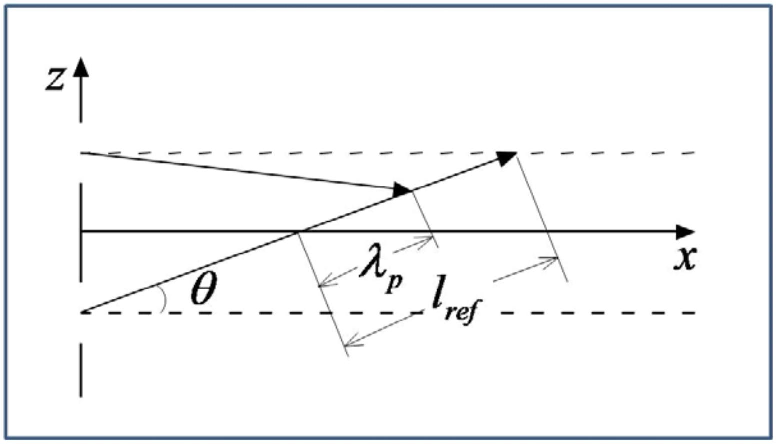

Figure 6.2. Definition of Kn_p for dual interacting jets, showing the penetration mean free path λ_p, the reference length l_{ref}, and the interaction angle θ.

Using $Kn_{p,\min}$ as a parameter, plume-plume interaction can be classified as follows (Figure 6.3) [8]:

(1) When $Kn_{p,\min} \gg 1$, the interaction is in the free molecular regime. In this case, the collision between the molecules of the two jets can be neglected, so that no shock wave is created in the flow field. The flow field can be considered as the summation of the movements of the two classes of molecules – the molecules from the two jets. In particular,

for the case of $Kn_p \to \infty$, the flow is totally collisionless and the number density profile of the flow field can be accurately evaluated as the sum of the number density of every plume such that

$$n_{total} = n_{jet,1} + n_{jet,2} \ , \tag{6.3}$$

where n_{total}, $n_{jet,1}$ and $n_{jet,2}$ are the total number density, number density of jet 1 and number density of jet 2, respectively

(2) When $Kn_{p,\min} \sim 1$, the interaction is in the near free molecular regime. Here, few collisions will occur, and the shock waves can still be neglected. The molecules emanating from every jet have a finite penetrating mean free path λ_p as compared to the collisionless flow. Different from the flows in the free molecular regime, the molecules from one jet cannot completely penetrate the flow field of the other jet and are blocked by the molecules from the other jet, thereby compressing the molecules in a finite region. As a result, the number density in the interaction region is larger as Kn_p becomes smaller.

(3) When $Kn_{p,\min} < 1$, the interaction is in the near continuum regime. In this regime, the collision effects between the two jets are significant. With smaller Knudsen numbers, the flow will gradually acquire the Rankine-Hugoniot characteristics. The interaction of the two jets located with a distance L from each other is mathematically equivalent to the interaction of one jet with a specular plane located at a distance $L/2$ from the source orifice. As in the case of an interaction with a plane, an oblique shock wave will be formed near the symmetric plane of the two jets. The region surrounded by the oblique shock waves

is called the interaction region. Due to rarefaction effects, the oblique shock wave is thick and weak in this regime.

(4) When $Kn_{p,\min} \ll 1$, the interaction is in the continuum regime and a strong oblique wave front is formed. The stream velocity behind the shock front is completely parallel to the symmetry plane. The penetration effects between the two plumes can be neglected in the limiting case of $Kn_{p,\min} \to 0$.

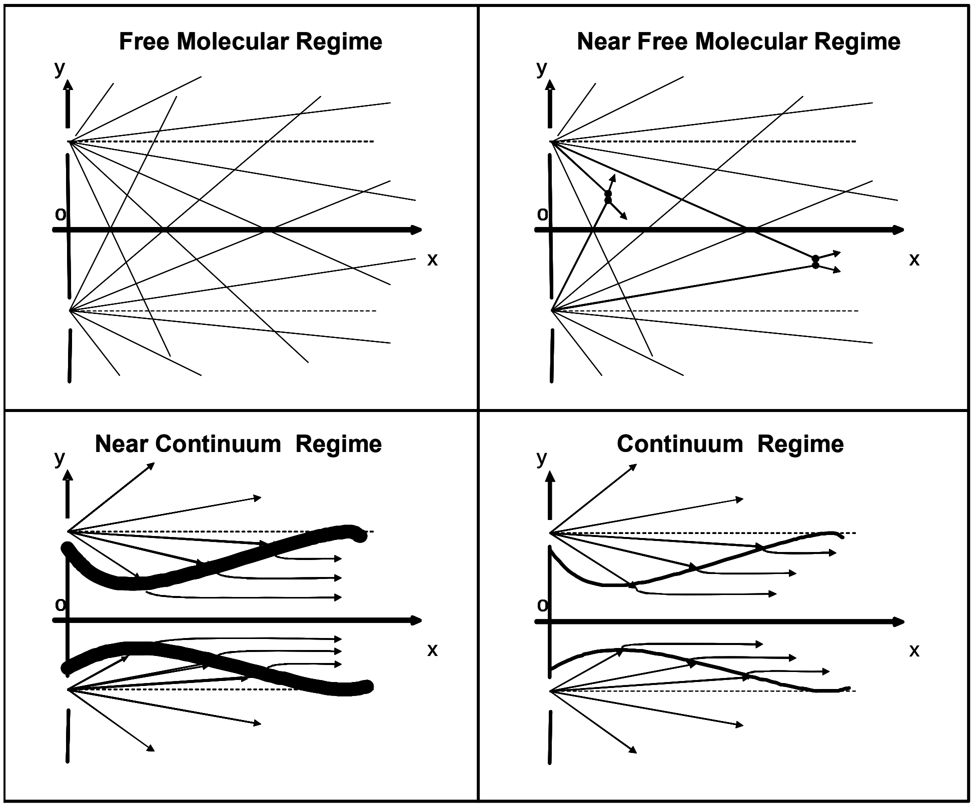

Figure 6.3. The possible plume interacting regimes for interacting jets expanding into vacuum.

Figures 6.4 and 6.5 show the contour maps of the normalized density, translational temperature and rotational temperature on the $y = 0$ and $z = 0$ symmetry planes for $Kn_s = 0.002$, $L/D = 3$, and $P_s/P_b \rightarrow \infty$. In this case, $Kn_{p,\min} = 0.1434$ and flow is in the near continuum regime. The interaction between the two jets is strong and we can clearly observe an interaction region that is formed, especially in the temperature contours. Since the collisions between the molecules of the two jets nullify the $z-$velocity component of the molecules and the kinetic energy is converted into thermal energy, it is clear that the secondary jet has higher temperature than the primary jets. Figure 6.5 shows that the secondary jet expands at a faster rate in the $y-$direction. Because of low density in the secondary jet, the secondary jet is very rarefied and it is expected to observe significant differences between the translational and rotational temperature contours in the secondary jet. We also can observe that the maximum points for the density and temperature profiles on the x-axis are not at the same position. In this case, the density has a maximum value at $x/D \approx 3$, while the translational and rotational temperatures have a maximum value at $x/D \approx 1$.

Figures 6.6 shows the normalized density, translational temperature and rotational temperature contours on the $y = 0$ symmetry plane for $Kn_s = 0.02$, $L/D = 3$, and $P_s/P_b \rightarrow \infty$. Compared with Figure 14, the flow is more rarefied due to the larger Kn_s value ($Kn_{p,\min} = 1.4336$). In this case, the secondary jet is not evident in the density contour, but is more pronounced in temperature contours. Also, larger deviations between the translational and rotational temperatures can be observed.

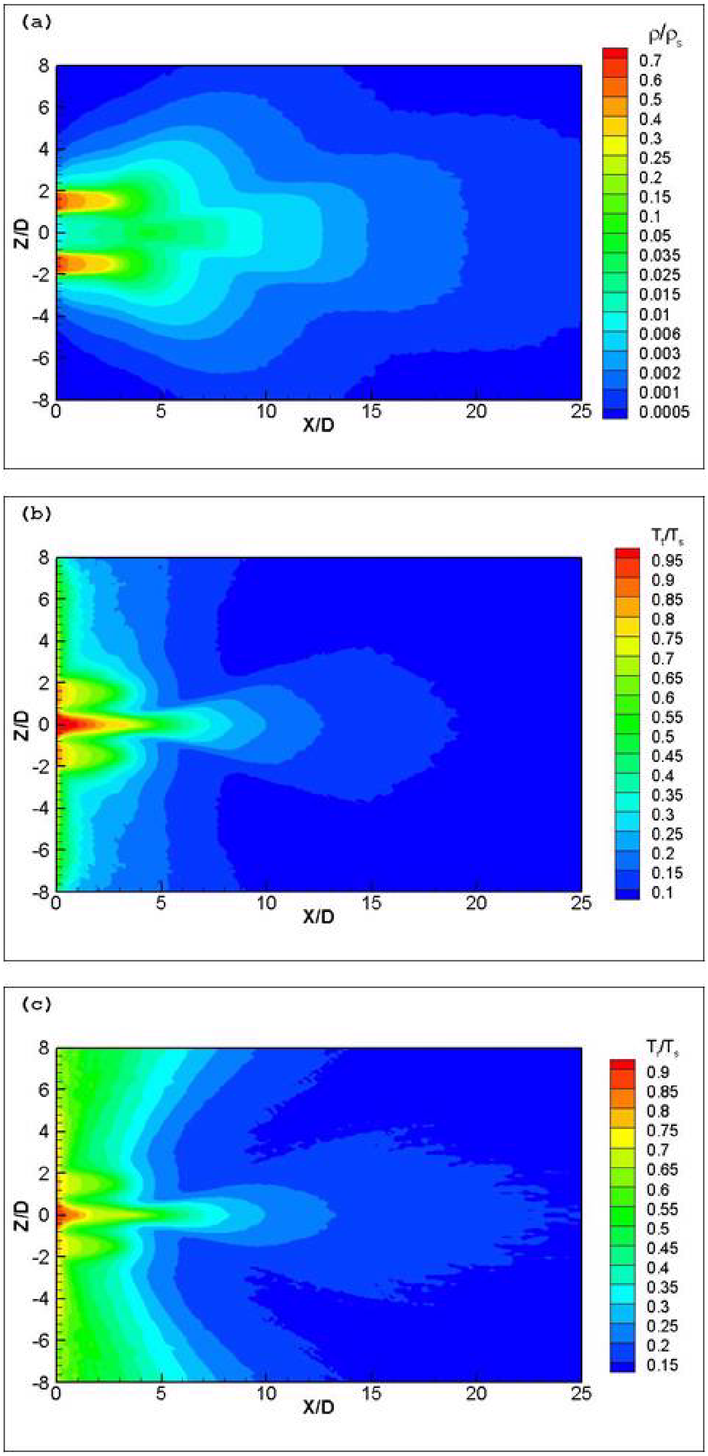

Figure 6.4. Density (a), translational temperature (b), and rotational temperature (c) contours on the $y = 0$ symmetry plane for $Kn_s = 0.002$, $L/D = 3$, and $P_s/P_b \rightarrow \infty$.

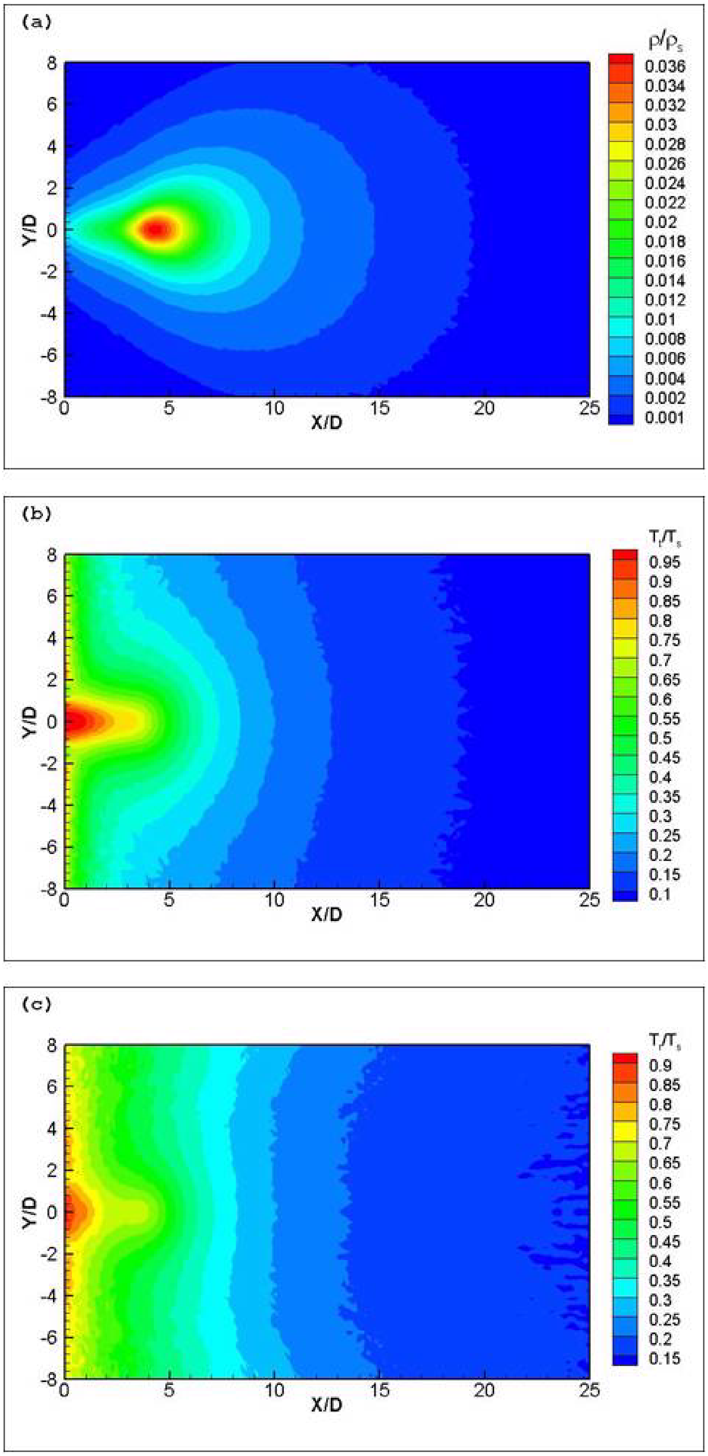

Figure 6.5. Density (a), translational temperature (b), and rotational temperature (c) contours on the $z = 0$ symmetry plane for $Kn_s = 0.002$, $L/D = 3$, and $P_s/P_b \to \infty$.

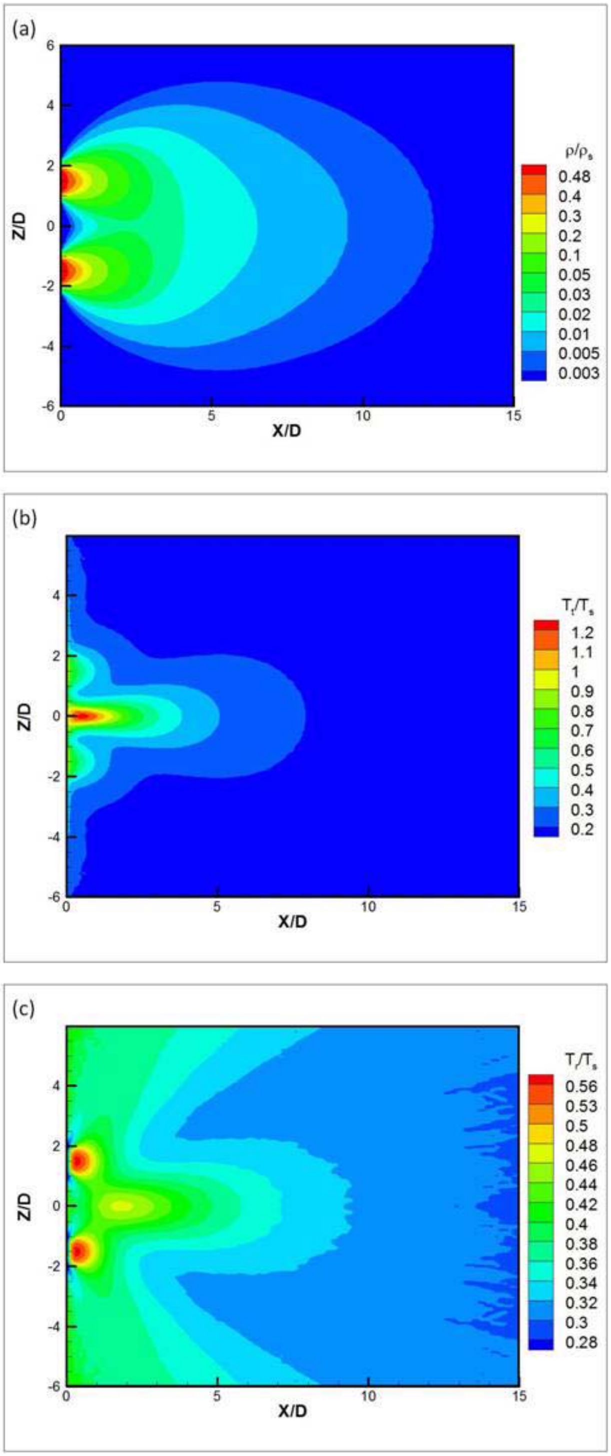

Figure 6.6. Density (a), translational temperature (b), and rotational temperature (c) contours on the $y = 0$ symmetry plane for $Kn_s = 0.02$, $L/D = 3$, and $P_s/P_b \to \infty$.

6.1.2 The Effects of Kn_s

To show the effect of Kn_s, Figure 6.7 shows the density profiles along the $(x, 0, 0)$ symmetry axis for different values of Kn_s when $L/D = 3.0$. It clearly shows that when Kn_s becomes smaller, the interaction between the two plumes becomes more significant, which results in the increase of the density in the interaction region. We can also notice that as Kn_s decreases, the position of the maximum point on the density profile moves toward right. This is due to the fact that, when Kn_s is small, the oblique shock waves are formed and likely to change the direction of the flow streamlines to the x-direction in the secondary jet.

In Figure 6.7, a prediction from the asymptotic model (Equation (5.2)) for the case $Kn_s \to \infty$ is also plotted. When $Kn_s \to \infty$, the flow is in the free molecular regime, as shown in Figure 6.8, the density profile along the $(x, 0, 0)$ axis can be computed by the addition of the density profiles of the two jets:

$$\rho_{total} = \rho_{jet,1} + \rho_{jet,2} = 2\rho_i \ . \tag{6.4}$$

Substituting Equation (5.2) into Equation (6.4), we can obtain the expression for the density profile along the $(x, 0, 0)$ axis as

$$\frac{\rho_t(x/D)}{\rho_s} = 2A\left(\frac{D}{R/2}\right)^2 \cdot f\left(\theta\right) = 2A^*\left(\frac{D}{L}\right)^2 \cdot \sin^2\theta \cdot \cos^2\left(\frac{\pi}{2} \cdot \frac{\theta}{\theta_{\max}}\right) \tag{6.5}$$

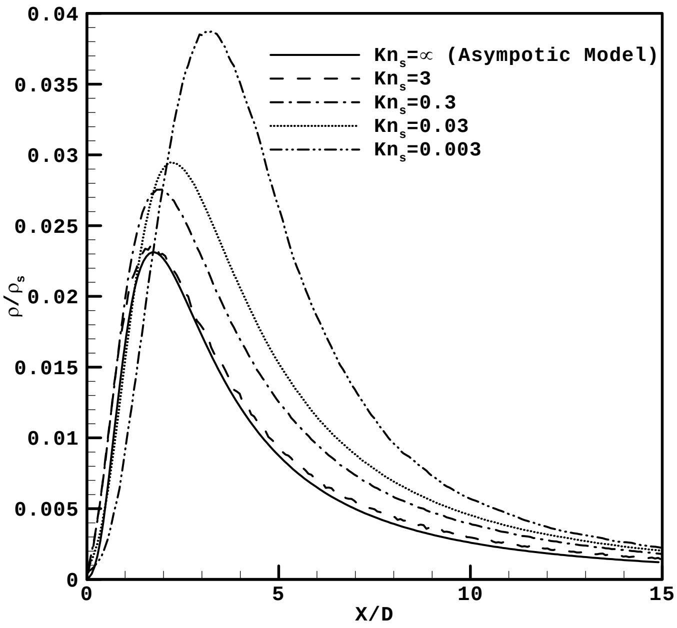

Figure 6.7. Normalized density profile along the $(x, 0, 0)$ axis for different values of Kn_s when $L/D = 3$

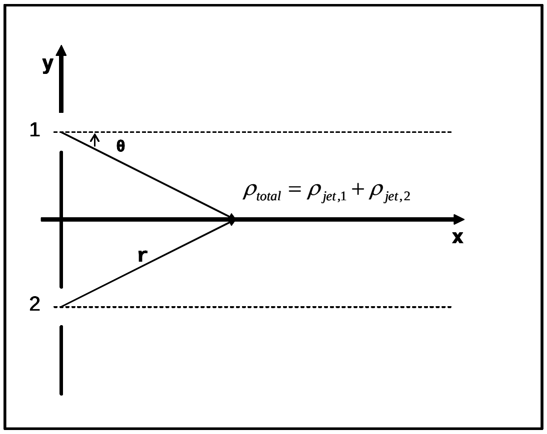

Figure 6.8. Interacting jets for $Kn_s \to \infty$

6.1.3 The Effects of L/D

Figure 6.9 shows the normalized density distributions along $(x, 0, 0)$ symmetry axis for different values of L/D when $Kn_s = 0.003$. As expected, when the value of L/D is smaller, the interaction between the two plumes is stronger and higher density field in the secondary jet can be observed. The effects of L/D can also be estimated from Equation (6.5). It can be seen that the density ρ is proportional to $\frac{1}{(L/D)^2}$ and for a given value of θ, the position x/D is proportional to L/D:

$$\theta = \tan^{-1}\left(\frac{1}{2}\frac{L/D}{X/D}\right) \approx \frac{1}{2}\frac{L/D}{X/D} \quad . \tag{6.6}$$

Therefore, Zhu [7] observed a scaling law for the density distribution along the $(x, 0, 0)$ axis. He found that if ρ/ρ_s is scaled by $(L/D)^2$ and x/D by $(L/D)^{-1}$, the curves shown in Figure 6.9 should be overlapped. This is shown in Figure 6.10. However, small deviations can be observed from different scaled curves. This is due to the fact that Equation (6.5) is developed based on the assumption that there is no interaction between the two plumes ($Kn_s \to \infty$). When the value of L/D is smaller, the interaction of the two jets are stronger, which results in higher density in the secondary jet.

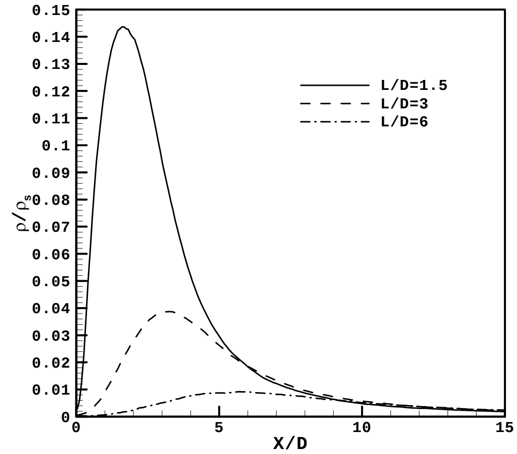

Figure 6.9. Normalized density profile along the $(x, 0, 0)$ axis fot different values of L/D; $Kn_s = 0.003$

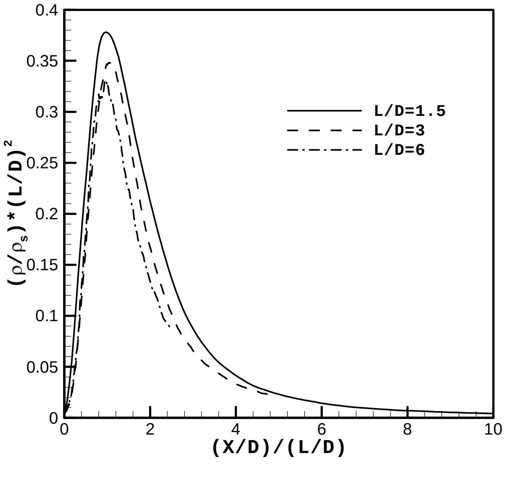

Figure 6.10. Scaled normalized density profile along the $(x, 0, 0)$ axis for different values of L/D; $Kn_s = 0.003$

6.1.4 Thermal Non-Equilibrium Effects

Figure 6.11 plots the translational and rotational temperature profiles along the $(x, 0, 0)$ symmetry axis for $Kn_s = 0.003$ and different values of L/D when the interacting jets are expanding into vacuum. Large deviation between the two temperatures can be found when X/D is small ($X/D < 5$) and for larger value of L/D, this deviation becomes even larger. This may be due to the low density in the region close to the orifice plate and a rapid temperature increase in the secondary jet due to the interaction of the two jets. Since the density is small, there are not enough number of inter-molecular collisions to balance the translational and rotational temperatures. Since rotational relaxation is a much slower process than the translational mode, therefore, large deviation between the two temperatures can be observed. When L/D is large, the density in the region close to the orifice plate becomes even smaller and the peak value of the translational temperature moves further downstream, thus the non-equilibrium effects between the two temperatures become more significant.

Figure 6.12 plots the translational and rotational temperature profiles along the $(x, 0, 0)$ symmetry axis for $L/D = 3$ and different values of Kn_s when the interacting jets are expanding into vacuum. Since the value of L/D is same, the peak value of the translational temperature is all located around $X/D \approx 1$. When Kn_s is smaller, the interaction between the two jets are stronger and the peak value of the translational temperature also increases. It is as expected that for larger Kn_s value, larger deviation between the two temperatures can be observed since the flow is more rarefied.

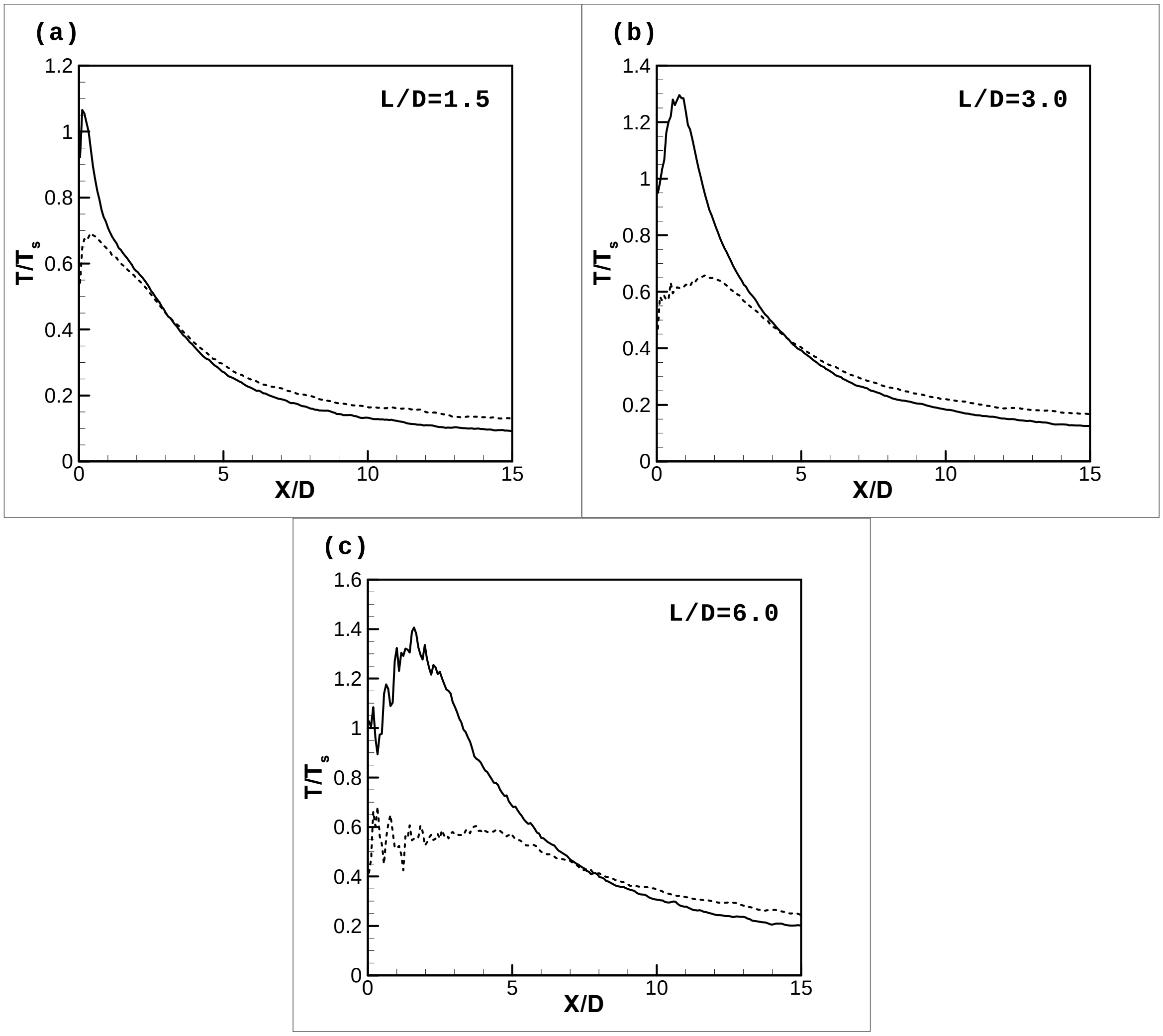

Figure 6.11. Translational Temperature (lines) and rotational temperature (dashed lines) distributions along the $(x, 0, 0)$ symmetry axis for $Kn_s = 0.003$ with different values of L/D when $P_s/P_b \rightarrow \infty$: (a) $L/D = 1.5$; (b) $L/D = 3.0$; (c) $L/D = 6.0$

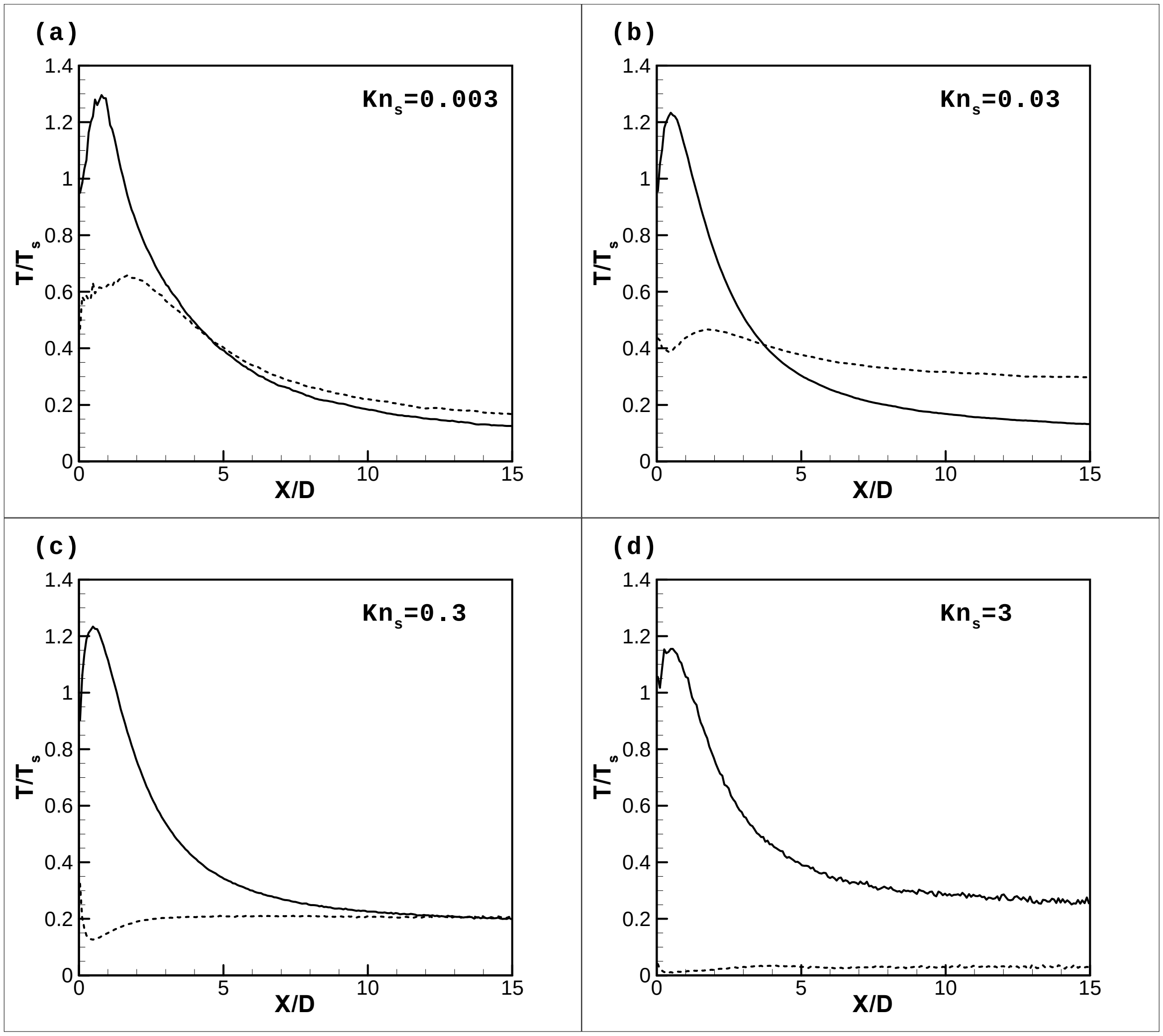

Figure 6.12. Translational Temperature (lines) and rotational temperature (dashed lines) distributions along the $(x, 0, 0)$ symmetry axis for $L/D = 3$ with different values of Kn_s when $P_s/P_b \to \infty$: (a) $Kn_s = 0.003$; (b) $Kn_s = 0.03$; (c) $Kn_s = 0.3$; (d) $Kn_s = 3$

6.2 Interacting Jets Expanding Into a Background with Finite Pressure

When interacting jets exhaust into a region with finite pressure, both the interaction between the molecules of the two jets and that between the jet gas molecules and the background gas molecules need to be considered. The barrel shocks, jet boundaries, and Mach disks in both of the primary and secondary jets are formed. This "primary-secondary" shock-cell structure is shown in Figure 1.1(b).

6.2.1 Rarefaction Parameter

As mentioned earlier, the interaction between the jet gas molecules with the background gas molecules depends on Kn_s and P_s/P_b (Equation (5.18)) and the interaction between the molecules of the gases of the two jets depends on Kn_s and L/D (Equation (6.2)). Therefore, the three parameters: Kn_s, L/D, and P_s/P_b characterize the overall rarefaction effects when interacting under-expanded jets exhaust into a background with finite pressure.

The same parameter ξ defined in Equation (5.17) will also be used here to characterize the overall interaction between the primary jets and the background gas (ξ_{primary}) and the interaction between the secondary jet and the background gas ($\xi_{\text{secondary}}$). The two cases $L/D \to 0$ and $L/D \to \infty$ are of interest:

1) When $L/D \to 0$, the primary and secondary jets overlap. The flow is identical to that of a single under-expanded jet with the jet stagnation pressure increased to $2P_s$.

2) When $L/D \rightarrow \infty$, the two jets do not affect each other and their respective stagnation pressure remains distinct at P_s.

Note that $\xi \propto (P_s/P_b)^{-1/2}$, and ξ_{primary} and $\xi_{\text{secondary}}$ can be expressed as

$$\xi = c \cdot D \left(P_s \cdot P_b\right)^{1/2} / T_s \tag{6.7}$$

where c depends on L/D:

$$c_{\text{primary}} = \begin{cases} 1/\sqrt{2} & \text{for} \quad L/D \rightarrow 0 \\ 1 & \text{for} \quad L/D \rightarrow \infty \end{cases} \tag{6.8}$$

and

$$c_{\text{secondary}} = \begin{cases} 1/\sqrt{2} & \text{for} \quad L/D \rightarrow 0 \\ \infty & \text{for} \quad L/D \rightarrow \infty \end{cases} \tag{6.9}$$

Soga [19] experimentally measured the density and rotational temperature in interacting jets when $Kn_s = 0.002$ and $P_s/P_b = 220$ for several values of L/D. This provides additional validation data for the present effort. The details of the conditions are shown in Table 6.2.

Figure 6.13 shows the density, translational temperature, and rotational temperature contours at the $y = 0$ symmetry plane for $L/D = 3$, $Kn_s = 0.002$, and $P_s/P_b = 220$. Compared with the results of the jets expanding into vacuum (Figure 6.4), it can be seen that the existence of the background pressure greatly changes the flow structure. Although the flow is sill rarefied and the shock structure is much dissipated, the primary and secondary shock-cell structure as shown in Figure 1.1(b) can still be observed, especially in the temperature contours. Figure 6.14 shows the same contours but for $z = 0$ symmetry plane. The results in Figure 6.14 should be contrasted with those in Figure 6.5. In the figure, a shock-cell structure is also evident at the $z = 0$ plane, whereas no such structure can be observed in the latter.

Table 6.2. Details of Soga's experiment

No.	P_s	D	T_s	L/D	Kn_s	P_b	M^*	**Purpose**	**Method**
1	*870* Pa	*3* mm	*285* K	0, 1.2, 2, 3, 6, 8, ∞	1.95142×10^{-3}	4.0 Pa	1.0	Density measurement	Electron beam fluorescence
2	*650* Pa				2.61190×10^{-3}	3.1 Pa		Temperature measurement	

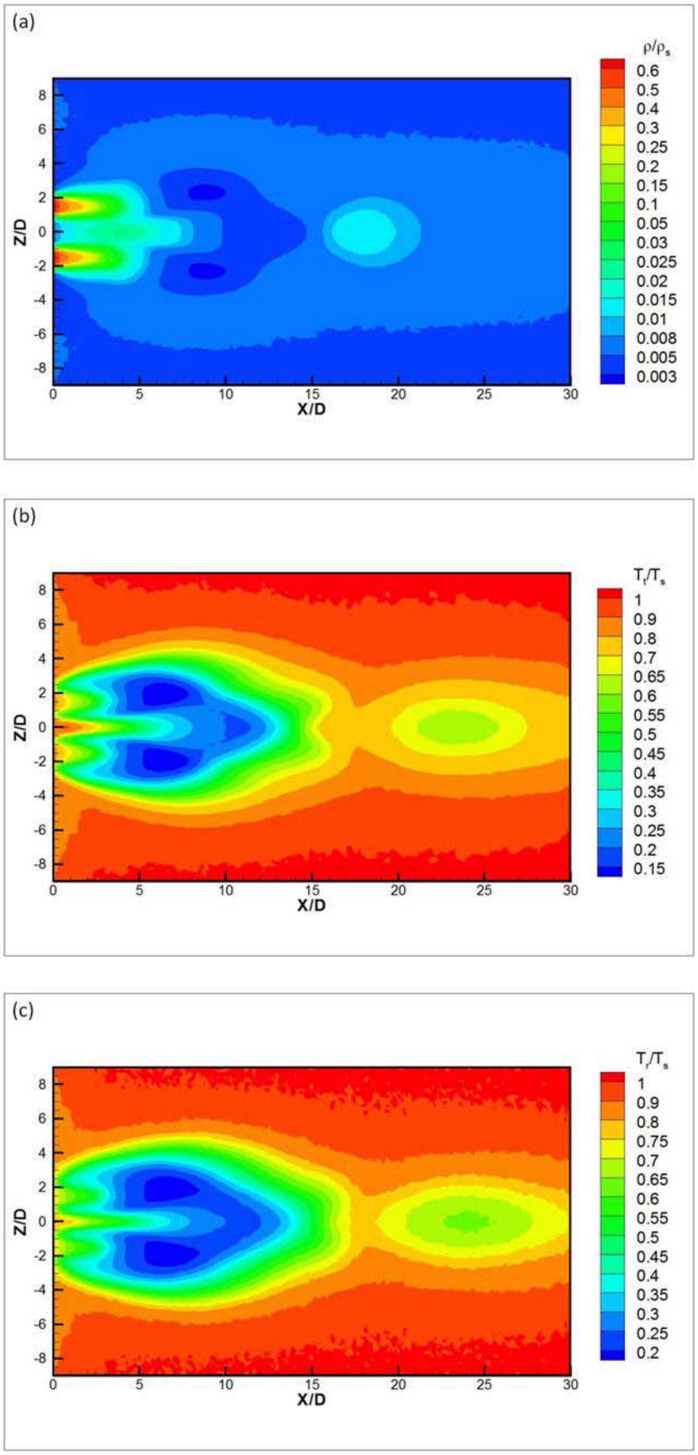

Figure 6.13. Density (a), translational temperature (b), and rotational temperature (c) contours in $y = 0$ plane for $L/D = 3.0$, $Kn_s = 0.002$, and $P_s/P_b = 220$

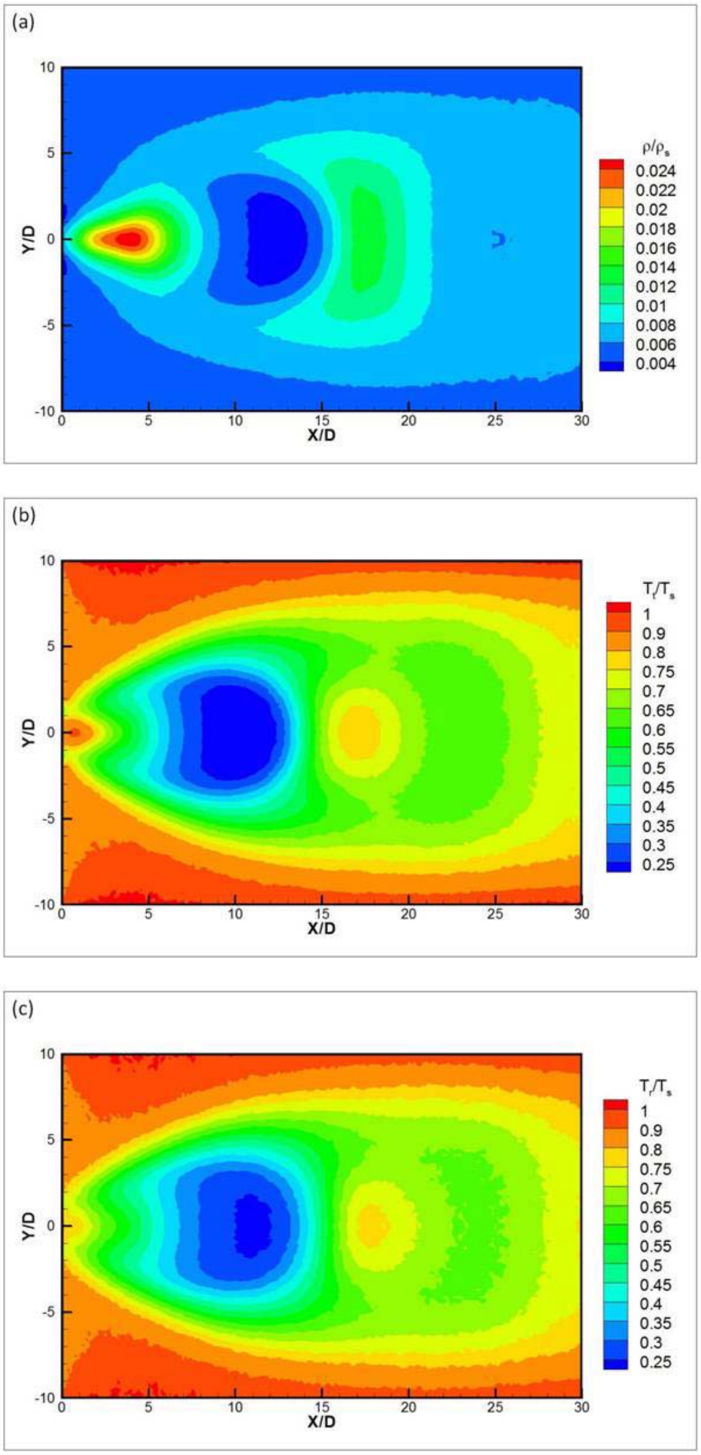

Figure 6.14. Density (a), translational temperature (b), and rotational temperature (c) contours in $z = 0$ plane for $L/D = 3.0$, $Kn_s = 0.002$, and $P_s/P_b = 220$

The calculated results are compared with Soga's experimental data in Figure 6.15, which shows the density distribution along the $(x, 0, 0)$ symmetry axis. Note that two sets of DSMC results are presented: $P_s/P_b = 220$ and $P_s/P_b \to \infty$. The monotonic decay of density after the first peak for the case $P_s/P_b \to \infty$ is expected based on the results from the previous section. Dagum also simulated this problem using DSMC, but he assumed that the jet expanded into vacuum. It is therefore not surprising that his result only compared well with Soga's data [19] when $X/D < 10$. Other investigations using a similar background condition (vacuum) in their simulation do not show results for $X/D \geq 10$ in their comparison with Soga's experiments, suggesting inaccurate results in this region. In our simulation, the correct background conditions ($P_s/P_b = 220$) is used and our predictions compare well with experimental data at all X/D values. Figure 6.16 shows the rotational temperature distribution along the $(x, 0, 0)$ axis. Since the experimental data for this variable is available only for $X/D < 8.0$, both the two cases $P_s/P_b = 220$ and $P_s/P_b \to \infty$ agree well with experimental data.

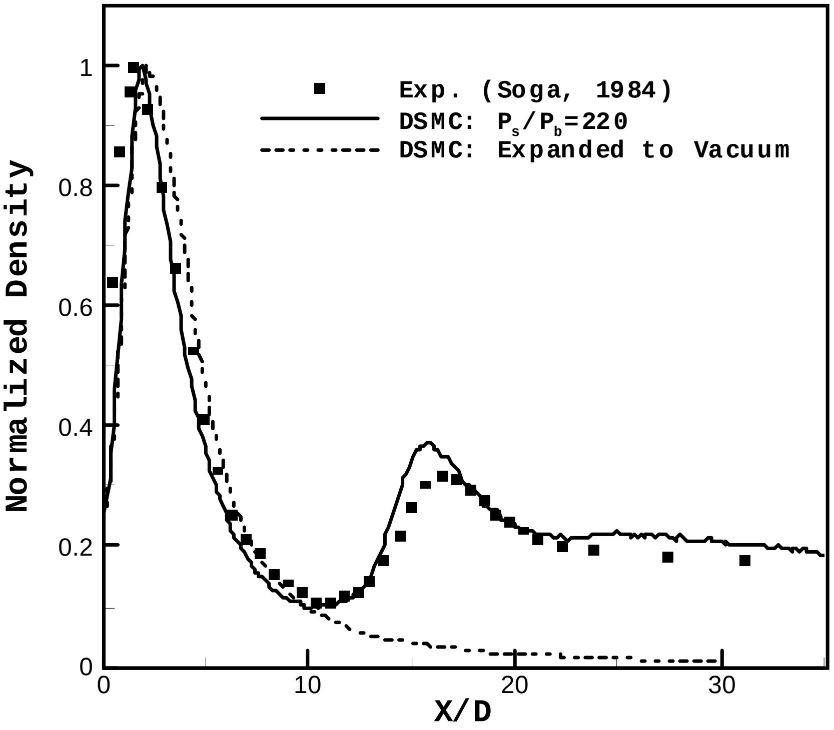

Figure 6.15. Density distribution along the $(x, 0, 0)$ axis showing comparison with Soga's experimental data for $L/D = 3.0$, $P_s/P_b = 220$, and $Kn_s = 0.002$. The case $P_s/P_b \to \infty$ (vacuum background) is shown as a reference.

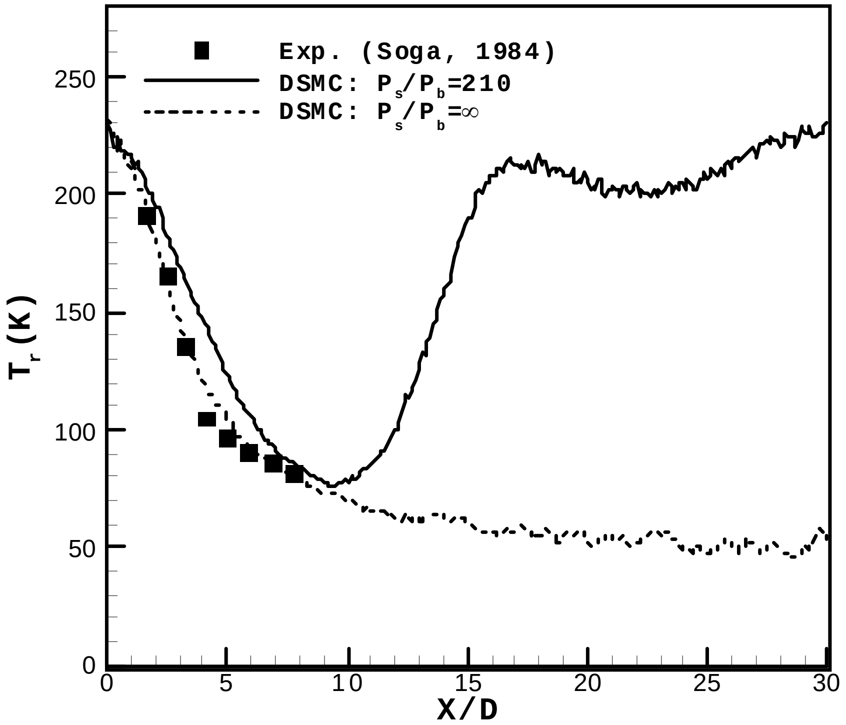

Figure 6.16. Rotational temperature distribution along the $(x, 0, 0)$ axis showing comparison with Soga's experimental data for $L/D = 3.0$, $P_s/P_b = 210$, and $Kn_s = 0.0027$. The case $P_s/P_b \to \infty$ (vacuum background) is shown as a reference.

6.2.2 Effects of L/D

The effects of L/D are further shown in Figures 6.17 through 6.20. Figures 6.17 and 6.18 show the density, translational temperature, and rotational temperature contours at $y = 0$ as in Figure 6.13, but with different values of L/D (1.5 and 6.0, respectively). Compared with Figure 6.13, in which $L/D = 3.0$, the effects of the separation distance L/D are shown. Smaller values of L/D lead to stronger interaction between the two jets, and to a better defined secondary jet, especially in the temperature contours. When L/D is increased to 6.0, the interaction between the two jets is much weaker.

Figure 6.19 shows the density distribution along the $(x, 0, 0)$ axis for $Kn_s = 0.002$, $P_s/P_b = 220$. It can be seen that increasing L/D values leads to smaller peaks, or weaker interactions between the two jets. Although the Mach disk is weak and dissipated in the secondary jet, it can be found that, for all L/D values (except $L/D = 8.0$), the location of the Mach disk in the secondary jet do not differ significantly ($X_{M,\text{secondary}}/D \approx 13$). This may be due to the large P_s/P_b value used ($P_s/P_b = 220$). When P_s/P_b is large, the position of the Mach disk in the secondary jet can be expected to be large (Equation (6.7)). When X/D is large, based on the definition of $Kn_p(\theta)$ (Equation (6.2)), the plumes from the two jets becomes much rarefied and the interaction region can be regarded as the fully mixing zone of the flow of the two jets. Note that the interaction angle θ can be calculated as $\theta = \tan^{-1}\left(\frac{1}{2}\frac{L/D}{X/D}\right)$, which means that when X/D is large, a small change in the value of L/D does not greatly affect the value of θ. Therefore, under these conditions, coupled with large values of P_s/P_b, L/D only has a mild effect on the location of the Mach disk in the secondary jet.

Figure 6.20 shows the density distribution along the $(x, 0, L/2)$ axis (symmetry axis of primary jet) for $Kn_s = 0.002$, $P_s/P_b = 220$, and different values of L/D. The plot clearly shows that the primary jet is also affected by the interaction between the two jets, especially when L/D is small. When the interaction effects are stronger, due to the existence of the strong oblique shock waves, the jet is less likely to cross the symmetry plane, leading to larger velocities (from decreasing cross-sectional area). Thus, the location of the Mach disk in the primary jet moves further downstream.

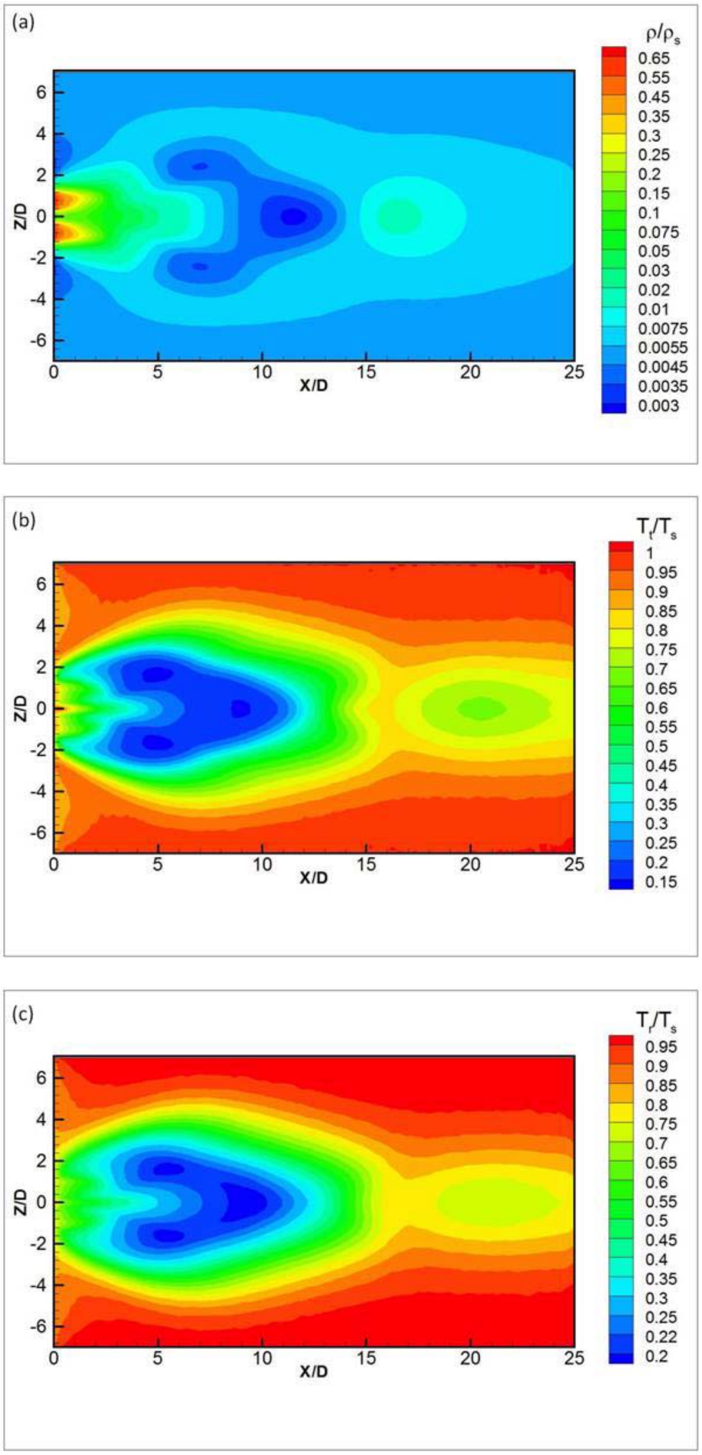

Figure 6.17. Density (a), translational temperature (b), and rotational temperature (c) contours on the $y = 0$ plane for $L/D = 1.5$, $Kn_s = 0.002$, and $P_s/P_b = 220$

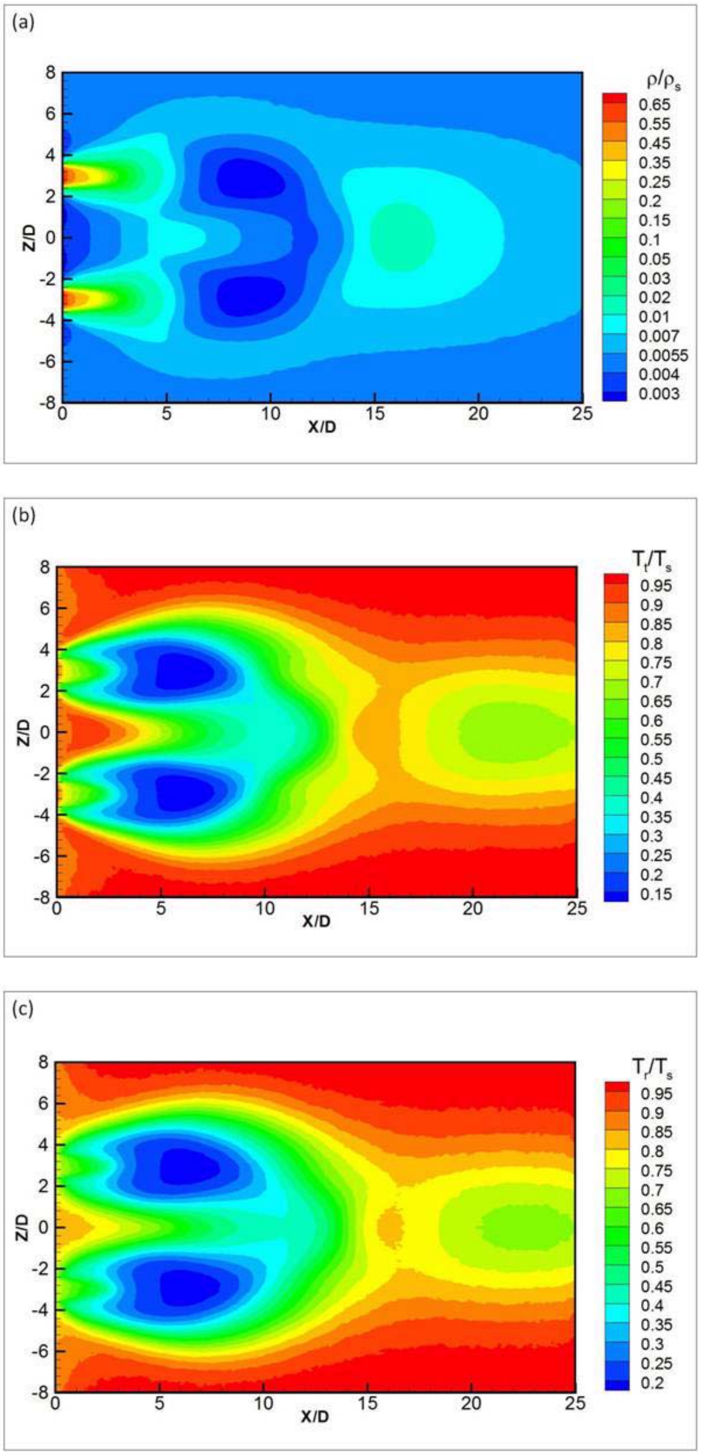

Figure 6.18. Density (a), translational temperature (b), and rotational temperature (c) contours on the $y = 0$ plane for $L/D = 6.0$, $Kn_s = 0.002$, and $P_s/P_b = 220$

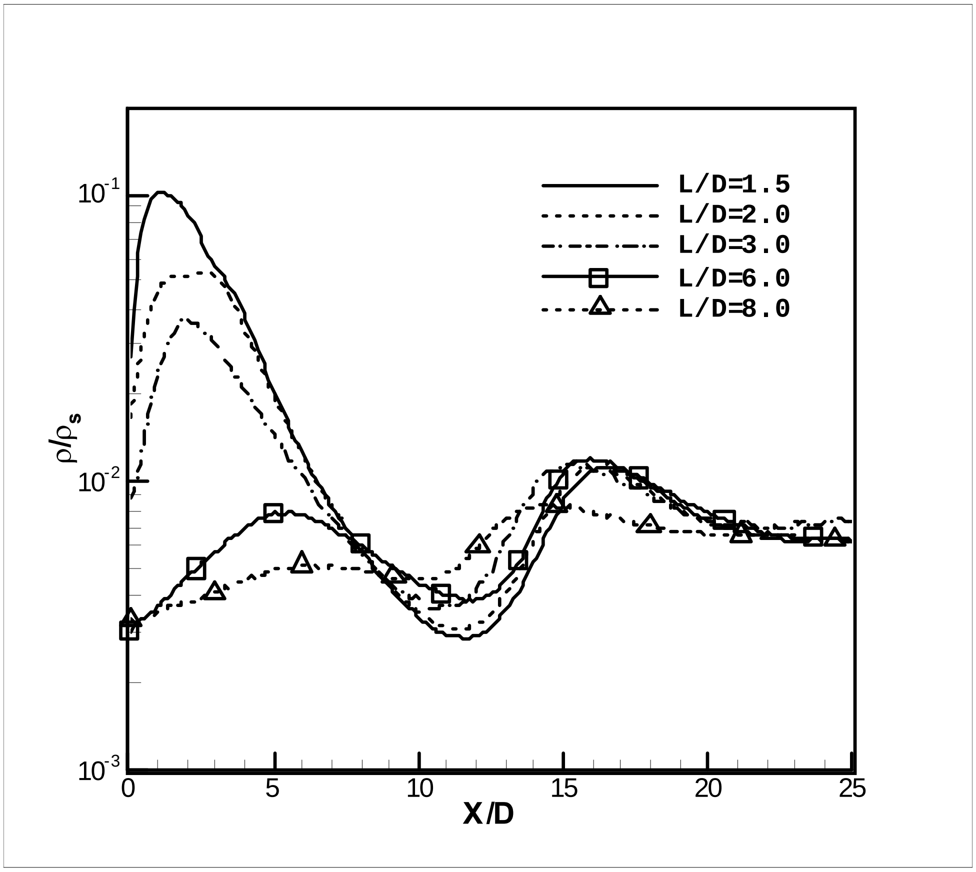

Figure 6.19. Density distribution along the $(x, 0, 0)$ symmetry axis for $Kn_s = 0.002$, $P_s/P_b = 220$, with $L/D = 1.5$, 2.0, 4.0, 6.0, and 8.0.

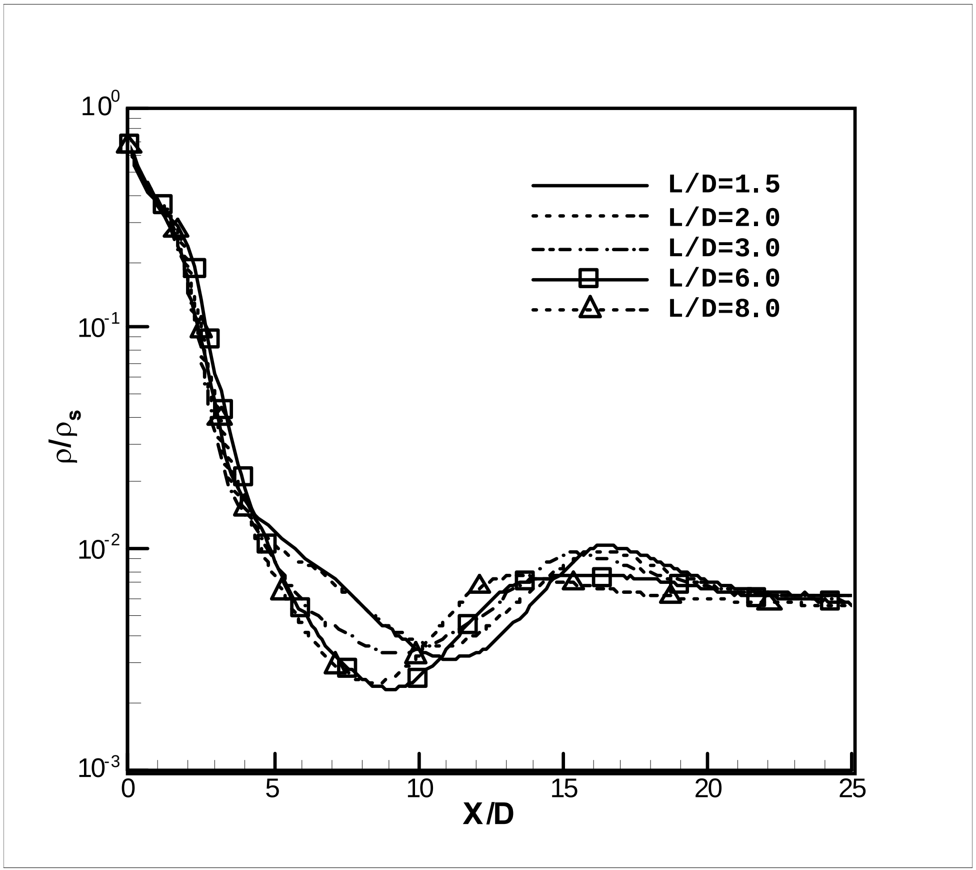

Figure 6.20. Density distribution along the $(x, 0, L/2)$ axis for $Kn_s = 0.002$, $P_s/P_b = 220$, with $L/D = 1.5$, 2.0, 4.0, 6.0, and 8.0.

6.2.3 Effects of Kn_s

The effects of Kn_s are shown in Figure 6.21, which plots the density distribution along the $(x, 0, 0)$ symmetry axis for $P_s/P_b = 200$, $L/D = 3.0$, and different values of Kn_s. As expected, it can be seen that reducing Kn_s values increases the interaction between the two jets (higher peaks). When Kn_s is relatively large ($Kn_s = 0.02$), the flow is strongly rarefied and there no Mach disk is formed in the interaction region. From Figures 6.19, 6.25, and 6.21, we can observe that the location of the Mach disk in the secondary jet depends on the values of the three parameters L/D, Kn_s, and P_s/P_b. This should be contrasted with the single jet case, where the Mach disk location depends only on P_s/P_b (Equation (5.15)).

6.2.4 Effects of P_s/P_b

The effects of P_s/P_b are shown in the density plot of Figure 6.22 with the parameters $Kn_s = 0.005$, $L/D = 3.0$, and different values of P_s/P_b. Since the value of L/D is same, the location of the peak values is almost same (around $X/D \approx 3$). As expected, reducing P_s/P_b strengthens the interaction between the secondary jet and the background gas. When P_s/P_b is small, stronger Mach disk is formed in the secondary jet and its location moves toward upstream. It can be seen that the existence of the background pressure significantly modifies the secondary jet flows, even when X/D is small. This is not the case for the primary jets, where the background gas does not significantly affect the expansion core. The reason may be due to the relatively small density values in the secondary jet, so that the flow in the secondary jet is more rarefied than the flow in the primary jets. Therefore, the molecules of the background gas can more easily penetrate into the secondary jet flow.

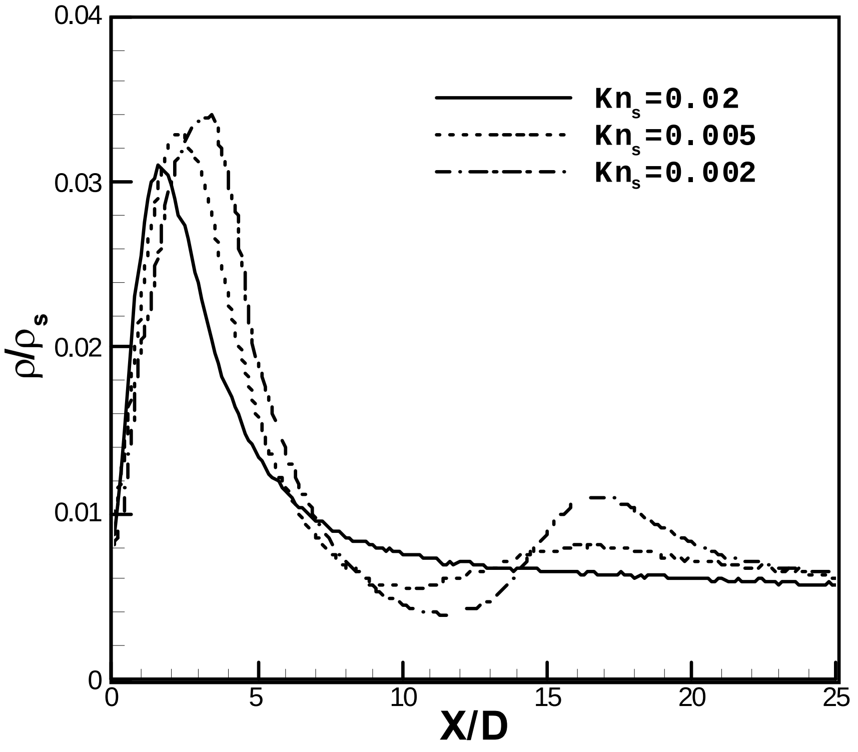

Figure 6.21. Density distribution along the $(x, 0, 0)$ symmetry axis for $P_s/P_b = 200$, $L/D = 3.0$, with $Kn_s = 0.02$, 0.005, and 0.002.

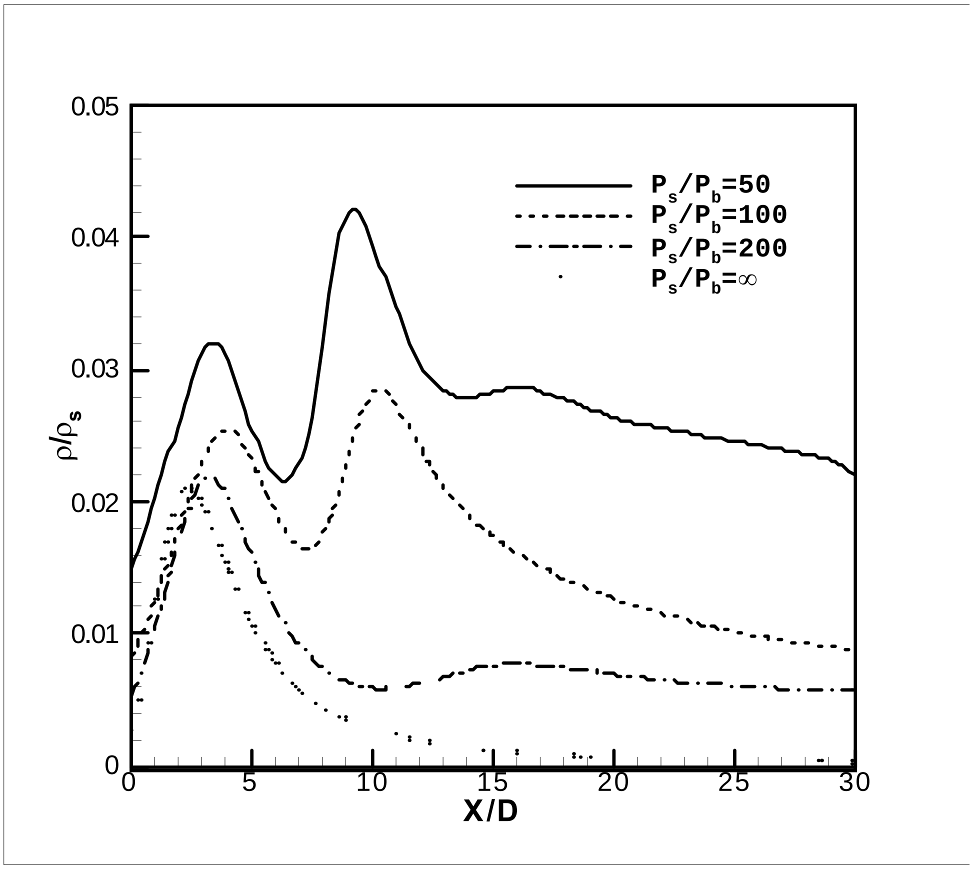

Figure 6.22. Density distribution along the $(x, 0, 0)$ symmetry axis for $Kn_s = 0.005$, $L/D = 3.0$, with $P_s/P_b = 50$, 100, 200, and ∞.

6.2.5 Thermal Non-Equilibrium Effects

The thermal non-equilibrium effects in the interacting jets are also investigated. Figures 6.23 and 6.24 show the translational-rotational non-equilibrium effects along the $(x, 0, 0)$ symmetry axis. Because the secondary jet is more rarefied, significant deviation between the translational and rotational curves are observed. Figure 6.23 shows the translational and rotational temperature profiles along the $(x, 0, 0)$ symmetry axis for $Kn_s = 0.002$, $P_s/P_b = 220$, and different values of L/D. When L/D is small, the interaction region is strong and, similar to the case of single under-expanded jets, large deviation between the two temperatures can be found in the expansion core (expansion before the Mach disk) and in the vicinity of the Mach disk. Large deviation between the two temperatures are especially evident in the vicinity of the orifice plate (X/D is small). This is due to the very low density in this region. When $L/D = 8.0$, the interaction between the two jets is of course weak and the non-equilibrium effects are not as significant as for the small L/D cases.

Figure 6.24 plots the translational and rotational temperature profiles along the $(x, 0, 0)$ symmetry axis for $Kn_s = 0.005$, $L/D = 3.0$, and different values of P_s/P_b. It shows the manner in which the background gas affects non-equilibrium in the secondary jet. Specifically, the figure shows that the smaller values of P_s/P_b, the smaller the deviation between the two temperatures. This agrees with the observations shown in Figure 6.22, which shows that the existence of the background gas increases the density in the secondary jet. That is, when the background pressure is high, the density in the secondary jet is also large and non-equilibrium effects are inhibited.

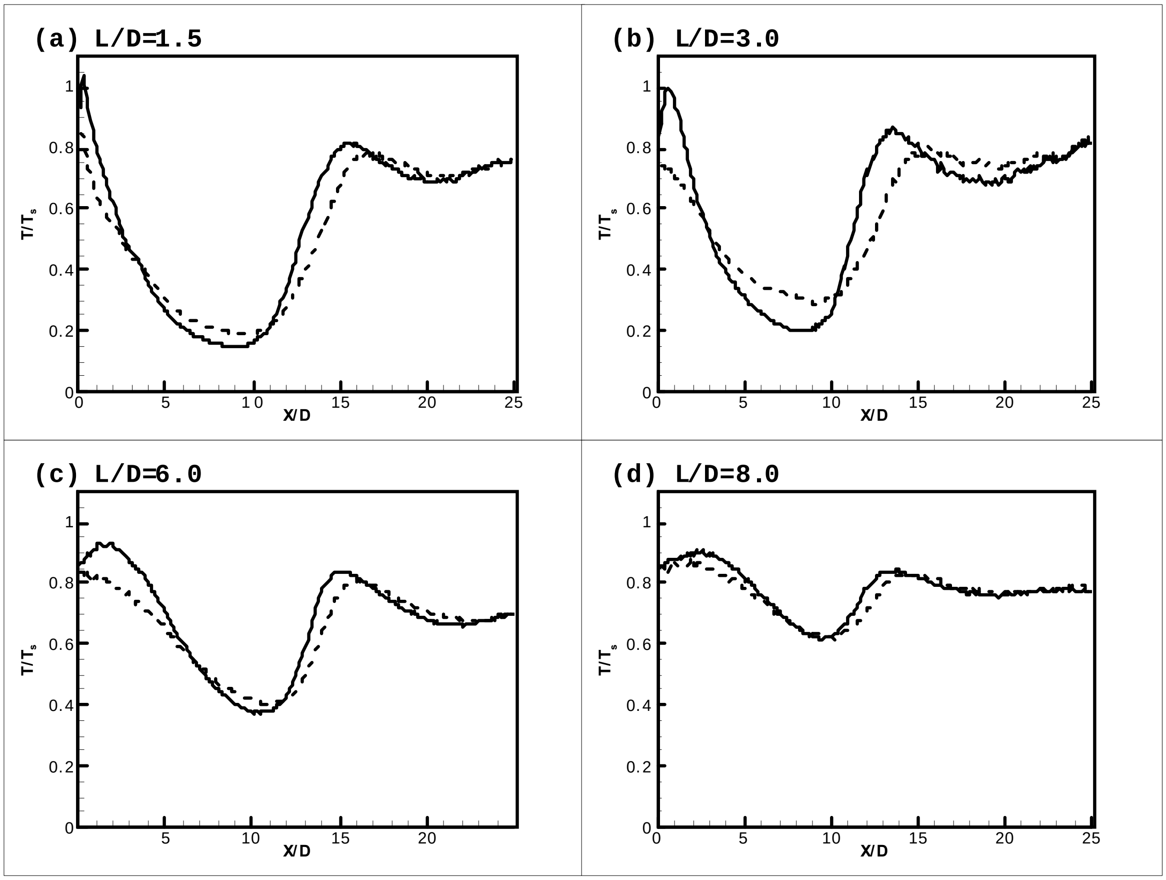

Figure 6.23. Translational Temperature (lines) and rotational temperature (dashed lines) distributions along the $(x, 0, 0)$ symmetry axis for $Kn_s = 0.002$, $P_s/P_b = 220$ with different values of L/D: (a) $L/D = 1.5$; (b) $L/D = 3.0$; (c) $L/D = 6.0$; (d) $L/D = 8.0$

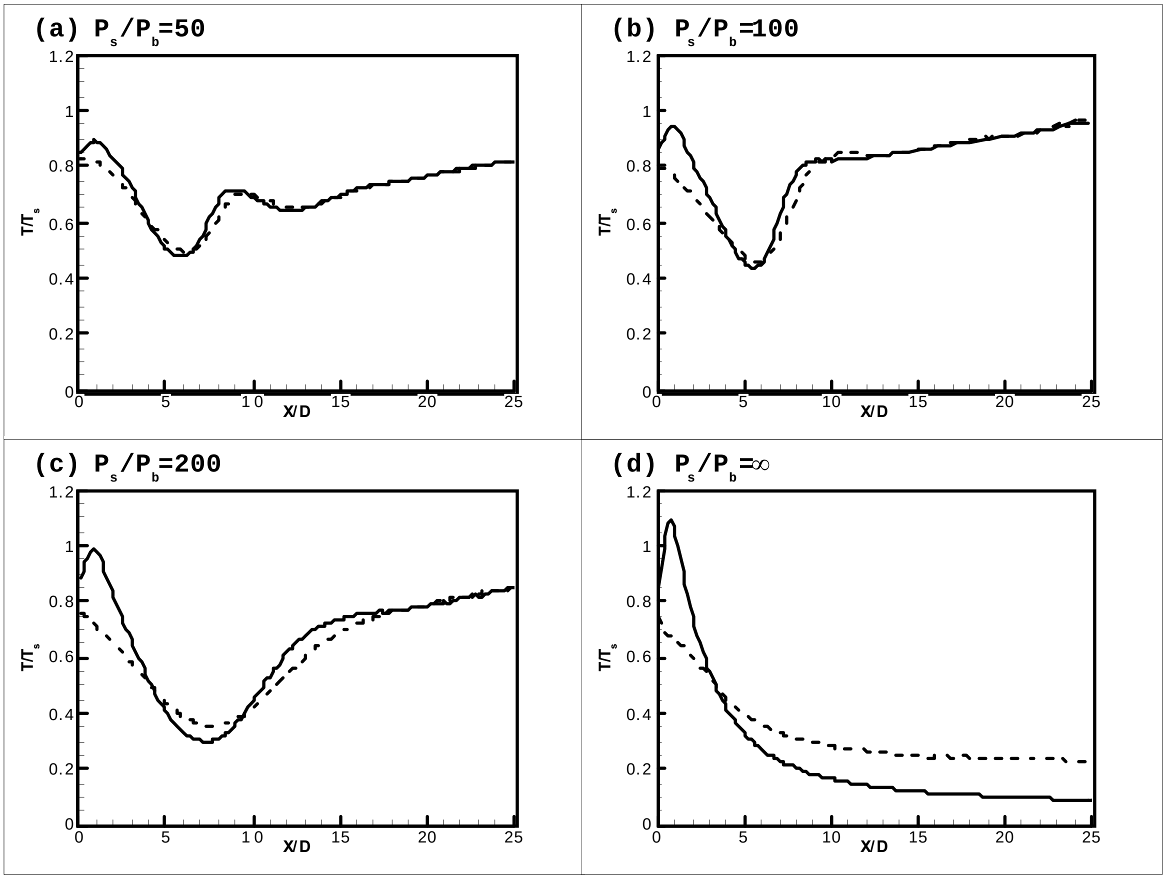

Figure 6.24. Translational Temperature (lines) and rotational temperature (dashed lines) distributions along the $(x, 0, 0)$ symmetry axis for $Kn_s = 0.005$, $L/D = 3.0$ with different values of P_s/P_b: (a) $P_s/P_b = 50$; (b) $P_s/P_b = 100$; (c) $P_s/P_b = 200$; (d) $P_s/P_b \to \infty$.

6.2.6 Location of the Mach disk

For single under-expanded jet, the Mach disk location $X_M \propto (P_s/P_b)^{1/2}$. Using the similar approach as in Equation (6.7), the location of the Mach disks in both the primary and secondary jets can be expressed as

$$X_M/D = c_M \cdot 0.67\,(P_s/P_b)^{1/2} \tag{6.10}$$

where c_M is also a function of L/D:

$$c_{M,\text{ primary}} = \begin{cases} \sqrt{2} & \text{for} \quad L/D \to 0 \\ 1 & \text{for} \quad L/D \to \infty \end{cases} \tag{6.11}$$

and

$$c_{M,\text{ secondary}} = \begin{cases} \sqrt{2} & \text{for} \quad L/D \to 0 \\ 0 & \text{for} \quad L/D \to \infty \end{cases} \tag{6.12}$$

Figure 6.25 shows the location of the Mach disks in the primary and secondary jets obtained from the DSMC calculations compared with data from Soga's experiment [19]. Although some deviations can be observed, the trends agree.

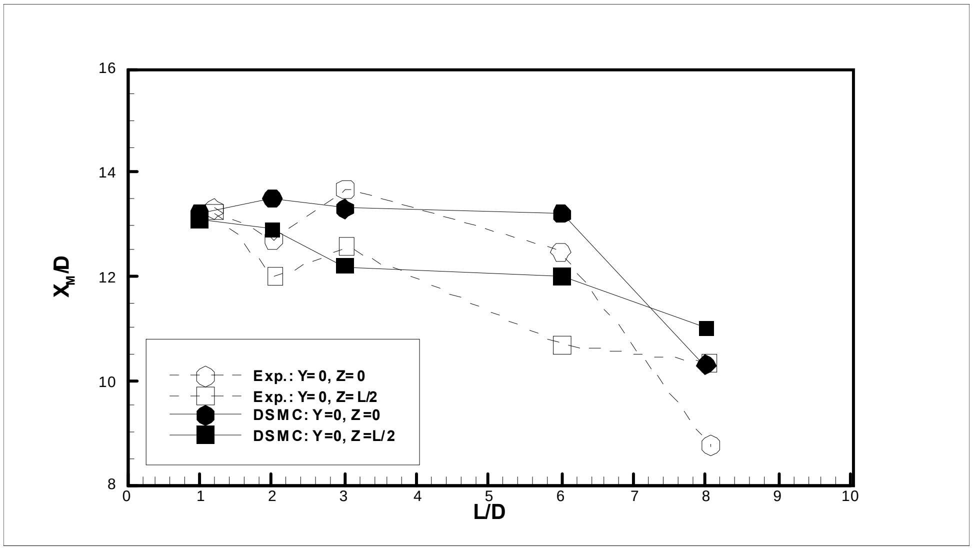

Figure 6.25. The location of Mach disk in both of the primary $(z = 0)$ and secondary $(z = L/2)$ jets, showing comparison with Soga's experimental data

Chapter 7
Conclusions

A parallel 3D DSMC code was successfully developed and validated. The dynamics of rarefied single jets and dual, interacting jets expanding into vacuum and into a background with finite pressure have been investigated.

The study of single under-expanded jet focuses on the shock structure and the thermal nonequilibrium effects when $0.002 \leq Kn_s \leq 0.02$ and P_s/P_b is between 20 and values that approach infinity. When Kn_s and P_s/P_b are relatively small, the "shock-cell" structure in experiments has been reproduced and the calculated location and size of the Mach disk compare well with the empirical relations. Other contributions include:

(1) For a single jet expanding into vacuum, a simple approximate expression was derived to evaluate the decay of the rotational temperature along the jet centerline and this compared well with the DSMC results and experimental data.

(2) For nitrogen under-expanded jets, the rotational-translational thermal nonequilibrium effects are found to be significant for the flows in all of the expansion core, Mach disk, and downstream of Mach disk, even when Kn_s and P_s/P_b is relatively small.

(3) In the expansion core, the deviation between the rotational and translational temperatures are more likely determined by the jet's Knudsen number, Kn_s, but are

not affected by the values of P_s/P_b. The rotational-translational nonequilibrium effects downstream from the Mach disk are affected by both Kn_s and P_s/P_b.

The dual interacting jets were simulated for $0.002 \leq Kn_s \leq 0.02$, $1.5 \leq L/D \leq 8.0$, and P_s/P_b values between 50 and infinity. The "primary-secondary" shock-cell structure has also been reproduced when the flow is in the near-continuum regime. The following observations were made:

(1) Compared with the density field, the interaction effects between the two jets are more significant in the temperature field. The interaction contributes to the creation of a high thermal nonequilibrium in the interaction region; this nonequilibrium decays at a fast rate downstream.

(2) For interacting jets expanding into a background with finite pressure, unlike the primary jets, in which the background gas cannot affect the expansion core, the existence of the background pressure significantly modifies the secondary jet flow.

(3) The value of L/D affects the locations of the Mach disk in both the primary and secondary jets. But when P_s/P_b is relatively large (such as $P_s/P_b = 220$) and L/D is relatively small ($L/D \leq 6.0$), the separation distance L/D has only a mild effect on the location of the Mach disk in the secondary jet.

(4) The secondary jet tends to be much more rarefied than the primary jet, and thermal non-equilibrium effects are significant in the secondary jet, especially in the vicinity

of the orifice plate. It is also found that the existence of the background gas helps to reduce the translational-rotational non-equilibrium effects in the secondary jet.

References

[1] Li, W. and Ladeinde, F., "Simulation and Analysis of Rarefied Parallel Interacting Sonic Jets," AIAA-2006-1192.

[2] Li, W., Simulation and Analysis of Rarefied Parallel Interacting Sonic Jets, Master's thesis, Department of Mechanical Engineering, Stony Brook University, NY, 2004.

[3] J. Sahu, J., "Numerical Computations of Three Dimensional Jet Interaction Flow Fields," AIAA-94-3521.

[4] Houshang, B. E., Levine, J. and Kawasaki, A., "Numerical Investigation of Twin-Nozzle Rocket Plume Phenomenology," Journal of Propulsion and Power, Vol. 16, No. 2, 2000, pp. 178-186.

[5] Dagum, L. and Zhu, S. H. K., "DSMC Simulation of the Interaction Between Rarefied Free Jets," AIAA-93-2872.

[6] Zhu, S. H. K. and Dagum, L., "A Parametric Study of Rarefied Jet Interaction Using DSMC," AIAA-94-2046.

[7] Zhu, S. H. K. and Dagum, L., "Self-Similarity in Rarefied Jet Interactions - a DSMC Study," AIAA-95-2030.

[8] Koppenwallner, G., "Scaling Laws for Rarefied Plume Interaction with Application to Satellite Thrusters," Proceedings of the 14th International Symposium on Space Technology and Science, Tokyo, May 1984, pp. 505-512.

[9] Ketsdever, A. Selden, N., Gimelshein, S., Alexeenko, A., Vashchenkov, P., and Ivanov, M., "Plume Interactions of Multiple Jets Expanding into Vacuum: Experimental Investigation," AIAA-2004-1348.

[10] Pal, S., Dey, S., and Miebach, T., "Numerical Simulation of a Dual-Source Supersonic Plasma Jet Expansion Process: Continuum approach," Journal of Physics D: Applied Physics, Vol. 40, 2007, pp. 3128-3136.

[11] Schaepkens, M., Selezneva, S., Moeleker, P., and Iacovangelo, C. D., “High-Rate Deposition of Abrasion Resistant Coatings Using a Dual-Source Expanding Thermal Plasma Reactor,” Journal of Vacuum Science & Technology A: Vacuum, Vol. 21, 2003, pp. 1266-1271.

[12] Autric, M., Lambert, L., and Itina, T., “Experimental and Theoretical Study of Dual-Crossed-Beam Pulsed Laser Deposition,” Proceedings of SPIE, Vol. 4070, 2000, pp.252-261.

[13] Ladeinde, F., Cai, X., Alabi, K., Reba, R., Schlinker, R., and Simonich, J., "On the Connection Between Near- Field and Far- Field Solutions of High- Speed Jet Noise," AIAA-2008-0011.

[14] Ladeinde, F., Alabi, K., Colonius, T., Gudmundsson, K., Schlinker, R., and Reba, R., "An Integrated RANS- PSE- Wave Packet Tool for the Prediction of Subsonic and Supersonic Jet Noise," AIAA-2010-4021.

[15] Dankert, C. and Koppenwallner, G., “Experimental Study of Interaction Between Two Rarefied Free Jets,” Rarefied Gas Dynamics: Proceeding of the 14th International Symposium on Rarefied Gas Dynamics, 1984, pp. 477-484.

[16] Cluass, J. S., Wright, B. R., and Bowie, G. E., “Twin Jet Noise Shielding for a Supersonic Cruise Vehicle,” AIAA Paper 79-670.

[17] Seiner, J. M., Manning, J. C., and Pooton, M. K., “Dynamic Pressure Loads Associated with Twin Supersonic Plume Resonance,” AIAA Paper 86-1539.

[18] Seiner, J. M., Manning, J. C., and Pooton, M. K., “Model and Full-Scale Study of Twin Supersonic Plume Resonance,” AIAA Paper 87-0244.

[19] Soga, T., Takanishi, M. and Yasuhara, M., “Experimental Study of Interaction of Underexpanded Free Jets,” Rarefied Gas Dynamics: Proceedings of the 14th International Symposium on Rarefied Gas Dynamics, July 1984, Tsukuba Science City, Japan, pp. 485-493.

[20] Niimi, T., Fujimoto, T., and Taoi, N., “Flow Fields of Interacting Parallel Supersonic Free Jets,” JSME International Journal, Series B, Vol. 39, No. 1, 1996, pp. 95-100

[21] Ladeinde, F., Cai, X., Li, W., and Agarwal, R., "A Unified Computational Methodology for Rarefied and Continuum Flow Regimes", AIAA-2004-1178.

[22] Ladeinde, F., Cai, X., and Agarwal, R., "On the Stability of High-Order Continuum (HOC) Equation for Hybrid HOC/DSMC Solvers," Proceedings of the 24th International Symposium on Rarefied Gas Dynamics, 2004, pp. 535-540.

[23] Wu, J. S., Tseng, K. C., and Wu, F. Y., “Parallel Three-Dimensional DSMC Method Using Mesh Refinement and Variable Time-Step Scheme,” Computer Physical Communications, Vol. 162, 2004, pp. 166-187

[24] Ikegawa, M., and Kobayashi, J., “Development of a Rare+1X Rarefied Flow Simulator Using the Direct Simulation Monte Carlo Method,” JSME International Journal, Series 2, Vol. 33, No. 3, 1990, pp. 463-467.

[25] Nance, P. R., Hash, D. B., and Hassan, H. A., “Role of Boundary Conditions in Monte Carlo Simulation of Microelectromechanical System,” Journal of Thermalphysics and Heat Transfer, Technical Notes, Vol. 12, No. 3, 1998, pp. 447-449.

[26] Wu, J.-S., Lee, F., and Wong, S.-C., “Pressure Boundary Treatment in Micromechanical Devices Using the Direct Simulation Monte Carlo Method,” JSME International Journal, Series 2, Vol. 44, 2001, pp. 439-450 (2001).

[27] Wu, J.-S., Chou, S.-Y., Lee, U.-M., Shao, Y.-L., and Lian, Y.-Y., “Parallel DSMC Simulation of a Single Under-Expanded Free Orifice Jet from Transition to Near-Continuum Regime,” Journal of Fluids Engineering, Vol. 127, 2005, pp. 1161-1170.

[28] Li, W. and Ladeinde, F., “Analysis of Single Under-Expanded Jets in Rarefied and Near-Continuum Regimes,” AIAA Journal (To be Submitted).

[29] Usami, M., and Teshima, K., “Three Dimensional DSMC Calculation of Interacting Flowfield in Two Parallel Underexpanded Jets,” Rarefied Gas Dynamics: Proceeding of the 21th International Symposium on Rarefied Gas Dynamics, 1999, pp.569-576.

[30] Oran, E. S., Oh, C. K., and Cybyk, B. Z., "Direct Simulation Monte Carlo: Recent Advances and Applications," Annual Review of Fluid Mechanics, Vol. 30, pp. 403-41, 1998

[31] Chen, Xi, Kinetic Theory and Its Applications in Studies of Heat Transfer and Fluid Flow, Tsinghua University Press, 1996 (In Chinese)

[32] Bird, G. A., Molecular Gas Dynamics, Clarendon Press, Oxford, 1976

[33] Bird, G. A., Molecular Gas Dynamics and the Direct Simulation of Gas Flows. 1st Ed., Oxford Univ. Press, Oxford, 1994.

[34] Cercignani, C., Rarefied Gas Dynamics, Cambridge University Press, Cambridge, 2000

[35] Koura, K., "Null-Collision Technique in the Direct-Simulation Monte Carlo Method," Physics of Fluids, Vol. 29, No. 11, 1986, pp. 3509-3511

[36] Borgnakke, C., and Larsen, P. S., "Statistical Collision Model for Monte Carlo Simulations of Polyatomic Gas Mixtures," Journal of Computational Physics 18, 1975, pp. 405-420

[37] Lumpkin, F. E., Haas, B. L., and Boyd, I. D., "Resolution of Differences Between Collision Number Definitions in Particle and Continuum Simulations," Physics of Fluids A, Vol. 3, 1991, pp. 2282-2284

[38] Parker, J. G., "Rotational and Vibrational Relaxation in Diatomic Gases," Physics of Fluids, Vol. 2, No. 4, 1959, pp. 449-462

[39] Hass, B. L., Hash, D., Bird, G. A., Lumpkin, F. E., and Hassan, H. A., "Rates of Thermal Relaxation in Direct Simulation Monte Carlo Methods," Physics of Fluids, Vol. 6, No. 6, 1994, pp. 2191-2201

[40] Boyd, I. D., "Direct Simulation of Rotational and Vibrational Nonequilibrium," AIAA Paper 89-1880

[41] Boyd, I. D., "Rotational-Translational Energy Transfer in Rarefied Nonequilibrium Flows," Physics of Fluids A, Vol. 2, No, 3, 1990, pp. 447-452

[42] Lumpkin, F. E., Chapman, D. R., and Park, C., "A New Rotational Relaxation Model for Use in Hypersonic Computational Fluid Dynamics," AIAA Paper 89-1737

[43] Abe, T., "New Model of DSMC for Internal-Translational Energy Transfer in Nonequilibrium Flow," presented at the 18th International Symposium on Rarefied Gas Dynamics, Vancouver, 1992

[44] Hass, B. L., McDonald, J. D., and Dagum, L., "Models of Thermal Relaxation Mechanics for Particle Simulation Methods, Journal of Computational Physics," Vol. 107, No. 2, 1993, pp. 348-358

[45] Bergemann, F., and Boyd, I. D., "New Discrete Vibrational Energy Model for the Direct Simulation Monte Carlo Method," Rarefied Gas Dynamics - Experimental Techniques and Physical Systems; International Symposium on Rarefied Gas Dynamics, 18th, 1994. pp.174-183

[46] Boyd, I. D., "Rotational and Vibrational Nonequilibrium Effects in Rarefied Hypersonic Flow, Journal of Thermophysics and Heat Transfer," Vol. 4, No. 4, 1990, pp. 478-484

[47] Millikan, R. C., and White, D. R., "Systematics of Vibrational Relaxation, Journal of Chemical Physics," Vol. 39, No. 12, 1963, pp. 3209–3213

[48] Hash, D. B., and Hassan, H. A., "Direct Simulation with Vibration-Dissociation Coupling," AIAA Paper 92-2875

[49] Boyd, I. D., "Assessment of Chemical Nonequilibrium in Rarefied Hypersonic Flow," AIAA Paper 90-0145

[50] Hass, B. L., and Boyd, I. D., "Models for Direct Monte Carlo Simulation of Coupled Vibration–Dissociation," Physics of Fluids A, Vol. 5, No. 2, 1993, 478-489

[51] Boyd, I. D., "Analysis of Vibration-Dissociation-Recombination Processes Behind Strong Shock Waves of Nitrogen," Physics of Fluids A, Vol. 4, No. 1, 1992, pp. 178-185

[52] Boyd, I. D., Bose, D., and Candler, G. V., "Monte Carlo Modeling of Nitric Oxide Formation Based on Quasi-classical Trajectory Calculations," Physics of Fluids, Vol. 9, No. 4, 1997, pp. 1162-1170

[53] Boyd, I. D., "A Threshold Line Dissociation Model for the Direct Simulation Monte Carlo Method," Physics of Fluids, Vol. 8, No. 5, 1996, pp. 1293-1300

[54] Marriott, P. M. and Bartel, T. J., "Comparison of DSMC Flow Field Predictions Using Different Models for Energy Exchange and Chemical Reaction Probability," Rarefied Gas Dynamics, 19th, Oxford, Ed. J. Harvey and G. Lord, New York, Oxford University Press, 1995, pp. 413-419

[55] Wadsworth, D. C., and Wysong, I. J., "Examination of DSMC Chemistry Models: Role of Vibrational Favoring," in Rarefied Gas Dynamics, Edited by Ching Shen, Peking University Press, Beijing, 1997, pp.174–179

[56] Boyd, I. D., "Nonequilibrium Chemistry Modeling in Rarefied Hypersonic Flows," in Chemical Dynamics in Extreme Environments, Edited by RA Dressler, World Scientific, Singapore, 2001, pp. 81-137

[57] Wysong, I. J., and Boyd, I. D., "Direct Simulation Monte Carlo Dissociation Model Evaluation: Comparision to Measured Cross Sections," Journal of Thermophysics and Heat Transfer, Vol. 16, No. 1, 2002, pp. 83-93

[58] Bondar, Y., Gimelshein, N., Gimelshein, S., Ivanov, M., and Wsong, I., "On the Accuracy of DSMC Modeling of Rarefied Flows with Real Gas Effects," Rarefied Gas Dynamics, 24th, Ed. M. Capitelli, 2005, pp. 607-613

[59] Lord, R. G., "Application of the Cercignani-Lampis Scattering Kernel to Direct Simulation Monte Carlo Method," Proceedings of the 17th International Symposium on Rarefied Gas Dynamics, Ed. A. E. Beylich, Aachen, Germany, 1991, pp. 1427-1433

[60] Cai, C., Boyd, I. D., Fan, J., and Candler, G. V., “Direct Simulation Methods for Low-Speed Micro-Channel Flows,” AIAA Paper No. 99-3801.

[61] Greene, E. F., and Hornig, D. F., "The shape and thickness of shock fronts in argon, hydrogen, nitrogen and oxygen," Journal of Chemical Physics, Vol. 21, 1953, pp. 617-624.

[62] Linzer, M., and Hornig, D. F., "Structure of shock fronts in argon and nitrogen," Physics of Fluids, Vol. 6, No. 12, 1963, pp. 1661-1668.

[63] Camac, M., "Argon shock structure," Proceedings of the 4th International Symposium on Rarefied Gas Dynamics, Vol. 1, 1965, pp. 240.

[64] Robben, F., and Talbot, L., "Measurement of shock wave thickness by the electron beam fluorescence method," Physics of Fluids, Vol. 9, No. 4, 1966.

[65] Mott-Smith, H. M., "The solution of the Boltzmann Equation for a shock wave," Physical Review, Vol. 82, No. 6, 1951, pp. 885-892.

[66] Muckenfuss, C., "Some aspects of shock structure according to the binomial model," Physics of Fluids, Vol. 5, No. 11, 1962, pp. 1325-1336.

[67] Sather, N. F., "Approximate solutions of the Boltzmann equation for shock waves," Physics of Fluids, Vol. 16, No. 12, 1973, pp. 2106-2109.

[68] Alsmeyer, H., “Density profiles in argon and nitrogen shock waves measured by the absorption of an electron beam,” Journal of Fluid Mechanics, Vol. 74, No. 3, 1976, pp.497-513.

[69] Holian, B. L., and Straub, G. K., "Shock-wave structure via nonequilibrium molecular dynamics and Navier-Stokes continuum mechanics," Physical Review A, Vol. 22, No. 6, 1980, pp. 2798-2808.

[70] Graur, I. A., Elizarova, T. G., Ramos, A., Tejeda, G., Fernandez, J. M., and Montero, S., "A study of shock waves in expanding flows on the basis of spectroscopic experiments and quasi-gasdynamic equations," Journal of Fluid Mechanics, Vol. 504, 2004, pp. 239-270.

[71] Elizarova, T. G., Shirokov, I. A., and Montero, S., "Numerical simulation of shock-wave structure for argon and helium," Physics of Fluids, Vol. 17, 2005, 068101.

[72] Kozlov, P. V., Losev, S. A., and Romanenko, Y. V., "Translational nonequilibrium of the shock wave front in an argon-helium gas mixture," Technical Physics Letters, Vol. 26, No. 11, 2000, pp. 69-75.

[73] Robben, F., and Talbot, L., "Experimental study of the rotational distribution function of nitrogen in a shock wave," Physics of Fluids, Vol. 9, No. 4, 1966, pp. 653-662.

[74] Boyd, I. D., "Analysis of rotational nonequilibrium in standing shock waves of nitrogen," AIAA Journal, Vol. 28, No. 11, 1990, pp.1997-1999.

[75] Koura, K., "Monte Carlo direct simulation of rotational relaxation of diatomic molecules using classical trajectory calculations: nitrogen shock wave", Physics of Fluids, No. 9, Vol. 11, 1997, pp. 3534-3549.

[76] Wysong, I. J., and Wadsworth, D. C., "Assessment of direct simulation Monte Carlo phenomenological rotational relaxation model," Physics of Fluids, Vol. 10, No. 11, 1998, pp. 2983-2994.

[77] Boyd, I. D., "Relaxation of discrete rotational energy distributions using a Monte Carlo method," Physics of Fluids A: Fluid Dynamics, Volume 5, No. 9, 1993, pp.2278-2286.

[78] Koura, K., “Improved null-collision technique in the direct simulation Monte Carlo method: application to vibrational relaxation of nitrogen,” Computers Math. Application, Vol. 35, 1998, pp. 139-154.

[79] Owen, P. L., and Thornhill, M. A., “The flow in an axially-symmetric supersonic jet from a nearly sonic orifice into a vacuum, ” Aeronautical Research Council, ARC Tech. Rept. RM-2616, 1948.

[80] Love, E. S., Grigsby, C. E., Lee, L. P., and Woodling, M. S., “Experimental and theoretical studies of axisymmetric free jets,” NASA TR R-6, 1959.

[81] Vick, A. R., Andrews Jr., E. H., Dennard, J. S., and Craidon, C. B., “Comparisons of experimental free-jet boundaries with theoretical results obtained with the method of characteristics,” NASA Technical Note D-2327, 1964.

[82] Hill, J. A. F., and Draper, J. S., "Analytical approximation for the flow from a nozzle into a vacuum," Journal of Spacecraft, Vol. 3, No. 10, 1966, pp. 1552-1554.

[83] Brook, J. W., "Far field approximation for a nozzle exhausting into a vacuum," Journal of Spacecraft, Vol 6, No. 5, 1969,pp. 626-628.

[84] Anderson, J. B., and Fenn, J. B., "Velocity distributions in molecular beams from nozzle sources," Physics of Fluids, Vol. 8, 1965, pp. 780-787.

[85] Hamel, B. B., and Willis, D. R., "Kinetic theory of source flow expansion with application to the free jet," Physics of Fluids, Vol. 9, 1966, pp.829-841.

[86] Edwards, R. H., and Cheng, H. K., "Steady expansion of a gas into a vacuum," AIAA Journal, 1966, pp. 558-561.

[87] Knuth, E. L., and Fisher, S. S., "Low-temperature viscosity cross sections measured in a supersonic argon beam," Journal of Chemical Physics, Vol. 48, No. 4, 1968, pp. 1674-1684.

[88] Cattolica, R., Robben, F., Talbot, L., and Willis, D. R., "Translational nonequilibrium in free jet expansions," Physics of Fluids, Vol. 17, No. 10, 1974, pp. 1793-1807.

[89] Koura, K., "Direct simulation Monte Carlo study of quantum effects on the spherical expansion of He," Physics of Fluids, Vol. 11, No. 10, 1999, pp. 3174-3180.

[90] Miffre, A., Jacquey, M., Buchner, M., Trenec, G., and Vigue, J., "Parallel temperatures in supersonic beams: ultracooling of light atoms seeded in a heavier carrier gas," Journal of Chemical Physics, Vol. 122, 2005, 094308.

[91] Robben, F., and Talbot, L., "Measurements of rotational temperature in a low density wind tunnel," Physics of Fluids, Vol. 9, 1966, pp. 644.

[92] Marrone, P. V., "Temperature and density measurements in free jets and shock waves," Physics of Fluids, Vol. 10, 1967, pp. 521.

[93] Gallagher, R. J., "Relaxation rates from time of flight analysis of molecular beams," Journal of Chemical Physics, Vol. 60, No. 9, 1974, pp. 3487-3491.

[94] Silvera, I. F., and Tommasini, F., “Intracavity Raman Scattering from Molecular Beams: Direct Determination of Local Properties in an Expanding Jet Beam,” Physical Review Letters, Vol. 37, No. 3, 1976, pp.136-140.

[95] Coe, D., Robben, F., Talbot, L., and Cattolica, R., "Rotational temperatures in nonequilibrium free jet expansion of nitrogen," Physics of Fluids, Vol. 23, 1980, pp. 706.

[96] Klots, C. E., "Rotational relaxation in sonic nozzle expansion," Journal of Chemical Physics, Vol. 72, 1980, pp. 192-197.

[97] Pollard, J. E., Trevor, D. J., Lee, Y. T., and Shirley, D. A., "Rotational relaxation in supersonic beams of hydrogen by high resolution photoelectron spectroscopy," Journal of Chemical Physics, Vol. 77, No. 10, 1982, pp. 4818,4825.

[98] Koura, K., "Study of rotational distribution of N_2 in the Ar free jet using two-parameter power gap model," Journal of Chemical Physics, Vol. 88, no. 10, 1982, pp. 5141-5145.

[99] Mazely, T. L., and Smith, M. A., "Rotational relaxation of N_2 in a free jet expansion," Journal of Chemical Physics, Vol. 94, 1990, pp. 6930-6933.

[100] Ilyukhin, A. A., Pykhov, R. L., Smirnov, V. V., and Marowsky, G., "Rotational temperature behavior in supersonic jet expansions of molecular nitrogen," Applied Physics B: Lasers and Optics, Vol. 51, No. 3, 1990, pp. 192-196.

[101] Mate, B., Tejeda, G., and Montero, S., "Raman spectroscopy of supersonic jets of CO_2: Density, condensation, and translational, rotational, and vibrational temperatures," Journal of Chemical Physics, Vol. 108, 1998, pp. 2676-2685.

[102] Campargue, R., Gaveau, M. A., and Lebehot, A., "Internal state populations in supersonic free jets and molecular beams," in Rarefied Gas Dynamics, Proceedings of the 14th International Symposium, edited by H. Oguchi (Tokyo University Press, Tokyo, 1984), Vol. II, pp. 551–566.

[103] Sharafutdinov, R. G., Ilyukhin, A. A., Smirnov, V. V., Belikov, A. E., Sukhinin, G. I., and Pykhov, R. L., "Populations of rotational levels of nitrogen molecules in free jets. Comparison of CARS and electron beam fluorescent technique," Chemical Physics, Vol. 233, 1998, pp. 127-144.

[104] Koura, K., "Direct simulation Monte Carlo study of rotational nonequilibrium in shock wave and spherical expansion of nitrogen using classical trajectory calculations", Physics of Fluids, Vol. 14, No. 5, 2002, 1689-1695.

[105] Mori, H., Niimi, T., Akiyama, I., Tsuzuki, T., “Experimental detection of rotational non-Boltzmann distribution in supersonic free molecular nitrogen flows,” Physics of Fluids, Vol. 17, 2005, pp. 117103.

[106] Albini, F. A., “Approximate computation of underexpanded jet structure,” AIAA JOURNAL, Vol. 3, 1965, pp. 1535-1537.

[107] Hubbard, E. W., “Approximate calculation of highly underexpanded jets,” AIAA Journal, Vol. 4, 1966, pp. 1877-1879.

[108] Boyton, F. P., “Highly underexpanded jet structure: exact and approximate calculations,” AIAA Journal, Vol. 8, 1967, pp. 1703-1704.

[109] Anonymous, AEROFLO’s User Manual, TTC Technologies, Inc., 2004.

[110] Young, W. S., “Derivation of the Free-Jet Mach-Disk Location Using the Entropy-Balance Principle,” Physics of Fluids, Vol. 18, No. 11, 1975, pp. 1421-1425.

[111] Lordi, J. A., and Mates, R. E., “Rotational relaxation in nonpolar diatomic gases,” Physics of Fluids, Vol. 13, 1970, pp. 291-308.

[112] Brau, C. A., and Jonkman, R. M., “Classical theory of rotational relaxation in diatomic gases,” Journal of Chemical Physics, Vol. 52, No. 2, 1970, pp. 477-484.

[113] Adamson, T. C., “The structure of the rocket exhaust plume without reaction at various altitudes,” Supersonic Flow, Chemical Processes and Radiative Transfer, Pergamon, New York, 1964.

[114] Otobe, Y., Matsuo, S., Tanaka, M., Kashimura, H., and Setoguchi, T., “A study on characteristics of under-expanded condensing jet,” JSME International Journal Series B, Vol. 49, No. 4, 2006, pp. 1165-1172.

[115] Phalnikar, K. A., Alvi, F. S., and Shih, C., “Behavior of free and impinging supersonic microjets,” AIAA Paper No. 2001-3047.

[116] Eastman, D. W., and Radtke, L. P., "Location of the normal shock wave in the exhaust plume of a jet," AIAA Journal, Vol. 1, No.4, 1963, pp. 918-919.

[117] Lewis Jr., C. H., and Carlson, D. J., "Normal shock location in underexpanded gas and gas-particle jets," AIAA Journal, Vol. 2,No. 4, 1964, pp.776-777.

[118] Ashkenas, H., and Sherman, F. S., “The structure and utilization of supersonic free jets in low density wind tunnels,” Rarefied Gas Dynamics: Proceeding of the 14th International Symposium on Rarefied Gas Dynamics, Vol. II, Academic, New York, 1965, pp. 84-105.

[119] Bauer, A. B., "Normal shock location of under-expanded gas-particle jet," AIAA Journal, Vol. 3, No. 6, 1965, pp. 1187-1189.

[120] Crist, S., Sherman, P. M., and Glass, D. R., "Study of the highly underexpanded sonic jet," AIAA Journal, Vol. 4, No. 1, 1966, pp. 68-71.

[121] Abbett, M., "Mach disk in underexpanded exhaust plumes," AIAA Journal, Vol. 9, No. 3, 1971, pp. 512-514.

[122] Davidor, W., and Penner, S. S., "Shock standoff distance and Mach-disk diameter in underexpanded sonic jets," AIAA Journal, Vol. 9, No. 8, 1971, pp. 1651-1652.

[123] Chang, I.-S., and Chow, W. L., "Mach disk from underexpanded axisymmetric nozzle flow," AIAA Journal, Vol. 12, No. 8, 1974, pp. 1079-1082.

[124] Addy, A. L., "Effects of axisymmetric sonic nozzle geometry on Mach disk characteristics," AIAA Journal, Vol. 19, No. 1, 1981, pp. 121-122.

[125] Muntz, E. P., Hamel, B. B., and Maguire, B. L., “Some characteristics of exhaust plume rarefaction,” AIAA Journal, Vol. 8, No. 9, 1970, pp. 2215-2222.

[126] Tejeda, G., Maté, B., Fernández-Sánchez, J. M., and Montero, S., “Temperature and Density Mapping of Supersonic Jet Expansions Using Linear Raman Spectroscopy,” Physical Review Letters, Vol. 76, 1996, pp. 34 – 37.

[127] Panda, J., and Seasholtz, R. G., "Measurement of shock structure and shock–vortex interaction in underexpanded jets using Rayleigh scattering," Physics of Fluids, Vol. 11, 1999, pp. 3761-3777.

[128] Venkatakrishnan, L., "Density measurements in an axisymmetric underexpanded jet by background-oriented Schlieren technique," AIAA Journal, Vol. 43, No. 7, 2005, pp. 1574-1579.

[129] Kolhe, P. S., and Agrawal, A. K., "Density measurements in a supersonic microjet using miniature rainbow schlieren deflectometry," AIAA Journal, Vol. 47, No. 4, 2009, pp. 830-838.

[130] Naik, S. V., Kulatilaka, W. D., Venkatesan, K. K., and Lucht, R. P., "Pressure, temperature, and velocity measurements in underexpanded jets using laser-induced fluorescence imaging," AIAA Journal, Vol. 47, No. 4, 2009, pp. 839-849.

[131] Vatsa, V. N., Anderson, O. L., and Werle, M. J., "Solution of slightly underexpanded two-dimensional and axisymmetric coflowing jets," AIAA Journal, Vol. 19, No. 3, 1981, pp. 303-310.

[132] Dash, S. M., Wolf, D. E., and Seiner, J. M., "Analysis of turbulent underexpanded jets, part I: parabolized Navier-Stokes model, SCIPVIS," AIAA Journal, Vol. 23, No. 4, 1985, pp. 505-514.

[133] Abdol-Hamid, Khaled, S., “Three-dimensional calculations for underexpanded and overexpanded supersonic jet flows,” AIAA Paper No. 1989-2196.

[134] Chuech, S. G., Lai, M.-C., and Faeth, G. M., "Structure of turbulent sonic underexpanded free jets," AIAA Journal. Vol. 27, 1989, pp. 549-559.

[135] Palacio, A., Malin, M., Proumen, N., and Sanchez, L., "Numerical computations of steady transonic and supersonic flow fields," International Journal of Heat and Mass Transfer, Vol. 33, No. 6, 1990, pp. 1193-1204.

[136] Bobba, C. R., Venkatapathy, E., Krothapalli, A., DeHart, J. J., and Wishart, D. P., "Structure of supersonic plumes: computational and measurements," AIAA Paper No. 95-0781

[137] Pao, S. P., and Abdol, K. S., "Numerical Simulation of Jet Aerodynamics Using the Three-Dimensional Navier-Stokes Code PAB3D," NASA Technical Report No. NASA-96-tp3596.

[138] Gribben, B. J., Cantariti, F., Badcock, K. J., and Richards, B. E., "Numerical study of an under-expanded jet," European Symposium on Aerothermodynamics for Space Vehicles, 3rd, Noordwijk, Netherlands, 1998, pp. 111-118.

[139] McDaniel, J., Glass, C., Staack, D., and Miller, C., "Experimental and computational comparison of an underexpanded jet flowfield," AIAA Paper No. 2002-0305

[140] Matsuo, S., Tanaka, M., Otobe, Y., Kashimura, H., Kim, H.-D., and Setoguchi, T., "Effect of axisymmetric sonic nozzle geometry on characteristics of supersonic air jet," Journal of Thermal Science, Vol. 13, No. 2, 2004, pp. 121-126.

[141] Si-Ameur, M., "Numerical simulation of turbulent underexpanded jet," International Journal of Fluid Mechanics Research, Vol. 31, 2004, pp. 8.

[142] Muntz, E. P., Hamel, B. B., and Scott, P. B., "A study of a background gas penetration into underexpanded jets and the resulting separation of gas mixture," Entropie, Vol. 42, 1971, pp.28-32.

[143] Brook, J. W., and Hamel, B. B., "Spherical source flow with a finite back pressure," Physics of Fluids, Vol. 15, No. 11, 1972, pp 1898-1912.

[144] Brook, J. W., Hamel, B. B., Muntz, E. P., “Theoretical and experimental study of background gas penetration into underexpanded free jets,” Physics of Fluids, Vol. 18, No. 5, 1975, pp. 517-528.

[145] D’Ambrosio, D., De Socio, L. M., and Gaffuri, G., "Physical and numerical experiments on an under-expanded jet," Meccanica, Vol. 34, No. 4, 1999, pp. 267-280.

[146] Mukherjee, J., Gantayet, L. M., and Ahmad, S. A., "Free jet expansion of atomic beam: simulation studies of some parameters, Journal of Physics D: Applied Physics, Vol. 33, No. 11, 2000, pp. 1386-1392.

[147] Usami, M., and Teshima, K., "DSMC calculation of supersonic free jets from an orifice with convex and concave corners," Rarefied Gas Dynamics: 22nd International Symposium. AIP Conference Proceedings, Volume 585, 2001, pp. 825-832.

[148] Teshima, K., and Usami, M., "DSMC simulation of axisymmetric supersonic free jets," Computational Fluid Dynamics Journal, Vol.10, 2001, pp. 525-530.

[149] Ivanov, M. S., Markelov, G. N., Gerasimov, Yu. I., Krylov, A. N., Mishina, L. V., Sokolov, E. I., “Free-flight experiment and numerical simulation for cold thruster plume” AIAA Paper No. 98-0898.

[150] Wang, W. L., and Boyd, I. D., “Hybrid DSMC-CFD simulations of hypersonic flow over sharp and blunted bodies”, AIAA-2003-3644.